Title

Deterministic Image Analysis for In Situ Transmission Electron Microscopy

Author

Mulvey, Justin T

Publication Date

2024

UNIVERSITY OF CALIFORNIA, IRVINE

Deterministic Image Analysis for In Situ Transmission Electron Microscopy

DISSERTATION

submitted in partial satisfaction of the requirements
for the degree of

DOCTOR OF PHILOSOPHY

in Materials Science and Engineering

by

Justin T Mulvey

Dissertation Committee:
Assistant Professor Joseph P. Patterson, Chair
Assistant Professor Stacy M. Copp
Assistant Professor William J. Bowman

2024

DEDICATION

I dedicate my dissertation to my parents Katherine Mulvey, OD, and Raymond Mulvey, OD, for teaching me hard work and independence. My dissertation would not have been possible without your unconditional love and support.

TABLE OF CONTENTS

Page

LIST OF FIGURES v

ACKNOWLEDGEMENTS x

VITA xii

ABSTRACT OF THE DISSERTATION xvi

INTRODUCTION 1
- 0.1 Transmission electron microscopy techniques 1
- 0.2 Convergence of advanced microscopy and data science 2
- 0.3 Defining a microscope image 3
- 0.4 Summary of chapters 3
- 0.5 References 4

CHAPTER 1: Correlating electrochemical stimulus to structural change in liquid electron microscopy videos using the structural dissimilarity metric 7
- 1.1 Abstract 8
- 1.2 Introduction 8
- 1.3 Methods 11
  - 1.3.1 DSSIM analysis workflow 11
  - 1.3.2 Parameter tuning 13
  - 1.3.3 Dataset considerations for DSSIM analysis 14
- 1.4 Results and Discussion 15
  - 1.4.1 DSSIM analysis of bright-field liquid cell STEM 15
  - 1.4.2 DSSIM analysis of bright-field LCTEM 17
  - 1.4.3 Comparison of DSSIM analysis and segmentation analysis 20
- 1.5 Code Availability and Efficiency 22
- 1.6 Data Acquisition 23
- 1.7 Conclusion 23
- 1.8 References 24

CHAPTER 2: Applying DSSIM analysis to quantify electrically-fueled dissipative self-assembly processes captured with liquid cell electron microscopy and confocal fluorescence microscopy 28
- 2.1 Abstract 29
- 2.2 Introduction 29
- 2.3 Liquid Cell Transmission Electron Microscopy (LCTEM) 32
  - 2.3.1 LCTEM: Methods and Results 32
    - 2.3.1.1 Preprocessing algorithm 32
    - 2.3.1.2 Segmentation algorithm 33
    - 2.3.1.3 DSSIM analysis 36
  - 2.3.2 LPEM: Discussion 39
- 2.4 Confocal Laser Scanning Microscopy (CLSM) 40
  - 2.4.1 CLSM: Methods and Results 40
    - 2.4.1.1 Preprocessing algorithm 40
    - 2.4.1.2 DSSIM analysis 43
  - 2.4.2 CLSM: Discussion 49

2.5 Conclusion 49
2.6 References 50

CHAPTER 3: Tracking transient nanofiber ordered phase in time-resolved cryoEM images via template matching and data science 52
3.1 Abstract 53
3.2 Introduction 53
3.3 Methods 55
3.3.1 Selection of cryoEM parameters 56
3.3.2 Cross-correlation template generation 56
3.3.3 Stacked fiber phase segmentation 57
3.3.4 TEM defocus correction 58
3.3.5 Labeling degree of stacking 60
3.4 Results 62
3.5 Discussion 66
3.6 Conclusion 67
3.7 References 68

CHAPTER 4: Observation of liquid−liquid-phase separation and vesicle spreading during supported bilayer formation via liquid-phase transmission electron microscopy 69
4.1 Abstract 70
4.2 Introduction 70
4.3 Methods and Results 72
4.3.1 Image pre-processing 72
4.3.2 Vesicle segmentation-based area and contrast analysis 74
4.3.3 Vesicles membrane rupture analysis 78
4.3.4 Video cross sectional time series analysis of bilayer formation 83
4.3.5 Bilayer coverage calculation 85
4.4 Discussion 86
4.5 Conclusion 89
4.6 References 89

CHAPTER 5: Liquid electron microscopy with non-aqueous solvents: evaluating the beam-sample interactions of complex liquid structures 93
5.1 Introduction 94
5.2 Methods and Results 94
5.3 Discussion 97
5.4 References 98

LIST OF FIGURES

Page

Figure 1.1 DSSIM analysis workflow. (A) Raw data is denoised with a combination of temporal and spatial averaging. (B) DSSIM analysis is applied using the defined parameters. Temporally offset images in the video are compared in a sliding-window operation (left). Image pairs are analyzed with the DSSIM metric which compares the same local neighborhoods of each image to produce a DSSIM image (right). Note images have been downsized by a factor of 4 to improve figure legibility. (C) DSSIM analysis results are quantified with global analysis (entire image) and regional analysis (cropped image. 11

Figure 1.2 DSSIM analysis applied to a previously published bright-field liquid cell STEM video. A-F) Select microscopy frames (top) and corresponding DSSIM frames (bottom) during electrode charging (A-D) and discharging (E,F). Bright pixels values correspond to regions of high dissimilarity between frames. Bottom labels correspond to the times of the two microscopy frames used to calculate the DSSIM image. Red arrows in (C, E) shows STEM scanline artifact in the DSSIM image. G) CV plotted as current vs. potential and H) current vs. time with key frames from (A-F) indicated with triangles. (H) contains a mean DSSIM plot, with key correlative features highlighted with dashed lines. High DSSIM values correspond to timepoints of high change. I) Mean DSSIM and MSE comparison. 15

Figure 1.3 (A,C) Consecutive frames in the bright-field liquid cell STEM video with (B) corresponding DSSIM image. Arrow in the DSSIM image highlights an isolated structural change event. 17

Figure 1.4 DSSIM analysis applied to bright-field LCTEM data. A-F) Select microscopy frames (top) and corresponding DSSIM frames (bottom) during electrode plating (A-D) and stripping (E,F). Bright pixels values correspond to regions of high dissimilarity between frames. Bottom labels correspond to the times of the two microscopy frames used to calculate the DSSIM image. (G) Square-wave chronoamperometry plotted as current vs. time and (H) potential vs. time compared to mean DSSIM. High DSSIM values correspond to timepoints of high change. Current and potential data was smoothed using a Gaussian-weighted sliding-window average with a stand deviation of 1.5 datapoints. (I) Zoom-in to dashed region in H. Black dashed lines mark timescale of features in the potential plot. Red dashed lines mark the timescale of the DSSIM peaks using FWHM. 18

Figure 1.5 Summation of all DSSIM frames from the bright-field LCTEM dataset. Arrows highlight regions where multiple nucleation events occurred on the electrode. 20

Figure 1.6 Regional DSSIM analysis compared to segmentation-based growth-rate analysis. (A,D) Select microscopy frames showing segmentation of particle (top) and corresponding DSSIM frames (bottom) during electrode plating and stripping. Bright pixels values correspond to regions of high dissimilarity between frames. Bottom labels correspond to the times of the two microscopy frames used to calculate the DSSIM image. (B,E) Segmented particle areas for each frame plotted over time. Black line indicates a sliding-window Gaussian-weighted average. (C,F) Growth rate calculated as the derivative of the smoothed particle area with respect to time and mean DSSIM from regional analysis. Dashed lines show key features are aligned. 21

Figure 1.7 ImageJ user interface for applying DSSIM analysis. DSSIM analysis can also be applied using Python or MATLAB scripts. 23

Figure 2.1 Schematic representation of the CSH/CSSC electrically-fueled dissipative self-assembly process. 30

Figure 2.2 Image pre-processing and segmentation pipeline. a) Images were spatially binned with pixel averaging, temporally binned with frame averaging, and contrast corrected by removing outlier pixels when displaying the image. Outliers were only removed when displaying the image and remain in the image in subsequent steps. b) A Gaussian FFT band-pass filter was applied to isolate the mid frequencies of the FFT which correspond to the sample. C) The average Otsu threshold of non-electrode pixels was calculated and applied to every image to produce a segmentation map. 33

Figure 2.3 Segmentation analysis of the LCTEM video. a) Spatially and temporally binned LCTEM images. b) Flattened LCTEM images. c) Binary images showing locations of segmented particles from b). d) Flattened LCTEM images with segmented structures outlined in green. 35

Figure 2.4 Regional segmentation analysis of the LCTEM video. a) Segmentation map divided into 4 colored regions based on distance from the electrode. Each region is 600 nm thick. B) Structure density within each region plotted over time. Density is calculated by the number of segmented pixels divided by the total pixels of the distance band. C) Band density plot normalized to the peak value. The bands reach their peak density sequentially, starting at the closest band and then moving outward. 35

Figure 2.5 Regional segmentation analysis of the LCTEM video. a) Segmentation map divided into 5 vertical regions based on distance from the left side of the image, denoted by color. Each region is 600 nm thick. B) Structure density within each region plotted over time. Density is calculated by the number of segmented pixels divided by the total pixels of the vertical band. C) Band density plot normalized to the peak value. Arrow highlights time points where there is a subtle increase in segmented area in the first right region of the viewing area where all other regions are decreasing. 36

Figure 2.6 Comparison of processed, flattened, and DSSIM LCTEM images. a) Spatially and temporally binned LCTEM images. b) Flattened LCTEM images. c) Dissimilarity images from DSSIM analysis. Bright pixel values correspond to regions of high dissimilarity between frames. Top time labels correspond to the times (seconds) of the two LCTEM images used to calculate the DSSIM image. 37

Figure 2.7 Visualization and quantification of fiber foci dynamics. a) The image was divided into 36 overlapping vertical regions, each 400 nm thick, based on distance from left edge of the image. The dashed line shows the size of 1 region. The color gradient shows distance from the left side of the image for each of the 36 regions, with purple being closest and yellow the furthest. Some of the far-right regions were omitted for visual clarity. b) Shows the mean DSSIM signal of each region versus time. The green dots mark the maximum for each region. c) Shows the progression of the global regional DSSIM maximums for front 1. Front 1 shows a linear velocity. 37

Figure 2.8 Visualization and quantification of fiber foci dynamics. (a) Image was divided into 70 overlapping regions, each 400 nm thick, based on distance from the electrode. The dashed line shows the size of 1 region. The color gradient shows the distance from the electrode for each of the 70 regions, with purple being closest to the electrode and yellow the furthest. (b) Mean DSSIM signal of each region versus time. The green dots mark the maximum dissimilarity for each region. (c) Progression of the regional DSSIM maximums for both front 1 (Figure 2.7) and front 2. Front 1 shows a linear velocity while front 2 is accelerating. 38

Figure 2.9 Dissimilarity images from DSSIM analysis with all assembly front labeled. Bright pixel values correspond to regions of high dissimilarity between frames. Top time labels correspond to the times (seconds) of the two Liquid EM images used to calculate the DSSIM image. 38

Figure 2.10 Summation of all DSSIM images. This shows the entire history of change within the viewing area and shows that the greatest amount of change occurs within ~1000 nm of the electrode. 38

Figure 2.11 Image filtering and normalization steps of select images, calculated from Eq 1-4. ……………..42

Figure 2.12 Each panel shows CLSM image (t) on the top and (t + Δt) on the bottom, with resulting DSSIM(t ,t + Δt) image between. Left column, 90 s temporal offset. Right column, 3.75 s offset. …………44

Figure 2.13 Active dynamic self-assembly fueled by electricity. (a) Processed CLSM snapshots highlighting the high dynamics for self-assembly at the gel front (details in Supporting Information). (b) Structural dissimilarity frame series generated by calculating the DSSIM of CLSM frames taken 90 s apart. Bright pixels represent regions of high structural dissimilarity between local areas in frames of comparison, which corresponds to fiber dynamics. (c–e) Snapshots showing different active fiber movements: simultaneous fiber growth and shrinkage ((c) green arrow for growing fiber and red for shrinking), waving (d), and curling/looping (e) (CLSM images rendered with γ = 0.45 and 150% hue saturation for fiber visualization). (f) Mean DSSIM in each region seen in (b). (The working electrode for (a–e) is out of frame on the left. Scale bar = 20 μm for (c–e). ……………………………………………………………………………………...46

Figure 2.14 Intensity analysis of normalized CLSM images and high temporal resolution DSSIM images. a, CLSM snapshots highlighting the high dynamics for self-assembly at the gel front, processed with Eqs 1-4. b, DSSIM frame series of images takes 3.75 s apart, which captures fast dynamics. c, mean normalized intensity in each region show in a. d, mean DSSIM in each region seen in b. ……………………………………….47

Figure 2.15 Comparison of raw signal to filtered signal used in Figure 2.13 and Figure 2.14f. Filtering was applied to smooth the signal via convolution of a normalized Gaussian Eq 7. …………………………………….48

Figure 3.1 Chemically-fueled dissipative self-assembly. Left shows the sequential process separated into the forward assembly reaction and backward disassembly reaction. Right shows the combined synchronous reaction. ……………………………………………………………………………………………………….54

Figure 3.2 Image processing pipeline for stacked fiber phase segmentation. The image processing steps are outlined for a representative image. A more detailed description of each step can be found in the text below. The templates have been increased in size for display purposes. ……………………………………………57

Figure 3.3 Individual segmentation maps for template pixel spacings of 15, 20, and 25 pixels. The templates have been increased in size by 4x for display purposes. The right figure shows an overlay of the 3 individual maps and demonstrates how different template spacings are used to identify different fiber stack spacings in the image. Note some highlighted regions are single fibers and not fiber stacks, these will be removed from the dataset during fiber stack labeling. ………………………………………………………………57

Figure 3.4 Defocus correction for segmentation algorithm. A) Typical TEM image with B) corresponding FFT image. Blue line represents radial integration of the FFT, with the green dot labeling the calculated second-peak distance. C) Examples of several radially integrated FFTs from images at different defocuses with the calculated second-peak distance. D) Calibration curve which relates defocus value to the calculated second-peak distance. Points below 7 μm were omitted from the fit. E) Empirically determined curve which adjusts probability threshold for segmentation as a function of image defocus. F) Mean segmented pixels of images across different defocus ranges. There was a clear correlation in the uncorrected curve which has been removed in the corrected curve. Dashed line represents linear fit. Error bars represent standard deviation. G) Uncorrected image with threshold of .145 showing over segmentation compared to H) segmentation after defocus threshold correction. …………………………………60

Figure 3.5 Labeling degree of stacking. A,B) snapshots of integrated profiles at different locations in the fiber stack. Fibers are labeled with orange dots. C,D) The number of fibers at each location is then counted and labeled. ……….61

Figure 3.6 Quantitative image analysis of the stacked fiber phase. (A–D) Selection of labeled frames from key timepoints. Colored tinting corresponds to the degree of stacking. F = forward, B = backward, S = synchronous. (E) Mean DoS for each timepoint, high values indicate higher order in the system. Black error bars represent 95% confidence interval of mean. (F) DoS datapoint distribution normalized to 1 for comparison between timepoint. Scale bars 300 nm. ……………………………………………………………………….64

Figure 3.7 Examples of labeled images. ………………………………………………………………………………………65

Figure 3.8 Display of Figure 3.6E with the mean combined DoS labeled for each timepoint (green dots. ………..66

Figure 3.9 Density distribution of each timepoint, defined as the total number of labeled pixels divided by the total number of pixels in each timepoint. Black dots represent standard deviation of image densities within each timepoint. (*) represents standard deviation points omitted for visibility. ………………………….66

Figure 4.1 Schematic of the two pathways observed during bilayer formation. (a) Vesicle spreading: the block copolymers were observed to form vesicles that grew, ruptured, and spread to form supported bilayers. (b) Droplet spreading: the block copolymers were observed to undergo liquid–liquid-phase separation to form droplets that spread over the surface to form supported bilayers. …………………………72

Figure 4.2 Image processing pipeline for particle segmentation. The image processing steps are outlined for a representative image, which are described in more detail in the text above. This pipeline was applied to each particle of the study individually. ……………………………………………………………………………………75

Figure 4.3 Vesicle spreading during bilayer formation. (a) Time series of Video 1: the colored arrows indicate each vesicle that was analyzed further, and the red dashed box highlights detector artifacts. (b) Time series of individual vesicles in Video 1 (15 e–/nm2·s). Colored outlines correspond to the arrows. (c) The area evolution of each vesicle shown above. The dashed line indicates a linear fit. (d) Ratio of average membrane contrast to membrane diameter. (e) The evolution of the spread rate for each vesicle shown above. ……76

Figure 4.4 Gaussian-Weighted sliding average for signal filtering prior to derivative calculation. Left shows unfiltered area calculation, while right shows the filtered signal which was used for the derivative calculation shown in Figure 4.3. ……………………………………………………………………………………………………77

Figure 4.5 Quantitative analysis of a particle in each control experiment. ……………………………………………78

Figure 4.6 Image processing pipeline for defining particle perimeter from binary map. A combination of polar and cartesian transforms were used to define a continuous perimeter of each particle. The images above demonstrate how this works when there is a significant gap in the vesicle. The colormap produced from the column averaging in polar space was mapped to the perimeter based on angular position in cartesian space. ………80

Figure 4.7 Membrane analysis of vesicle (V1). (a) Snapshots of the LCTEM Video 1 during the solvent exchange process. The outline intensity shows the integrity of the membrane; a high intensity of detected electrons means the membrane has been ruptured in that area. (b) Angular intensity map of the vesicle pictured above (more details in the SI). The red arrows correspond to the individual areas in the vesicle membrane where the rupture was observed. (c) Overlayed particle outlines for the selected frame (top) and all frames (bottom). ……81

Figure 4.8 Comparison of angular intensity map for different radial distances. Top shows the angular intensity map for the mean intensity values within 11 pixels (70 nm) of the perimeter in the polar transform. Center shows the angular intensity map for the mean intensity values from the perimeter to the center of mass pixel, average of 35 pixels (222 nm). Bottom shows the angular intensity map for the mean intensity values from the center of mass pixel to 11 pixels before the perimeter (the center of the vesicle excluding the membrane). All images are displayed on the same contrast boundaries. 82

Figure 4.9 Comparison of angular intensity map for different perimeter definitions. Top shows the angular intensity map for the mean intensity values within 11 pixels (70 nm) of the continuous perimeter in the polar transform (Figure 4.7b). Bottom shows the angular intensity map for the mean intensity values within 11 pixels (70 nm) of the discontinuous perimeter (details in Vesicle Segmentation section) in the polar transform. 83

Figure 4.10 LCTEM analysis of droplet spreading during bilayer formation. (a) Snapshots of the LCTEM Video 2 (11 e–/nm2·s) during the solvent exchange process. The blue and red boxes highlight examples of pristine bilayer formation and defect formation, respectively. (b) Close view of two droplets completely fusing together to form a homogeneous bilayer along with the cross-sectional time series of the highlighted green box to show a homogeneous bilayer area. (c) Close view of two droplets merging to form a bilayer boundary along with the cross-sectional time series of the highlighted green box to visualize boundary formation. 85

Figure 4.11 Percent coverage of the bilayer in the viewing area for the last frame of Video 2. The covered area was segmented manually and given a green tint in the right image. 86

Figure 5.1 A) LCTEM frame-series of dark polymer-rich liquid droplets nucleating, coalescing, and spreading under continuous irradiation from the beam. B) Polymer-rich droplet spreading while the beam is periodically blanked and unblanked. Time labels are experiment time. C) Frame-series of cropped images from droplet spreading shown in B). The green line labels the interface between the polymer-rich droplets and polymer-poor continuous phase. D,E) Boundary distance relative to the location in the first frame plotted as a function of experiment time (D) and beam irradiation time (E). 95

Figure 5.2 A,B) Selected images from dose study of complex liquid structures with continuous irradiation (A) and pulsed irradiation (B). Green arrows indicate internal droplet coalescence and orange arrows indicate external droplet coalescence. Time labels are experiment time. C,D) Normalized image intensity of frame-series for each dose study plotted against experiment time (C) and exposure time (D). Frame-series shown in A,B) are distinguished with dashed lines. 96

ACKNOWLEDGEMENTS

I would like to thank my parents for all their love and support. Thank you for driving me to all the volleyball practices, band practices, science Olympiad events, boy scout event, ect. You gave me complete freedom to pursue my passions from a young age and that has directly resulted in my love and pursuit of science. Thank you.

I would like to thank several of my teachers that held me to extremely high standards and went out of their way to offer support to me in my formative years. Among others this includes Aaron Morgan, Leeanne Branham, Denise DenHartog, Brian Hunter, Dr. Ellen Melocik, and Coach Bob McCarthy. Special thanks to Coach Gavin Gladding for being an incredible teacher, coach, and mentor.

I would like to thank Adam J. Moule for accepting me into his group during my undergraduate education at UC Davis. You provided me with so much guidance and support, the weekly undergraduate meeting was the best part of my week. Thank you. I would also like to thank the Moule research group as a whole for teaching me how to do science and for being patient through my initial year(s) of failure. I would specifically like to thank Dr. Tucker Murrey, Dr. Zaira Bedolla-Valdez, Goktug Gonel, and Dr. Thomas Harrelson for teaching me how to be an experimentalist and encouraging me to apply for graduate school.

I would like to thank all of the friends I made in Irvine. You know who you are. Irvine is the most barren and soulless city I have ever seen in my life. You guys made this place feel like home, and this was the strongest community I have ever been a part of. I will miss those Friday nights at Eureka.

I would like to thank all current and former members of the Patterson Lab. It has been a one-of-a-kind experience working with you all and I am happy I was part of this lab for my PhD. If I list any names, I'll have to list them all, so I'll just list them all. Dr. Rakia Dhaoui, Dr. Aoon Rizvi, Ben Rose, Dr. Paul Hurst, Dr. Giuseppe Di Palma, Nehal Idris, Lilian Zeinalvand, Riya Singh, Dr. Brooke Carpenter, Pushp Raj Prasad, Elmira Baghdadi, Wyeth Gibson, Elisa Olivas, Dr. Rain Talosig, Zhaoxu Li, Jovany Merham, Katen Iyer, Redford Hudson. It was an absolute pleasure working with you all and my PhD would not have been possible without you guys.

I would like to specifically acknowledge Dr. Aoon Rizvi for providing me several years of mentorship. Your enthusiasm for science is incredible and your ability to perform and present interdisciplinary science is an inspiration. It was a privilege to work with you and learn from you. I would also like to thank Jovany Merham for teaching me how to code very early on in my PhD. I have used the lessons you taught me in every project I've ever completed and passed them on to many others.

I would like to thank my advisor Joe Patterson, for the thousands of slack messages you responded to immediately, for the hundreds of hours we have spent in meetings together (I conservatively estimate 900 hours of meetings), for all the ideas you have helped me develop, for the countless early mornings and weekends of work you have put in to making the Patterson Lab and my PhD a success. The group you have created is one of a kind, and I am so grateful to have been a part of it. You have given me many hard challenges, but the hardest will be trying to find a mentor to replace you. Thank you.

I acknowledge the donors of The American Chemical Society Petroleum Research Fund. I acknowledge funding as part of Ensembles of Photosynthetic Nanoreactors (EPN), an Energy Frontier Research Center funded by the U.S. Department of Energy, Office of Science (DE-SC0023431). I also acknowledge the use of facilities and instrumentation at the UC Irvine Materials Research Institute (IMRI) supported in part by

the National Science Foundation Materials Research Science and Engineering Center program through the UC Irvine Center for Complex and Active Materials (DMR-2011967). Portions of chapter 3 utilized the infrastructure for high-performance and high throughput computing, research data storage and analysis, and scientific software tool integration built, operated, and updated by the Research Cyberinfrastructure Center (RCIC) at the University of California, Irvine (UCI). The RCIC provides cluster-based systems, application software, and scalable storage to directly support the UCI research community.

Chapter 1 of this dissertation is a reprint of the material as it appears in “Correlating Electrochemical Stimulus to Structural Change in Liquid Electron Microscopy Videos using the Structural Dissimilarity Metric” Ultramicroscopy 2024, 257, 113894, used with permission from Elsevier. The co-authors listed in this publication are JT Mulvey, KP Iyer, T Ortega, JG Merham, Y Pivak, H Sun, AI Hochbaum, JP Patterson.

Portions of Chapter 2 of this dissertation is a reprint of the material as it appears in “Observing the dynamics of an electrochemically driven active material with liquid electron microscopy” ACS Nano. 2024, 18 (18), 11898–11909, used with permission from American Chemical Society. The co-authors listed in this publication are WS Gibson, JT Mulvey, S Das, S Selmani, JG Merham, AM Rakowski, E Schwartz, AI Hochbaum, Z Guan, JR Green, JP Patterson.

Portions of Chapter 2 of this dissertation is a reprint of the material as it appears in “Electrically Fueled Active Supramolecular Materials” J. Am. Chem. Soc. 2022, 15 (3), 1106–1116, used with permission from American Chemical Society. The co-authors listed in this publication are S Selmani, E Schwartz, JT Mulvey, H Wei, A Grosvirt-Dramen, W Gibson, AI Hochbaum, JP Patterson, R Ragan, Z Guan.

Chapter 3 of this dissertation is an adaptation of the material as it appears in “CryoEM reveals the complex self-assembly of a chemically driven disulfide hydrogel” Chem. Sci. 2024, 15 (3), 1106–1116, used with permission from Royal Society of Chemistry. The co-authors listed in this publication are PJ Hurst, JT Mulvey, RA Bone, S Selmani, RF Hudson, Z Guan, JR Green, JP Patterson.

Chapter 4 of this dissertation is a reprint of the material as it appears in “Observation of Liquid–Liquid-Phase Separation and Vesicle Spreading during Supported Bilayer Formation via Liquid-Phase Transmission Electron Microscopy.” Nano Lett. 2021, 21, 24, 10325–10332, used with permission from American Chemical Society. The co-authors listed in this publication are A Rizvi, JT Mulvey, JP Patterson.

VITA

Justin T Mulvey

Education

PhD Materials Science and Engineering, University of California, Irvine (Spring 2021 - Summer 2024)

M.S. Materials Science and Engineering, University of California, Irvine, (Fall 2019 – Spring 2021)

B.S. Materials Science and Engineering, University of California, Davis, (Fall 2015 – Spring 2019)

Research Experience

Ph.D. Research, UC Irvine, Dept. of Materials Science and Engineering (Fall 2019 – Summer 2024)

Materials science research at the interface of microscopy and image science.

Advisor: Dr. Joseph P. Patterson, Dept. of Chemistry

Junior Research Fellow of UC Irvine NSF MRSEC: Center for Complex and Active Materials (CCAM). (2020-2022)

Junior Research Fellow of UC Irvine DoE EFRC: Ensembles of Photosynthetic Nanoreactors (EPN). (2022-2024)

- Developed, evaluated, and published computational image analysis pipelines to: processing raw microscopy images and video, extract and statistically quantify feature of interest, and clearly visualize results to general audience (8 publications submitted/accepted)
- Implemented image analysis techniques: object segmentation, background subtraction, feature labeling, structural change analysis, Fourier transform filtering and analysis, EDS signal averaging, quantitative contrast analysis, machine learning denoising, principal component analysis.
- Expertise in performing microscopy techniques and image interpretation: transmission electron microscopy (TEM), high-resolution TEM, in situ liquid-cell TEM, scanning TEM EDS, optical confocal microscopy, atomic force microscopy, scanning electron microscopy. PRFICIENCY IN:
- Proficiency in materials systems: amphiphilic block-copolymer self-assembly, dissipative/fuel driven polymer self-assembly, inorganic photoactive nanocrystals (TiO_2,STO), organic semiconductors (P3HT, PBTTT).
- Proficiency performing computation analysis on high performance cluster (UC Irvine HPC3).

Undergraduate Research, UC Davis, Dept. of Chemical Engineering (Spring 2017- Spring 2019)

Advisor: Dr. Adam J. Moulé, Dept. of Chemical Engineering

- Optimized procedure for spin coating organic semiconductor films on ITO substrate, evaporating silver electrodes onto the film surface, and evaluating in-plane conductivity with 4-bar conductivity measurements. (published)
- Built and optimized in-house microscope apparatus to focus a laser through a custom photomask and selectively heat semiconducting polymer film to produce photothermal, micron-scale patterns which were characterized with atomic force microscopy. (published)
- Developed Matlab program to subtract background and measure integrated line profile of photothermal patterns from atomic force microscopy images.

Undergraduate Research, UC Davis, Dept. of Materials Science and Engineering (Spring 2018 - Fall 2018)

Advisor: Dr. Susan P. Gentry, Dept. of Materials Science and Engineering

- Independently designed and conducted experiments attempting to determine tension force in slackline (tensioned tubular nylon webbing) based on reflected in-line wave speed measured with stopwatch.
- Produced and reported empirical equation to the slackline community which relates slackline tension to wave speed, line density, and empirical 'energy dissipation' factor which depend on slackline webbing model.

Technical Skills

Laboratory skills: Transmission electron microscopy (TEM) (UCI IMRI, ~400 hours hands-on, JOEL 2100F and JOEL 2800), in situ liquid-cell TEM, high-resolution TEM, scanning TEM EDS, optical confocal microscopy (Zeiss LSM 900), atomic force microscopy, scanning electron microscopy, standard wet-lab skills and safety, machine shop experience using mill and lathe.

Software skills: Matlab (~3000 hours), Python (~500 hours), ChatGPT, ImageJ, Linux, high performance cluster (UCI HPC3, CentOS), Adobe Illustrator and Photoshop, AutoCAD, Microsoft Suite

Publications

1. JT Mulvey, KP Iyer, T Ortega, JG Merham, Y Pivak, H Sun, AI Hochbaum, JP Patterson. Correlating Electrochemical Stimulus to Structural Change in Liquid Electron Microscopy Videos using the Structural Dissimilarity Metric. *Ultramicroscopy* (2024) doi.org/10.1016/j.ultramic.2023.113894
2. PJ Hurst, JT Mulvey, RA Bone, S Selmani, RF Hudson, Z Guan, JR Green, JP Patterson. CryoEM Reveals the Complex Evolution of a Thermodynamically Unstable Phase in the Chemically Fueled Dissipative Assembly of a Disulfide Hydrogel. *Chemical Science* (2024) doi.org/10.1039/D3SC05790A
3. WS Gibson, JT Mulvey, S Das, S Selmani, JG Merham, AM Rakowski, E Schwartz, AI Hochbaum, Z Guan, JR Green, JP Patterson. Observing the dynamics of an electrochemically driven active material with liquid electron microscopy. *ACS Nano* (2024) doi.org/10.1021/acsnano.4c01524
4. A Rizvi, JT Mulvey, JP Patterson. Observation of Liquid–Liquid-Phase Separation and Vesicle Spreading during Supported Bilayer Formation via Liquid-Phase Transmission Electron Microscopy. *Nano Lett.* (2021) doi.org/10.1021/acs.nanolett.1c03556. co-first author
5. S Selmani, E Schwartz, JT Mulvey, H Wei, A Grosvirt-Dramen, W Gibson, AI Hochbaum, JP Patterson, R Ragan, Z Guan. Electrically Fueled Active Supramolecular Materials. *J. Am. Chem. Soc.* (2022) doi.org/10.1021/jacs.2c01884
6. R Dhaoui, SL Cazarez, L Xing, E Baghdadi, JT Mulvey, NS Idris, PJ Hurst, MP Vena, GD Palma, JP Patterson. 3D Visualization of Proteins within Metal–Organic Frameworks via Ferritin-Enabled Electron Microscopy. *Adv. Functional Mats.* (2024) doi.org/10.1002/adfm.202312972
7. A Rizvi, JT Mulvey, BP Carpenter, R Talosig, JP Patterson. A Close Look at Molecular Self-Assembly with the Transmission Electron Microscope. *Chem. Rev.* (2021) doi.org/10.1021/acs.chemrev.1c00189

8. DR Lustig, E Buz, JT Mulvey, JP Patterson, KR Kittilstved, JB Sambur. Characterizing the Ligand Shell Morphology of PEG-Coated ZnO Nanocrystals Using FRET Spectroscopy. *J. Phys. Chem. B* (2023) doi.org/10.1021/acs.jpcb.3c04900.
9. DR Lustig, ZN Nilsson, JT Mulvey, W Zang, X Pan, JP Patterson, JB Sambur. Toward Imaging Defect-Mediated Energy Transfer between Single Nanocrystal Donors and Single Molecule Acceptors. *Chemical & Biomedical Imaging* (2023) doi.org/10.1021/cbmi.3c00015
10. AR Talosig, F Wang, JT Mulvey, BP Carpenter, EM Olivas, BB Katz, C Zhu, JP Patterson. Understanding the Nucleation and Growth of ZIF-8 Polymorphs. *Crystal Growth & Design* (2024) doi.org/10.1021/acs.cgd.4c00194
11. TL Murrey, JT Mulvey, M Jha, AS Fergerson, D Vong, A Soika, J Lorek, SE Dolan, DR Tiffany-Appleton, AJ Moulé. Approaching Rapid, High-Resolution, Large-Area Patterning of Semiconducting Polymers Using Projection Photothermal Lithography. *Adv Materials Technologies* (2022) doi.org/10.1002/admt.202100812
12. BP Carpenter, AR Talosig, JT Mulvey, JG Merham, J Esquivel, B Rose, AF Ogata, DA Fishman, JP Patterson. Role of Molecular Modification and Protein Folding in the Nucleation and Growth of Protein–Metal–Organic Frameworks. *Chem. Mater.* (2022) doi.org/10.1021/acs.chemmater.2c01903
13. TL Murrey, K Guo, JT Mulvey, OA Lee, C Cendra, ZI Bedolla-Valdez, A Salleo, JF Moulin, K Hong, AJ Moulé. Additive Solution Deposition of Multi-Layered Semiconducting Polymer Films for Design of Sophisticated Device Architectures. *J. Mater. Chem. C* (2019) doi.org/10.1039/C8TC05652H

Conference Talks and Posters

1. Talk: Microscopy and Microanalysis Annual meeting, (2023)
2. Talk: Gordon Research Seminar: Liquid Phase Electron Microscopy, (2022)
3. Poster: DoE-EFRC-Hub-CMS-CCS PI Meeting, (2023)
4. Poster: Gordon Research Seminar: Liquid Phase Electron Microscopy, (2022)
5. Poster: Gordon Research Seminar: Image Science, (2022)
6. Poster: UC Davis Engineering Senior Design Symposium (2019)
7. Poster: MRS Boston Fall Conference and Exhibition, (2018)
8. Poster: ACS Undergraduate Research Symposium, Mills College, (2018)

Awards and Fellowships

UC Irvine, Materials Science and Engineering Elevator Pitch Competition, 3rd place (2023 and 2024)

5th international Symposium on Advanced Microscopy and Spectroscopy, 2nd place poster award

MRS Science as Art Competition, 1st place (2022)

NSF GRFP, Honorable Mention (2020)

UC Davis, Materials Science and Engineering Department Citation (top 3 in class) (2019)

UC Davis, University thesis-based honors program (2016-2019)

UC Davis, Department honors program (2016-2019)

UC Davis, Recipient of Wasson Family Scholarship (2016,2017)

Professional Experience

UC Davis Outdoor Adventure — Davis, California, USA

UC Davis Campus Rock Wall Manager — Summer 2017 – Spring 2019

- Managed hiring, training, and scheduling for 10-person student staff to safely supervise rock climbing wall.
- Established dedicated route-setting shifts to better organize staff and ensure new hires were supervised and properly trained for best safety practices while changing routes.
- Organized monthly safety inspections of all climbing equipment and convinced management to invest in new floor padding to prevent guest injury.

Teaching, Mentorship, and Outreach

Teaching Assistant: Analytical Methods for Organic Nanomaterials (2020-2022) (Three quarters). Designed 3-part lecture series for using ImageJ to segment and analyze structures from TEM image datasets.

Teaching Assistant: Upper Division Thermodynamics of Materials, (2022) (One quarter). Designed lectures for weekly discussion and graded quizzes and exams.

Mentored 4 undergraduate researchers from multiple backgrounds (Computer Science, Chemistry, Materials Science and Engineering) culminating in co-authorship across 3 publications.

Mentored 2 new PhD students including training in TEM, in situ Liquid Cell TEM, and Computational Image Analysis (ImageJ, Matlab, Python).

Outreach:

- EPN microscopy bridge, supervised 2 undergraduate students imaging their samples with TEM (2023)
- EPN microscopy bridge, 2 lectures about different types of microscopy and graduated studies in microscopy (2022)
- MRSEC MSPIRE, graduate panel for high school/undergraduate students (2022)
- MRSEC Foldscope module: Developed education video and accompanying worksheet for high school foldscope microscopy lesson plan (2021)
- MSE “Cooking with Science”, zoom event teaching materials science to elementary school students (2020)

Miscellaneous

Rock climber for 10 years with ascents in Yosemite, Whitney Wilderness, and Red Rocks NV

Musically trained in classical guitar and percussion (marimba, vibraphone)

Adventure photography

Indoor volleyball (2010-present)

Eagle Scout, conferred 2015

ABSTRACT OF THE DISSERTATION

Deterministic Image Analysis for In Situ Transmission Electron Microscopy

by

Justin T Mulvey

Doctor of Philosophy in Materials Science and Engineering

University of California, Irvine, 2024

Assistant Professor Joseph P. Patterson, Chair

In situ transmission electron microscopy enables the study of nanoscale solution state events such as battery electrode deposition and molecular self-assembly. Recent improvements in electron microscope detectors have vastly improved the spatial resolution (pixel count) and temporal resolution (frame rate) of microscopy videos, which has resulted in large, information-rich datasets. The central mission of my PhD has been to use image analysis techniques and algorithms to translate improvements in microscopy signal collection to improvements in materials insight. Towards this, I have developed several novel image analysis algorithms built on deterministic image science methods which extract quantitative information from raw microscopy datasets. I developed an algorithm to quantify materials dynamics captured with in situ microscopy videos and applied this algorithm to quantify the spatiotemporal dynamics of dissipative self-assembly processes (Chapters 1-2). I applied image science to track the presence of an unstable phase captured in time-resolved cryogenic transmission electron microscopy (Chapter 3). And finally, I applied a variety of custom image analysis algorithms to quantify amphiphilic block copolymer morphological transitions such as vesical-to-bilayer transitions, droplet-to-bilayer transitions, and droplet dissolution dynamics (Chapters 4-5). In each case, I demonstrate the power of deterministic image analysis methods for converting raw microscopy datasets into interpretable materials science results.

INTRODUCTION

The following dissertation is a collection of works centered on deterministic image analysis for transmission electron microscopy (TEM).[1–5] My body of work also includes publications which focus entirely on TEM data collection,[6,7] and publications which focus entirely on spectroscopic data science.[8,9] I believe that my background in materials science and my experience as a microscope operator directly strengthened my ability to perform data analysis. First, my knowledge of microscopy and spectroscopy made it much easier to communicate with my colleagues and understand the instrument-specific artifacts which may be present in the data. I also believe it was much easier for me to mine the data for information relevant to the broader study, and present findings to the audience in a way that directly strengthened scientific arguments or directly answered scientific questions. Finally, knowledge of microscopy enabled me to design studies from the ground up with data science in mind, leading to several interdisciplinary studies which merge the fields of microscopy, materials science, and data science. Ultimately, I strongly encourage researchers in both microscopy and materials science to investigate data science techniques and begin to incorporate these methods into future studies.

0.1 Transmission electron microscopy techniques

The TEM offers a diverse set of characterization tools for nanoscale structures.[1] TEMs generate images by transmitting a beam of electrons through the sample which is then collected by a detector. Electron-sample interactions generate contrast in the image, which can be used to resolve sub-nanometer features.[2] There are several methods for imaging solution-state processes using specialized preparation techniques and sample holders. Specialized in situ liquid cell TEM (LCTEM) holders can capture a sample's response to a variety of external stimuli such as changes in solvent composition, temperature, or electrical bias (Chapters 1,2,4,5).[3,4] This makes it possible to record movies of nanoscale dynamic processes in solution, which is not otherwise possible. There have been recent improvements in resolution and frame rate of electron detectors. 4k x 4k image resolution is now standard, with frame rates often reaching 100 frames per second enabling dynamics to be captured with high spatial and temporal resolution.[1] LCTEM experiments often generate terabyte-scale image datasets exceeding 10,000 frames. While this vastly increases the amount of structural information captured, the dynamics captured in these videos are difficult to interpret and quantify. Thus, automated image analysis methods are essential for characterizing processes captured in LCTEM. In addition, cryogenic transmission electron microscopy (cryoTEM) can also be used to study solution state processes (Chapter 3).[1] In cryoTEM, the solution sample is rapidly frozen, or vitrified, which makes it possible to image snap-shots of the system during individual time points in a process. An advantage of cryoTEM over LCTEM is that cryoTEM provides higher-resolution structural information on the system, and several images can be taken of the sample at different locations, rather than the single location imaged in LCTEM. Modern software designed for cyroTEM allows for automated data collection routines, which generate vast libraries of information rich image datasets. Again, these datasets benefit greatly from automated image analysis routines that are able to convert the raw data into easily interpretable results.

0.2 Convergence of advanced microscopy and data science

Signal processing and image processing are becoming increasingly important parts of modern transmission electron microscopy studies. Originally, TEM images were collected on photographic film where no numerical signal processing was possible.[5] Subsequently, more advanced techniques such as scanning transmission electron microscopy-energy dispersive X-ray spectroscopy (STEM-EDS) and STEM-electron energy loss spectroscopy (STEM-EELS) were developed which captured more complex signals in the TEM to provide local chemical information about the sample.[6] These techniques generate multiple signal types that must be collected simultaneously and assembled into multidimensional files. These signals must then be processed with methods such as background subtraction and spectrum peak integration before they can be displayed as an image. In modern TEM, advanced techniques such as 4D-

STEM are gaining popularity in which each beam scan position contains a 2D diffraction pattern.[7] Such a technique requires extremely fast data-transfer speeds and complex reconstruction algorithms in order to extract meaningful insight from the data. I believe cutting-edge techniques such as this represent a convergence for the fields of microscopy and data science, where strong knowledge in both fields is required to conduct a study.

0.3 Defining a microscope image

Microscope images are the combination of a numerical 2D signal and a colormap.[8] Fundamentally, a microscope is an instrument which uses a detector to collect a signal coming from the sample. The microscope will then arbitrarily assign a colormap to this signal in order to display the signal to the microscope operator as an image. Importantly, the assignment of colormap by the microscope is completely arbitrary. The microscope operator should always adjust the colormap of the signal (by adjusting brightness and contrast) to best display the signal of interest in the image. Because colormap assignment is completely arbitrary, there is no such thing as a “raw image”, only a raw signal. I politely encourage manuscript reviewers to stop requesting “raw images”, as this term carries no real meaning. The image provided by the microscope is not a raw image, it is a raw signal with an arbitrary colormap. In the text that follows, all analysis was applied to the raw signal of the collected datasets. In most cases, the datasets were 2D double precision floating point values which contain more information than an 8-bit grayscale image. Note that while the words “image processing” and “image analysis” are used throughout the thesis, all algorithms and analysis were conducted on the raw signals that compose the images.

0.4 Summary of chapters

In the following chapters I will describe a series of image analysis algorithms I developed to quantify microscopy datasets. In Chapter 1 I present structural dissimilarity (DSSIM) analysis as a new video processing algorithm for quantifying structural change occurring in LCTEM videos.[9] I show the algorithm can be used to correlate electrical biasing data to structural change occurring in the microscope. In Chapter 2 I apply DSSIM analysis to quantify an electrically fueled dissipative self-assembly process in LCTEM and confocal laser scanning microscopy (CLSM) datasets.[10,11] In the LCTEM dataset, the analysis reveals a wave-like propagation of self-assembly which is then tracked and quantified. The analyses also show a strong spatial relationship between the self-assembly process and the electrode. In Chapter 3, I apply a cross-correlation algorithm to a time-resolved cryoTEM datasets to track the presence of a thermodynamically transient stacked-fiber phase.[12] In Chapter 4, I apply a series of algorithms to quantify bilayer formation via two pathways captured in LCTEM.[13] In the first pathway, I track the rupture and spread of a vesicle transitioning to a bilayer on the LCTEM window. In the second pathway, I track polymer rich liquid droplets which coalesce and spread as they transition to a bilayer on the LCTEM window. In Chapter 5, I present an experimental methodology and data analysis algorithm to quantify electron beam interactions with polymer-dense liquid structures in non-aqueous solvent systems.[14] Every chapter is based on published research, and the reader is directed to the full text document for a complete description of the materials system and experimental methodology. Each chapter will contain some information on the material system and major outcomes, but the focus of each chapter will be on the image processing, analysis methodology, and interpretation of results.

0.5 References

(1) Rizvi, A.; Mulvey, J. T.; Patterson, J. P. Observation of Liquid–Liquid-Phase Separation and Vesicle Spreading during Supported Bilayer Formation via Liquid-Phase Transmission Electron Microscopy. *Nano Lett.* **2021**, *21* (24), 10325–10332. https://doi.org/10.1021/acs.nanolett.1c03556.

(2) Hurst, P. J.; Mulvey, J. T.; Bone, R. A.; Selmani, S.; Hudson, R. F.; Guan, Z.; Green, J. R.; Patterson, J. P. CryoEM Reveals the Complex Self-Assembly of a Chemically Driven Disulfide Hydrogel. *Chem. Sci.* **2024**, *15* (3), 1106–1116. https://doi.org/10.1039/D3SC05790A.

(3) Mulvey, J. T.; Iyer, K. P.; Ortega, T.; Merham, J. G.; Pivak, Y.; Sun, H.; Hochbaum, A. I.; Patterson, J. P. Correlating Electrochemical Stimulus to Structural Change in Liquid Electron Microscopy Videos Using the Structural Dissimilarity Metric. *Ultramicroscopy* **2024**, *257*, 113894. https://doi.org/10.1016/j.ultramic.2023.113894.

(4) Dhaoui, R.; Cazarez, S. L.; Xing, L.; Baghdadi, E.; Mulvey, J. T.; Idris, N. S.; Hurst, P. J.; Vena, M. P.; Palma, G. D.; Patterson, J. P. 3D Visualization of Proteins within Metal–Organic Frameworks via Ferritin-Enabled Electron Microscopy. *Advanced Functional Materials* **2024**, *34* (13), 2312972. https://doi.org/10.1002/adfm.202312972.

(5) Gibson, W.; Mulvey, J. T.; Das, S.; Selmani, S.; Merham, J. G.; Rakowski, A. M.; Schwartz, E.; Hochbaum, A. I.; Guan, Z.; Green, J. R.; Patterson, J. P. Observing the Dynamics of an Electrochemically Driven Active Material with Liquid Electron Microscopy. *ACS Nano* **2024**, *18* (18), 11898–11909. https://doi.org/10.1021/acsnano.4c01524.

(6) Lustig, D. R.; Nilsson, Z. N.; Mulvey, J. T.; Zang, W.; Pan, X.; Patterson, J. P.; Sambur, J. B. Toward Imaging Defect-Mediated Energy Transfer between Single Nanocrystal Donors and Single Molecule Acceptors. *Chemical & Biomedical Imaging* **2023**, *1* (2), 168–178. https://doi.org/10.1021/cbmi.3c00015.

(7) Lustig, D. R.; Buz, E.; Mulvey, J. T.; Patterson, J. P.; Kittilstved, K. R.; Sambur, J. B. Characterizing the Ligand Shell Morphology of PEG-Coated ZnO Nanocrystals Using FRET Spectroscopy. *J. Phys. Chem. B* **2023**, acs.jpcb.3c04900. https://doi.org/10.1021/acs.jpcb.3c04900.

(8) Carpenter, B. P.; Talosig, A. R.; Mulvey, J. T.; Merham, J. G.; Esquivel, J.; Rose, B.; Ogata, A. F.; Fishman, D. A.; Patterson, J. P. Role of Molecular Modification and Protein Folding in the Nucleation and Growth of Protein–Metal–Organic Frameworks. *Chem. Mater.* **2022**, *34* (18), 8336–8344. https://doi.org/10.1021/acs.chemmater.2c01903.

(9) Talosig, A. R.; Wang, F.; Mulvey, J. T.; Carpenter, B. P.; Olivas, E. M.; Katz, B. B.; Zhu, C.; Patterson, J. P. Understanding the Nucleation and Growth of ZIF-8 Polymorphs. *Crystal Growth & Design* **2024**, *24* (10), 4136–4142. https://doi.org/10.1021/acs.cgd.4c00194.

(10) Rizvi, A.; Mulvey, J. T.; Carpenter, B. P.; Talosig, R.; Patterson, J. P. A Close Look at Molecular Self-Assembly with the Transmission Electron Microscope. *Chem. Rev.* **2021**, acs.chemrev.1c00189. https://doi.org/10.1021/acs.chemrev.1c00189.

(11) Kubota, R.; Tanaka, W.; Hamachi, I. Microscopic Imaging Techniques for Molecular Assemblies: Electron, Atomic Force, and Confocal Microscopies. *Chem. Rev.* **2021**, acs.chemrev.0c01334. https://doi.org/10.1021/acs.chemrev.0c01334.

(12) Omme, J. T. van; Wu, H.; Sun, H.; Beker, A. F.; Lemang, M.; Spruit, R. G.; Maddala, S. P.; Rakowski, A.; Friedrich, H.; Patterson, J. P.; Garza, H. H. P. Liquid Phase Transmission Electron Microscopy with Flow and Temperature Control. *J. Mater. Chem. C* **2020**, *8* (31), 10781–10790. https://doi.org/10.1039/D0TC01103G.

(13) Pu, S.; Gong, C.; Robertson, A. W. Liquid Cell Transmission Electron Microscopy and Its Applications. *Royal Society Open Science 7* (1), 191204. https://doi.org/10.1098/rsos.191204.

(14) Krivanek, O. L.; Mooney, P. E. Applications of Slow-Scan CCD Cameras in Transmission Electron Microscopy. *Ultramicroscopy* **1993**, *49* (1–4), 95–108. https://doi.org/10.1016/0304-3991(93)90216-K.

(15) Su, D. Advanced Electron Microscopy Characterization of Nanomaterials for Catalysis. *Green Energy & Environment* **2017**, *2* (2), 70–83. https://doi.org/10.1016/j.gee.2017.02.001.

(16) Ophus, C. Four-Dimensional Scanning Transmission Electron Microscopy (4D-STEM): From Scanning Nanodiffraction to Ptychography and Beyond. *Microscopy and Microanalysis* **2019**, *25* (3), 563–582. https://doi.org/10.1017/S1431927619000497.

(17) Zhou, L.; Hansen, C. D. A Survey of Colormaps in Visualization. *IEEE Trans. Visual. Comput. Graphics* **2016**, *22* (8), 2051–2069. https://doi.org/10.1109/TVCG.2015.2489649.

(18) Selmani, S.; Schwartz, E.; Mulvey, J. T.; Wei, H.; Grosvirt-Dramen, A.; Gibson, W.; Hochbaum, A. I.; Patterson, J. P.; Ragan, R.; Guan, Z. Electrically Fueled Active Supramolecular Materials. *J. Am. Chem. Soc.* **2022**, jacs.2c01884. https://doi.org/10.1021/jacs.2c01884.

(19) Mulvey, J. T.; Rizvi, A.; Patterson, J. P. Liquid Electron Microscopy with Non-Aqueous Solvents: Evaluating the Beam-Sample Interactions of Complex Liquid Structures. *Microscopy and Microanalysis* **2023**, *29* (Supplement_1), 1758–1760. https://doi.org/10.1093/micmic/ozad067.909.

CHAPTER 1: Correlating electrochemical stimulus to structural change in liquid electron microscopy videos using the structural dissimilarity metric

This Chapter was adapted from a published article (JT Mulvey, KP Iyer, T Ortega, JG Merham, Y Pivak, H Sun, AI Hochbaum, JP Patterson. “Correlating Electrochemical Stimulus to Structural Change in Liquid Electron Microscopy Videos using the Structural Dissimilarity Metric” Ultramicroscopy 2024, 257, 113894). © Elsevier 2024

1.1 Abstract

In-situ liquid cell transmission electron microscopy (LCTEM) with electrical biasing capabilities has emerged as an invaluable tool for directly imaging electrode processes with high temporal and spatial resolution. However, accurately quantifying structural changes that occur on the electrode and subsequently correlating them to the applied stimulus remains challenging. Here, we present structural dissimilarity (DSSIM) analysis as segmentation-free video processing algorithm for locally detecting and quantifying structural change occurring in LCTEM videos. In this study, DSSIM analysis is applied to two in-situ LCTEM videos to demonstrate how to implement this algorithm and interpret the results. We show DSSIM analysis can be used as a visualization tool for qualitative data analysis by highlighting structural changes which are easily missed when viewing the raw data. Furthermore, we demonstrate how DSSIM analysis can serve as a quantitative metric and efficiently convert 3-dimensional microscopy videos to 1-dimenional plots which makes it easy to interpret and compare events occurring at different timepoints in a video. In the analyses presented here, DSSIM is used to directly correlate the magnitude and temporal scale of structural change to the features of the applied electrical bias. ImageJ, Python, and MATLAB programs, including a user-friendly interface and accompanying documentation, are published alongside this manuscript to make DSSIM analysis easily accessible to the scientific community.

1.2 Introduction

In-situ liquid cell transmission electron microscopy (LCTEM) with biasing capabilities enables solution-state electrode processes to be recorded with nanoscale spatial resolution and millisecond-scale temporal resolution.[1-5] Direct observation of electric potential induced phenomena has contributed valuable mechanistic insights towards research in batteries,[6-9] catalysis,[10-13] and polymers.[14,15] The principal goal of many in-situ LCTEM electrochemical studies is to correlate the applied stimulus to structural changes captured in the video, such as material formation or dissolution. While structural changes may be visually apparent, raw LCTEM videos are often difficult to analyze for two main reasons. First, the liquid layer within the cell reduces object contrast in the images and introduces a large amount of noise into the data.[16] As a result, subtle structural changes are easily missed when viewing the raw data. Second, LCTEM videos collected on high-framerate microscopes can reach 1000's of frames in size, resulting in multiple terabytes of data.[17] Manually identifying and comparing events in the raw data can be extremely time-consuming and subjective. Thus, large datasets require efficient video analysis algorithms to detect and measure structural change events so they can be easily interpreted and correlated to the applied stimulus.

The most common method of quantitatively analyzing structural change is with image segmentation algorithms, in which objects are identified and analyzed in every image of the video.[18] This has been widely used in the LCTEM community to quantify dynamic events such as micelle fusion,[19] solid electrolyte interphase (SEI) layer growth,[6] nanoparticle etching,[20] and more.[21] However, in some datasets which contain multiple classes of objects or continuous objects, segmentation can be highly subjective or impossible. Recently, there have been segmentation-free analysis algorithms developed to measure structural change without the need to label objects in the images.[22] For example, an algorithm was developed to quantify beam-induced damage over time while imaging organic thin-films.[23] This was accomplished by using the normalized cross-correlation metric to compare the first frame and subsequent frames of an electron dose-series. The success of this method for characterizing a dynamic process unsuitable for segmentation analysis demonstrates the need for continued development of segmentation-free metrics. Here, we present a new segmentation-free video analysis algorithm to highlight and quantify structural change using the structural dissimilarity (DSSIM) metric, a linear variant of the commonly used structural similarity (SSIM) metric.[24]

DSSIM is an established measure of the perceived difference between two images, which compares local variation in the mean, standard deviation, and cross-correlation of pixel intensity values to produce a new dissimilarity image.[25,26] DSSIM was originally developed to assess the quality of structural information present in a reference and distorted image, such as comparing a raw image with a compressed image.[25] It was later adopted by the machine learning community as a metric to evaluate model performance by comparing a reconstructed image against a ground truth image.[27] The resulting dissimilarity image will highlight regions where the reconstruction image deviates the most from the ground truth image. To date, DSSIM has found several niche applications for structural analysis in the microscopy community. For example, DSSIM/SSIM has been used to identify: neurochemical events from cyclic voltammetry,[28] microcalcification from mammography,[29] crack formation from X-ray tomography,[30] phase changes in polarized optical microscopy,[31] and dynamic behavior in confocal fluorescence microscopy.[32] A recent LCTEM study used the metric to quantify beam-induced gold nanoparticle growth because segmentation analysis was not possible.[33] To quantify growth, they used SSIM to compare pairs of images taken of the same region in the liquid cell before and after electron irradiation.

For the first time, we apply the DSSIM metric to spatially and temporally quantify the stimulated structural changes captured in LCTEM electrochemistry videos. The proposed DSSIM analysis video algorithm compares temporally offset frames of the input video to create a dissimilarity video, which measures and highlights locations where structural change has occurred. In Section 1.3, we describe how to apply and tune the parameters of DSSIM analysis. In Section 1.4, we analyze two in-situ LCTEM datasets from different studies and show it is possible to extract quantitative, easy-to-interpret information and gain additional insight into electrochemically-driven materials formation and dissolution. For each dataset, we demonstrate DSSIM analysis can be used to evaluate the correlation between the applied stimulus and the resulting structural change.

1.3 Methods

1.3.1 DSSIM analysis workflow

Figure 1.1 describes the general workflow for applying DSSIM analysis to a video dataset. In step 1, the raw data is preprocessed to reduce noise in each frame prior to DSSIM analysis. In this study, noise is reduced by using frame averaging (temporal averaging) and Gaussian blurring (spatial averaging).

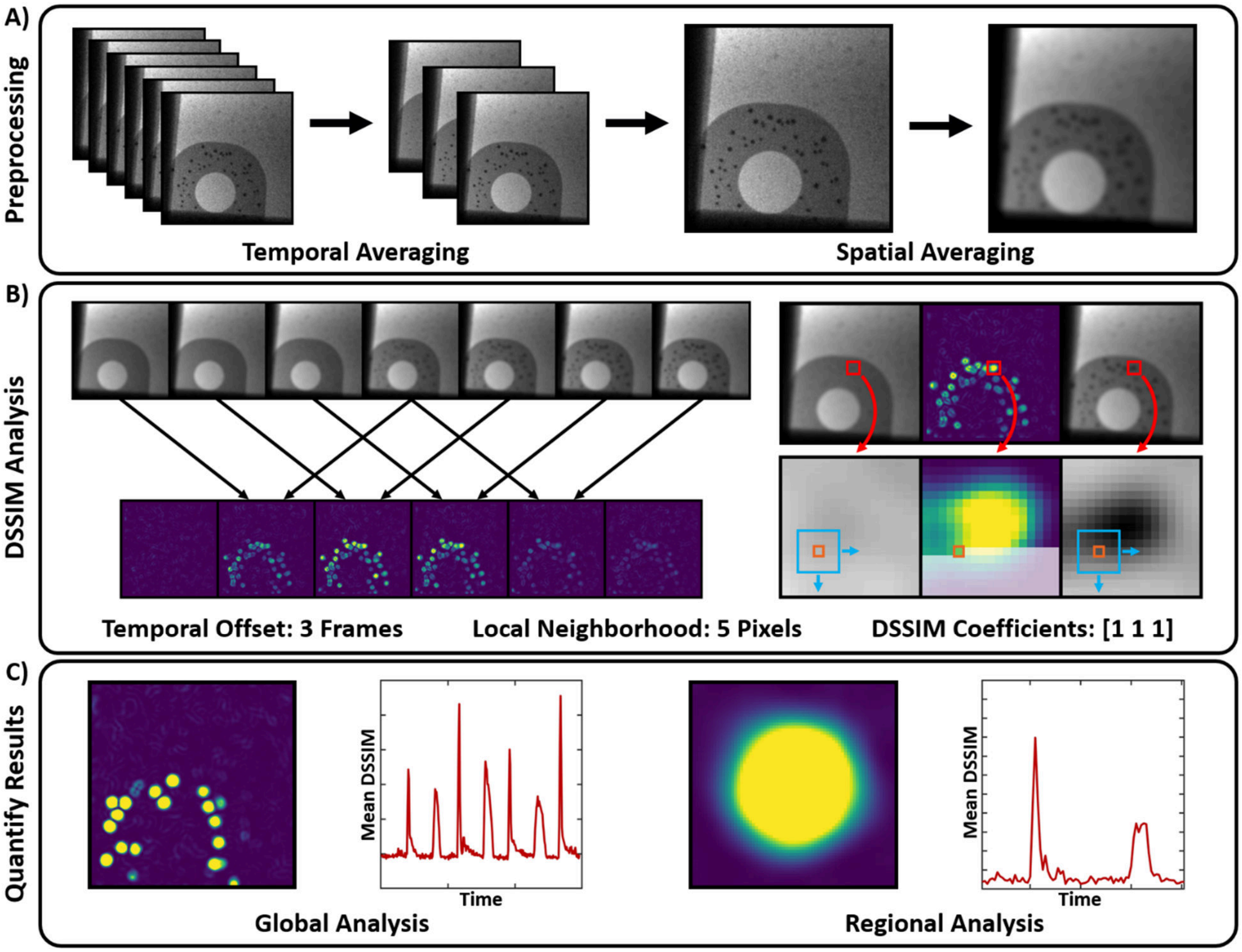

Figure 1.1 DSSIM analysis workflow. (A) Raw data is denoised with a combination of temporal and spatial averaging. (B) DSSIM analysis is applied using the defined parameters. Temporally offset images in the video are compared in a sliding-window operation (left). Image pairs are analyzed with the DSSIM metric which compares the same local neighborhoods of each image to produce a DSSIM image (right). Note images have been downsized by a factor of 4 to improve figure legibility. (C) DSSIM analysis results are quantified with global analysis (entire image) and regional analysis (cropped image).

In step 2, DSSIM analysis is applied to the denoised video. The DSSIM analysis algorithm presented here is a sliding-window calculation which compares frame t with frame t+Δt (Figure 1.1B). First, the two frames are compared with the SSIM metric. For every pixel location in each pair of images (Figure 1.1B, orange boxes), the metric compares intensity values in a Gaussian-weighted local neighborhood around the pixel location (Figure 1.1B, blue boxes). Boarder pixels are excluded from the analysis. The Gaussian-weighted intensity values in the local neighborhoods are compared with three components: the mean (m), variance (v), and cross-correlation (c).[26] Then, these components are weighted by the exponents [$\alpha\ \beta\ \gamma$] and multiplied together to produce a SSIM image (Eq. (1)). The SSIM image is linearly converted to a DSSIM image using Eq. (2). DSSIM values are between 0 and 1, where a high value corresponds to a region of high dissimilarity. The result of the sliding window algorithm is a DSSIM video, which is shorter than the input video by Δt frames.

$$SSIM(t, t + \Delta t) = m(t, t + \Delta t)^{\alpha} * v(t, t + \Delta t)^{\beta} * \ c(t, t + \Delta t)^{\gamma} \tag{1}$$

$$DSSIM(t, t + \Delta t) = \frac{1 - SSIM(t, t + \Delta t)}{2} \tag{2}$$

There are 3 parameters that will affect the output of DSSIM analysis: the local neighborhood size, the temporal offset Δt, and the [$\alpha\ \beta\ \gamma$] DSSIM coefficients. Xt and Xt+Δt denote two local neighborhoods of common size (Figure 1.1B, blue boxes) taken from the same pixel location (Figure 1.1B, orange boxes) in both images. For example, the analysis shown in Figure 1.1B uses 5 × 5 pixel local neighborhoods which are visualized with blue boxes. Every valid pair of neighborhoods is compared with DSSIM to construct the final dissimilarity image, and the size of the local neighborhood will determine the spatial resolution of the output. Δt is the temporal offset of the pair of frames and will determine the temporal resolution of the output. $[\alpha\ \beta\ \gamma]$ are the DSSIM coefficients which adjust the relative weighting of the mean, standard deviation, and cross-correlation components. Coefficients were kept at [1 1 1] for the analyses presented here.

Lastly, the output of DSSIM analysis is quantified (Figure 1.1C). The simplest method of quantification is calculating the global mean DSSIM value for each DSSIM image. This provides information about mean structural change occurring in the image, where high mean DSSIM values correspond to a high degree of structural change. Alternatively, it is often useful to perform regional analysis to compare structural change across different spatial locations in the data,[32] or to closely examine a particular event of interest. After quantification, the original 3-dimensional video is reduced to 1-dimensional data that is easily interpreted and correlated to other types of data.

1.3.2 Parameter tuning

The data analysis pipeline described here requires three parameters to be tuned in Step 2. While multiparameter analysis methods are generally considered to be complex, parameter tuning for DSSIM analysis is intuitive and directly related to the spatial and temporal resolution of the physical phenomena taking place. The spatial and temporal resolution of the detected dynamics will depend on the temporal offset and local neighborhood, respectively. Determining the ideal local neighborhood size requires consideration of the feature size of interest as well as the signal-to-noise ratio. In general, smaller neighborhoods are ideal because they have the highest resolution and are most sensitive to small structural changes, but can result in artifacts and 'false events' caused by noise. If DSSIM analysis is applied to particle nucleation events, the neighborhood should be smaller than the particle (Figure 1.1B). Typically, it is best to start parameter tuning with a large temporal offset and a large neighborhood to capture the most obvious dynamics. These parameters can then be iteratively decreased until the output becomes too noisy for clear interpretation. Depending on the nature of the dynamics, the user should focus on maximizing either temporal or spatial resolution. The structural change must occur over a time period that is strictly larger than twice the time of the temporal offset in order to be captured by DSSIM analysis (Nyquist-Shannon theorem).[34]

The DSSIM coefficients should generally be kept at [1 1 1]. However, it can be useful to remove one of the components of the DSSIM analysis by setting a coefficient to 0. For example, using coefficients [0 0 1] will reduce DSSIM to a local normalized cross-correlation calculation.[35] In the case of confocal fluorescence microscopy data, it was reported that the mean channel contributed mostly noise in the final output, so [0 1 1] coefficients were selected.[32] In the LCTEM datasets presented here, no exponent tuning was required.

Overall, we find parameter tuning to be intuitive and find that the end result is consistent and stable for a wide range of parameters. Additionally, it is important to note that DSSIM analysis is a computationally efficient algorithm that is easily parallelizable. This enables users to receive rapid feedback when tuning DSSIM analysis parameters.

1.3.3 Dataset considerations for DSSIM analysis

The DSSIM metric highlights both structural change and object movement. For datasets where both are occurring at the same time, DSSIM analysis will highlight both types of dynamics.[32] For structures that are in motion, object tracking and drift correction algorithms could be applied in the pre-processing steps to minimize movement from camera drift. This would enable the DSSIM metric to highlight structural changes. In the case of LCTEM electrochemical experiments, structures are typically attached to the electrode or the silicon nitride window, and so structural change can be isolated from object movement. In general, TEM imaging is better suited than scanning transmission electron microscopy (STEM) imaging for DSSIM analysis. This is because TEM images can be captured at higher framerates and there are no scanlines which result in artifacts after applying DSSIM analysis (Figure 1.2C,E). In addition, near-zero pixel intensity values recorded in dark-field STEM imaging can cause instability in the DSSIM metric.

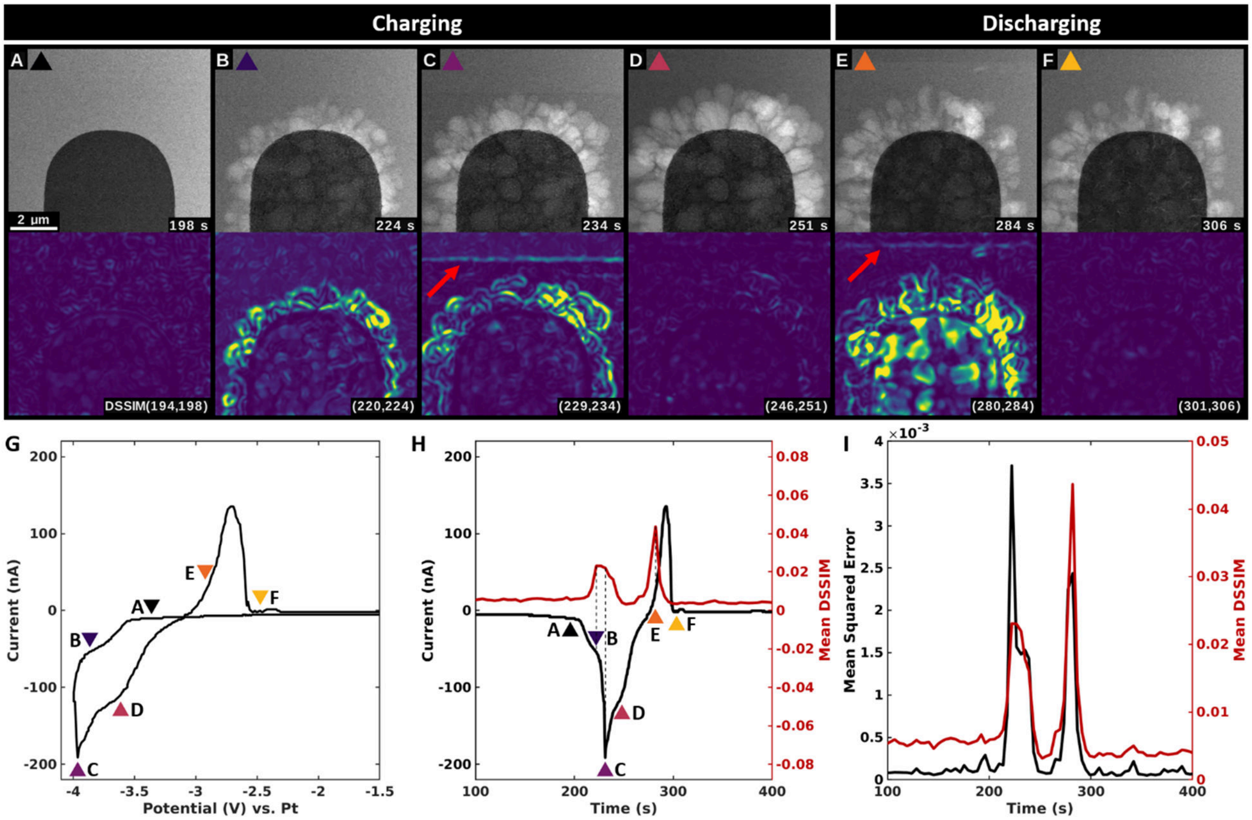

Figure 1.2 DSSIM analysis applied to a previously published bright-field liquid cell STEM video.[6] A-F) Select microscopy frames (top) and corresponding DSSIM frames (bottom) during electrode charging (A-D) and discharging (E,F). Bright pixels values correspond to regions of high dissimilarity between frames. Bottom labels correspond to the times of the two microscopy frames used to calculate the DSSIM image. Red arrows in (C, E) shows STEM scanline artifact in the DSSIM image. G) CV plotted as current vs. potential and H) current vs. time with key frames from (A-F) indicated with triangles. (H) contains a mean DSSIM plot, with key correlative features highlighted with dashed lines. High DSSIM values correspond to timepoints of high change. I) Mean DSSIM and MSE comparison.

1.4 Results and Discussion

1.4.1 DSSIM analysis of bright-field liquid cell STEM

DSSIM analysis is applied to a previously published bright-field liquid cell STEM video of SEI layer formation on a Pt electrode.[6] In this dataset, an electrochemical liquid cell was configured with Pt electrodes on a silicon nitride membrane to create an operando Li battery. Cyclic voltammetry (CV) was performed, in which the electrode potential was progressively decreased to induce charging, then progressively increased to induce discharging. During charging, the SEI layer rapidly grows on the electrode and there is a negative peak in the current (Figure 1.2A-D). During discharging, the SEI layer partially dissolves and there is a positive peak in the current (Figure 1.2E,F).

DSSIM analysis is applied to correlate the features of the recorded CV with the structural changes recorded on the electrode during charging and discharging. The dataset consists of 95 images taken across 402 s with a frame-time of 4.2 s. Preprocessing was done by applying a Gaussian blur with a first standard deviation of 90 nm (7 pixels) to remove noise. Due to the high signal-to-noise ratio and relatively low temporal resolution, no temporal averaging was applied to this dataset. Next, DSSIM analysis was applied with a local neighborhood of 244 × 244 nm (19 × 19 pixels), 1 frame offset, and [1 1 1] coefficients, resulting in 94 DSSIM frames.

The CV is shown as a current-potential plot in Figure 1.2G and replotted as a current-time plot in Figure 1.2H. The mean DSSIM value for each DSSIM frame is plotted to directly compare features of the current-time plot with the structural change taking place in the microscope. The analysis shows a clear correlation between the features of the CV and the resulting structural change. Interesting, there is a 9.0 s delay between the peak current and peak mean DSSIM during charging, and a 10.0 s delay between the negative peak current and peak mean DSSIM during discharging. The current value should be directly proportional to the rate of addition or removal of Li. Considering the frame-time of this dataset is 4.2 s, the mismatch represents 2 frames which could be attributed to a delay in recording the frames. The mismatch could also suggest the addition of Li during the peak current is not contributing to significant structural change of the SEI volume.

To compare the results of DSSIM with another metric, the analysis workflow described in Figure 1.1 was applied but the DSSIM metric was replaced with the mean squared error (MSE) metric. Figure 1.2I shows there is very good agreement between the timescale of features captured with both metrics. Figure 1.2I also shows disagreement in relative peak heights of the two metrics during charging and discharging. This discrepancy is unsurprising, as disagreement between the two metrics has been previously reported.[36-38] MSE compares the absolute error between each pixel for the image pair, whereas DSSIM attempts to evaluate perceived differences in structure by comparing local regions of pixels. As a result, DSSIM is less susceptible to single-pixel noise, which may be the reason for the disagreement in relative peak heights in Figure 1.2I. Another key advantage of DSSIM analysis is the algorithm provides a map of local change for each pair of frames, which is not provided with MSE. This makes it easy to assess which regions of the image are contributing to the mean DSSIM value. Furthermore, the dissimilarity images can aid in qualitative analysis and reveal events easily missed. For example, Figure 1.3 shows there is a subtle structural change that occurs a long time after motion has stopped elsewhere in the SEI layer.

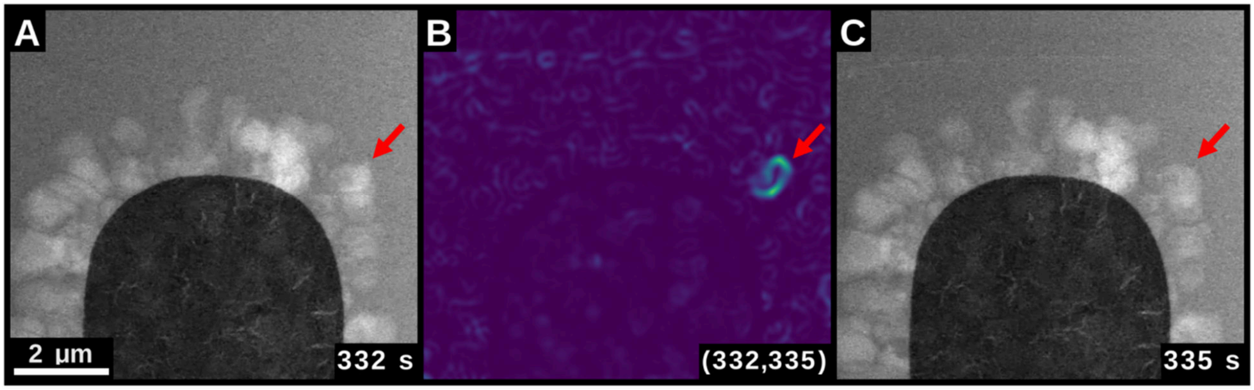

Figure 1.3 (A,C) Consecutive frames in the bright-field liquid cell STEM video with (B) corresponding DSSIM image. Arrow in the DSSIM image highlights an isolated structural change event.

1.4.2 DSSIM analysis of bright-field LCTEM

DSSIM analysis was applied to a bright-field LCTEM dataset which captures cyclic electrochemical Cu plating and stripping on a TiNx electrode. An in-depth description of the electrode fabrication and experimental details will be released in an upcoming manuscript.[39] In this experiment, square-wave chronoamperometry was performed in which the electrode potential was decreased to −1.5 V (vs. TiNx) and held constant to induce Cu plating, then instantaneously increased to +1.5 V (vs. TiNx) and held constant to induce Cu stripping. Figure 1.4A-D shows the first plating process as the dark Cu domains form on the electrode. Figure 1.4E,F shows the first stripping process as the domains dissolve. In total, 4 plating and 3 stripping processes were performed.

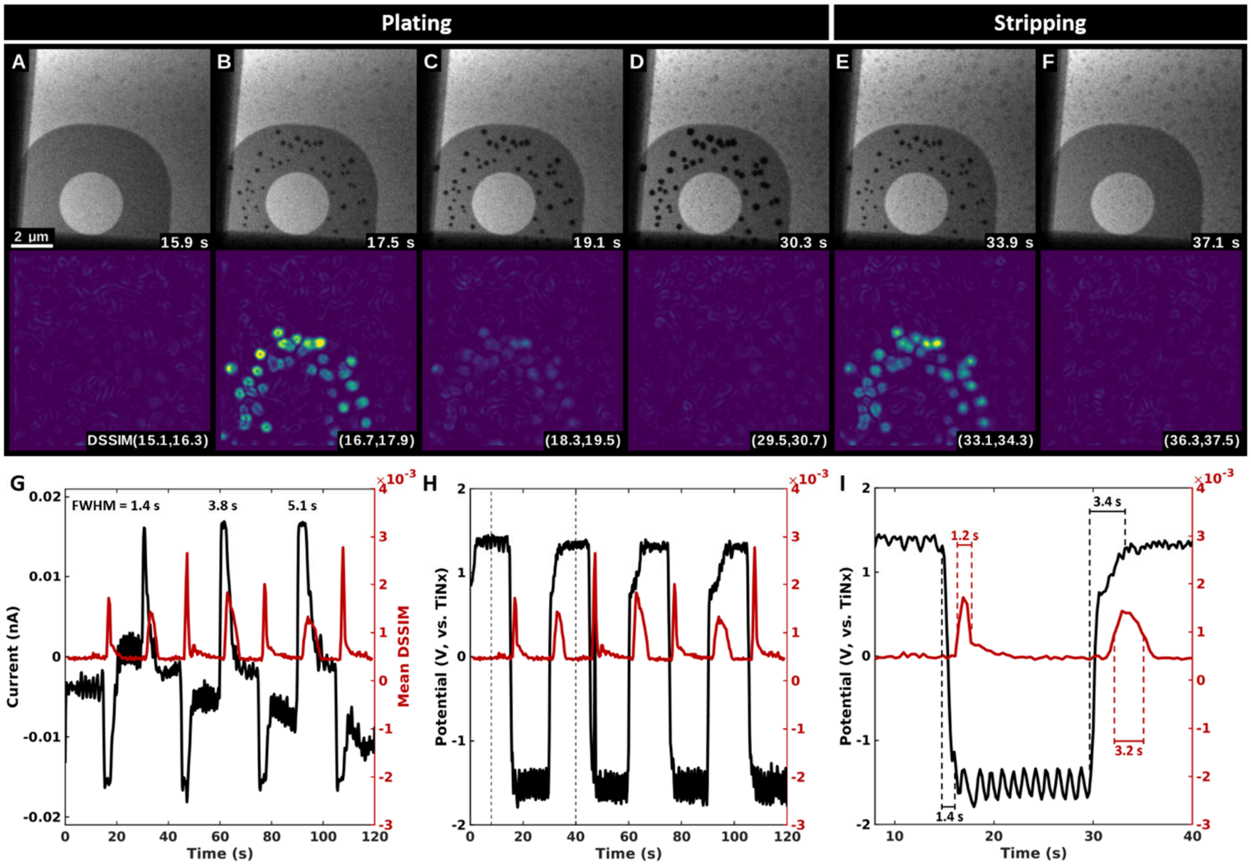

Figure 1.4 DSSIM analysis applied to bright-field LCTEM data.[39] A-F) Select microscopy frames (top) and corresponding DSSIM frames (bottom) during electrode plating (A-D) and stripping (E,F). Bright pixels values correspond to regions of high dissimilarity between frames. Bottom labels correspond to the times of the two microscopy frames used to calculate the DSSIM image. (G) Square-wave chronoamperometry plotted as current vs. time and (H) potential vs. time compared to mean DSSIM. High DSSIM values correspond to timepoints of high change. Current and potential data was smoothed using a Gaussian-weighted sliding-window average with a stand deviation of 1.5 datapoints. (I) Zoom-in to dashed region in H. Black dashed lines mark timescale of features in the potential plot. Red dashed lines mark the timescale of the DSSIM peaks using FWHM.

DSSIM analysis is applied to correlate the features of the square wave chronoamperometry data with the structural changes occurring on the electrode during plating and stripping. The raw dataset consists of 600 images taken across 120 s with a frame-time of 0.2 s. Preprocessing was done by first temporal averaging every 2 frames, reducing the size of the dataset to 300 frames. Next, a Gaussian blur was applied with a standard deviation of 120 nm (10 pixels) to remove noise. Then, DSSIM analysis was applied with a local neighborhood of 131 × 131 nm (11 × 11 pixels), 1.8 s offset (3 frames), and [1 1 1] coefficients. A frame offset of 3 was selected due to the high temporal resolution of the initial dataset, which meant there was little measurable change between adjacent frames. These parameters resulted in 297 DSSIM frames.

The mean DSSIM is calculated for each frame and then plotted against the current-time data (Figure 1.4G) and the potential-time data (Figure 1.4H). The mean DSSIM plot shows that during plating, there is a sharp peak in Cu structural formations which subsequently slows down. During stripping, there is more uniform structural dissolution that occurs at a slower rate. This signature pattern is observed during each of the plating/stripping cycles captured in this dataset. Interestingly, during stripping the DSSIM peaks show broadening across each subsequent cycle. This peak broadening is also seen via full-width half-max (FWHM) analysis of the stripping peaks in the current-time plot (Figure 1.4G). These features in the chronoamperometry and mean DSSIM data suggest there is hysteresis across the stripping cycles. To further examine this, all DSSIM images were averaged together to display the entire history of structural change in a single image (Figure 1.5). Figure 1.5 shows there were regions that experienced multiple nucleation events (red arrows). This suggests there are some locations that favor Cu nucleation, or the Cu does not fully dissolve during stripping.

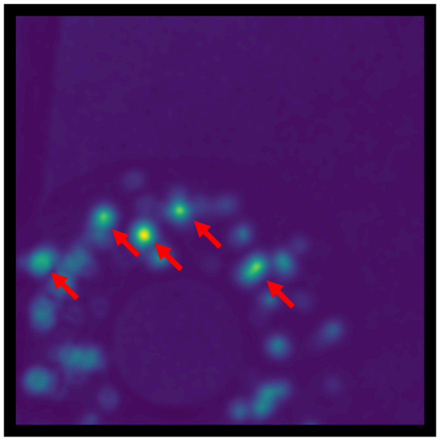

Figure 1.5 Summation of all DSSIM frames from the bright-field LCTEM dataset. Arrows highlight regions where multiple nucleation events occurred on the electrode.

Closer examination of the potential-time and mean DSSIM plots from the first cycle shows there is a strong correlation between the shape of the square-wave chronoamperometry and the structural change events occurring on the electrode (Figure 1.4I). During plating, the potential-time plot shows a delay of 1.4 s before −1.5 V is reached. Applying FWHM analysis to the mean DSSIM peak shows that structural formation occurs across 1.2 s. During stripping, a similar phenomenon occurs in which there is a delay of 3.4 s before the voltage reaches +1.5 V. FWHM analysis of the mean DSSIM peak shows that structural dissolution occurs across 3.2 s. This analysis demonstrates the timescale of features in the square-wave chronoamperometry correlate with the timescale of structural change events occurring on the electrode.

1.4.3 Comparison of DSSIM analysis and segmentation analysis

Regional DSSIM analysis was applied to individual Cu plating and stripping events from the previously discussed bright-field LCTEM dataset (Section 3.2) to compare the results of DSSIM analysis to the results of segmentation-based growth rate analysis. Typically, particle growth rate is calculated by segmenting the particle in each frame and then calculating the derivative of area with respect to time.[40] Here, we compare growth rates calculated from segmentation analysis to the structural change calculated from regional DSSIM analysis.

Individual particle plating and stripping events from video 2 were isolated and cropped for analysis (Figure 1.6). For each frame, the particle area was calculated using a standard segmentation routine that has been described previously.[40] The green outline labels the edge of the segmented particle in each frame (Figure 1.6A,D). Next, the particle growth rate was calculated by first smoothing the particle areas (Figure 1.6B,E) and then taking the derivative of smoothed area with respect to time (Figure 1.6C,F). The growth rate plots show a sharp increase in size during plating followed by a decrease in size during striping.

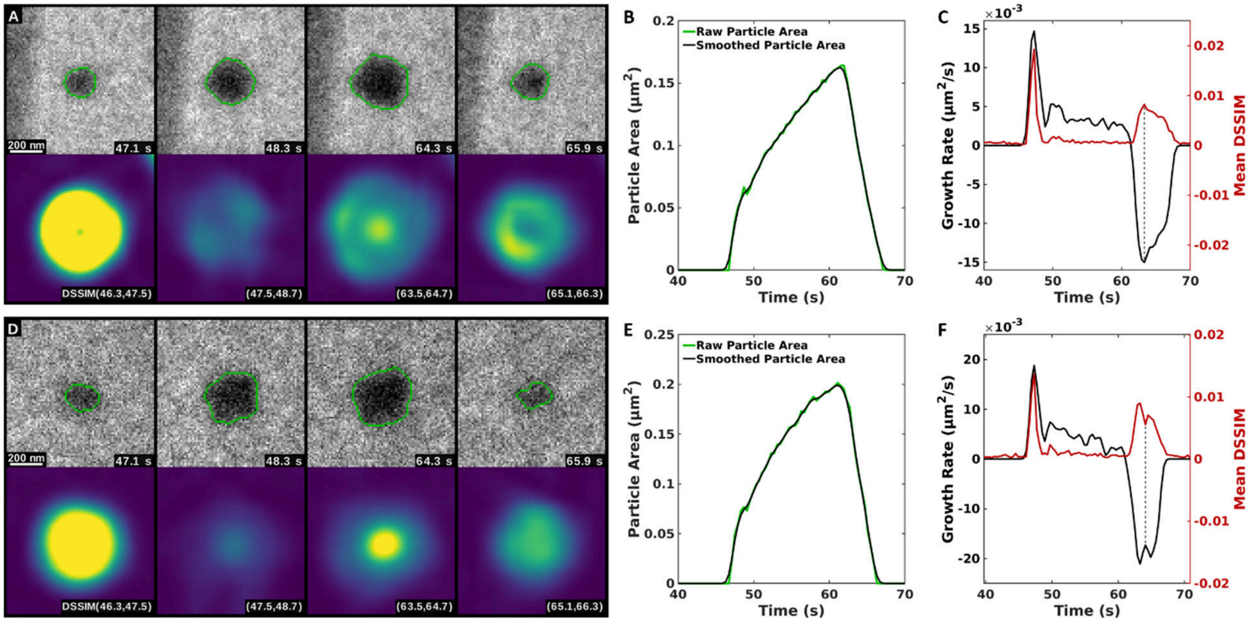

Figure 1.6 Regional DSSIM analysis compared to segmentation-based growth-rate analysis. (A,D) Select microscopy frames showing segmentation of particle (top) and corresponding DSSIM frames (bottom) during electrode plating and stripping. Bright pixels values correspond to regions of high dissimilarity between frames. Bottom labels correspond to the times of the two microscopy frames used to calculate the DSSIM image. (B,E) Segmented particle areas for each frame plotted over time. Black line indicates a sliding-window Gaussian-weighted average. (C,F) Growth rate calculated as the derivative of the smoothed particle area with respect to time and mean DSSIM from regional analysis. Dashed lines show key features are aligned.

The same region was then cropped from the corresponding DSSIM frames and the mean DSSIM values were calculated. Figure 1.6C,F shows the same features are captured in particle growth rate analysis and the regional mean DSSIM analysis. Figure 1.6F shows DSSIM analysis correctly captures the subtle decrease in growth rate (dashed line). This demonstrates DSSIM can be used as an alternative to segmentation analysis in cases where the temporal scale and rate of structural change are of interest. It is important to highlight that DSSIM analysis provides different information than segmentation analysis. Specifically, DSSIM analysis will capture changes in object contrast, which are not directly captured in segmentation analysis. Additionally, DSSIM analysis will only provide relative information about how a structure is changing whereas segmentation analysis provides an absolute value about the particle size and position. For example, Figure 1.6C,F shows the particle size is increasing steadily between 50 s and 60 s. While this slow growth is still visible in the DSSIM(47.5,48.7) images, the mean DSSIM graph does not highlight this processes. Note that increasing the temporal-offset of DSSIM analysis would improve the signal of the slow growth at the cost of temporal resolution. While particle segmentation is straightforward in the case presented here, DSSIM analysis can be applied to datasets in which segmentation is highly subjective or impossible, such as multiclass datasets where objects have a wide distribution of intensities.[23,32]

1.5 Code availability and efficiency

ImageJ, MATLAB, and Python code for applying DSSIM analysis is available via Github: github.com/JustinTMulvey/DSSIM_Analysis. DSSIM analysis is accessible as a MATLAB script, Python Jupyter notebook, or ImageJ plugin with an accompanying user-guide. The ImageJ plugin has an easy-to-use user-interface and can process floating-point and integer-type microscopy datasets (Figure 1.7). The MATLAB and Python codes are parallelized and can process floating point videos data at 100–1000 MB/s (depending on neighborhood size) on a modern high-end CPU (32 cores 3.5 GHz, 3200 MHz memory).

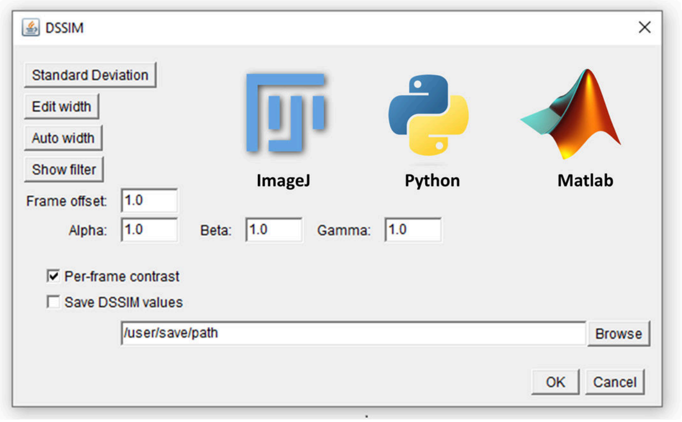

Frame offset: 1.0

Alpha: 1.0 Beta: 1.0 Gamma: 1.0

☑ Per-frame contrast

☐ Save DSSIM values

/user/save/path

Figure 1.7 ImageJ user interface for applying DSSIM analysis. DSSIM analysis can also be applied using Python or MATLAB scripts.

1.6 Data acquisition

The bright-field liquid cell STEM video of SEI layer formation on a Pt electrode was acquired by downloading the SI video from the publication.[6] The CV data was extracted and aligned to frames using a custom computer vision script. Frame times and CV times were estimated by matching the extracted frames to the publication figure time stamps and then using linear interpolation. The bright-field LCTEM dataset of Cu plating and stripping on a TiNx electrode and accompanying square wave chronoamperometry data was received as raw data.[39]

1.7 Conclusion

We have demonstrated DSSIM analysis can be used to detect and quantify structural change in LCTEM videos. We showed the method can be used to assist in qualitative analysis and reveal structural change that is easily missed when viewing the raw data. We also showed the algorithm can be used to quantitatively correlate the applied electrochemical biasing to the structural change that occurs on the electrode. We verified the accuracy of the metric by comparing it to segmentation analysis and found good agreement in temporal scale and magnitude of individual particle growth rates. Given the computation efficiency and ease of interpretation, we believe there is great potential to use DSSIM analysis for real-time event detection during data acquisition to highlight changes taking place to the microscope operator. This use case may also extend as an automated event detection algorithm for application in sparse imaging.

1.8 References

(1) De Jonge, N.; Ross, F. M. Electron Microscopy of Specimens in Liquid. *Nature Nanotechnology* **2011**, *6* (11), 695–704. https://doi.org/10.1038/nnano.2011.161.

(2) Ross, F. M. Opportunities and Challenges in Liquid Cell Electron Microscopy. *Science* **2015**, *350* (6267), aaa9886. https://doi.org/10.1126/science.aaa9886.

(3) Mirsaidov, U.; Patterson, J. P.; Zheng, H. Liquid Phase Transmission Electron Microscopy for Imaging of Nanoscale Processes in Solution. *MRS Bulletin* **2020**, *45* (9), 704–712. https://doi.org/10.1557/mrs.2020.222.

(4) Sung, J.; Bae, Y.; Park, H.; Kang, S.; Choi, B. K.; Kim, J.; Park, J. Liquid-Phase Transmission Electron Microscopy for Reliable In Situ Imaging of Nanomaterials. *Annu. Rev. Chem. Biomol. Eng.* **2022**, *13* (1), 167–191. https://doi.org/10.1146/annurev-chembioeng-092120-034534.

(5) Abellan, P.; Woehl, T. J. Liquid Cell Electron Microscopy for the Study of Growth Dynamics of Nanomaterials and Structure of Soft Matter. In *In-situ Characterization Techniques for Nanomaterials*; Kumar, C. S. S. R., Ed.; Springer Berlin Heidelberg: Berlin, Heidelberg, 2018; pp 1–31. https://doi.org/10.1007/978-3-662-56322-9_1.

(6) Mehdi, B. L.; Qian, J.; Nasybulin, E.; Park, C.; Welch, D. A.; Faller, R.; Mehta, H.; Henderson, W. A.; Xu, W.; Wang, C. M.; Evans, J. E.; Liu, J.; Zhang, J.-G.; Mueller, K. T.; Browning, N. D. Observation and Quantification of Nanoscale Processes in Lithium Batteries by Operando Electrochemical (S)TEM. *Nano Lett.* **2015**, *15* (3), 2168–2173. https://doi.org/10.1021/acs.nanolett.5b00175.

(7) Lee, S.-Y.; Shangguan, J.; Alvarado, J.; Betzler, S.; Harris, S. J.; Doeff, M. M.; Zheng, H. Unveiling the Mechanisms of Lithium Dendrite Suppression by Cationic Polymer Film Induced Solid–Electrolyte Interphase Modification. *Energy Environ. Sci.* **2020**, *13* (6), 1832–1842. https://doi.org/10.1039/D0EE00518E.

(8) Mehdi, B. L.; Stevens, A.; Qian, J.; Park, C.; Xu, W.; Henderson, W. A.; Zhang, J.-G.; Mueller, K. T.; Browning, N. D. The Impact of Li Grain Size on Coulombic Efficiency in Li Batteries. *Sci Rep* **2016**, *6* (1), 34267. https://doi.org/10.1038/srep34267.

(9) Leenheer, A. J.; Jungjohann, K. L.; Zavadil, K. R.; Sullivan, J. P.; Harris, C. T. Lithium Electrodeposition Dynamics in Aprotic Electrolyte Observed *in Situ via* Transmission Electron Microscopy. *ACS Nano* **2015**, *9* (4), 4379–4389. https://doi.org/10.1021/acsnano.5b00876.

(10) Yang, Y.; Xiong, Y.; Zeng, R.; Lu, X.; Krumov, M.; Huang, X.; Xu, W.; Wang, H.; DiSalvo, F. J.; Brock, Joel. D.; Muller, D. A.; Abruña, H. D. *Operando* Methods in Electrocatalysis. *ACS Catal.* **2021**, *11* (3), 1136–1178. https://doi.org/10.1021/acscatal.0c04789.

(11) Hwang, S.; Chen, X.; Zhou, G.; Su, D. In Situ Transmission Electron Microscopy on Energy-Related Catalysis. *Adv. Energy Mater.* **2020**, *10* (11), 1902105. https://doi.org/10.1002/aenm.201902105.

(12) Pan, Y.; Li, X.; Su, D. Understanding the Structural Dynamics of Electrocatalysts via Liquid Cell Transmission Electron Microscopy. *Current Opinion in Electrochemistry* **2022**, *33*, 100936. https://doi.org/10.1016/j.coelec.2022.100936.

(13) Yang, Y.; Louisia, S.; Yu, S.; Jin, J.; Roh, I.; Chen, C.; Fonseca Guzman, M. V.; Feijóo, J.; Chen, P.-C.; Wang, H.; Pollock, C. J.; Huang, X.; Shao, Y.-T.; Wang, C.; Muller, D. A.; Abruña, H. D.; Yang, P. Operando Studies Reveal Active Cu Nanograins for CO2 Electroreduction. *Nature* **2023**, *614* (7947), 262–269. https://doi.org/10.1038/s41586-022-05540-0.

(14) Liu, J.; Wei, B.; Sloppy, J. D.; Ouyang, L.; Ni, C.; Martin, D. C. Direct Imaging of the Electrochemical Deposition of Poly(3,4-Ethylenedioxythiophene) by Transmission Electron Microscopy. *ACS Macro Lett.* **2015**, *4* (9), 897–900. https://doi.org/10.1021/acsmacrolett.5b00479.

(15) Subramanian, V.; Martin, D. C. In Situ Observations of Nanofibril Nucleation and Growth during the Electrochemical Polymerization of Poly(3,4-Ethylenedioxythiophene) Using Liquid-Phase Transmission Electron Microscopy. *Nano Lett.* **2021**, *21* (21), 9077–9084. https://doi.org/10.1021/acs.nanolett.1c02762.

(16) de Jonge, N.; Houben, L.; Dunin-Borkowski, R. E.; Ross, F. M. Resolution and Aberration Correction in Liquid Cell Transmission Electron Microscopy. *Nature Reviews Materials* **2019**, *4* (1), 61–78. https://doi.org/10.1038/s41578-018-0071-2.

(17) Spurgeon, S. R. Towards Data-Driven next-Generation Transmission Electron Microscopy. *Nature Materials* 6.

(18) Rizvi, A.; Mulvey, J. T.; Carpenter, B. P.; Talosig, R.; Patterson, J. P. A Close Look at Molecular Self-Assembly with the Transmission Electron Microscope. *Chem. Rev.* **2021**, acs.chemrev.1c00189. https://doi.org/10.1021/acs.chemrev.1c00189.

(19) Parent, L. R.; Bakalis, E.; Ramírez-Hernández, A.; Kammeyer, J. K.; Park, C.; de Pablo, J.; Zerbetto, F.; Patterson, J. P.; Gianneschi, N. C. Directly Observing Micelle Fusion and Growth in Solution by Liquid-Cell Transmission Electron Microscopy. *J. Am. Chem. Soc.* **2017**, *139* (47), 17140–17151. https://doi.org/10.1021/jacs.7b09060.

(20) Yan, C.; Byrne, D.; Ondry, J. C.; Kahnt, A.; Moreno-Hernandez, I. A.; Kamat, G. A.; Liu, Z.-J.; Laube, C.; Crook, M. F.; Zhang, Y.; Ercius, P.; Alivisatos, A. P. Facet-Selective Etching Trajectories of Individual Semiconductor Nanocrystals. *Sci. Adv.* **2022**, *8* (32), eabq1700. https://doi.org/10.1126/sciadv.abq1700.

(21) Yao, L.; Ou, Z.; Luo, B.; Xu, C.; Chen, Q. Machine Learning to Reveal Nanoparticle Dynamics from Liquid-Phase TEM Videos. *ACS Cent. Sci.* **2020**, *6* (8), 1421–1430. https://doi.org/10.1021/acscentsci.0c00430.

(22) Reehl, S.; Stanfill, B.; Johnson, M.; Ries, D.; Browning, N. D.; Layla Mehdi, B.; Bramer, L. Event Detection for Undersampled Electron Microscopy Experiments: A Control Chart Case Study. *Quality Engineering* **2020**, *32* (2), 244–254. https://doi.org/10.1080/08982112.2019.1638515.

(23) Leijten, Z. J. W. A.; Keizer, A. D. A.; de With, G.; Friedrich, H. Quantitative Analysis of Electron Beam Damage in Organic Thin Films. *J. Phys. Chem. C* **2017**, *121* (19), 10552–10561. https://doi.org/10.1021/acs.jpcc.7b01749.

(24) Loza, A.; Mihaylova, L.; Canagarajah, N.; Bull, D. Structural Similarity-Based Object Tracking in Video Sequences. In *2006 9th International Conference on Information Fusion*; IEEE: Florence, 2006; pp 1–6. https://doi.org/10.1109/ICIF.2006.301574.

(25) Wang, Z.; Bovik, A. C.; Sheikh, H. R.; Simoncelli, E. P. Image Quality Assessment: From Error Visibility to Structural Similarity. *IEEE Transactions on Image Processing* **2004**, *13* (4), 600–612. https://doi.org/10.1109/tip.2003.819861.

(26) Rouse, D. M.; Hemami, S. S. Understanding and Simplifying the Structural Similarity Metric. In *2008 15th IEEE International Conference on Image Processing*; IEEE: San Diego, CA, USA, 2008; pp 1188–1191. https://doi.org/10.1109/ICIP.2008.4711973.

(27) Wu, Y.; Rivenson, Y.; Wang, H.; Luo, Y.; Ben-David, E.; Bentolila, L. A.; Pritz, C.; Ozcan, A. Three-Dimensional Virtual Refocusing of Fluorescence Microscopy Images Using Deep Learning. *Nat Methods* **2019**, *16* (12), 1323–1331. https://doi.org/10.1038/s41592-019-0622-5.

(28) Puthongkham, P.; Rocha, J.; Borgus, J. R.; Ganesana, M.; Wang, Y.; Chang, Y.; Gahlmann, A.; Venton, B. J. Structural Similarity Image Analysis for Detection of Adenosine and Dopamine in Fast-Scan Cyclic Voltammetry Color Plots. *Analytical Chemistry* **2020**, *92* (15), 10485–10494. https://doi.org/10.1021/acs.analchem.0c01214.

(29) Touil, A.; Kalti, K.; Conze, P.-H.; Solaiman, B.; Mahjoub, M. A. Automatic Detection of Microcalcification Based on Morphological Operations and Structural Similarity Indices. *Biocybernetics and Biomedical Engineering* **2020**, *40* (3), 1155–1173. https://doi.org/10.1016/j.bbe.2020.05.002.

(30) Ushizima, D.; Perciano, T.; Parkinson, D. Fast Detection of Material Deformation through Structural Dissimilarity; IEEE, 2015. https://doi.org/10.1109/bigdata.2015.7364080.

(31) Madhav, B. T. P.; Venu Gopala Rao, M.; Pisipati, V. G. K. M. Identification of Liquid Crystalline Phases in 7O.O9 Compound Based on Structural Similarity Index Measure. *Liquid Crystals* **2015**, *42* (2), 198–203. https://doi.org/10.1080/02678292.2014.975290.

(32) Selmani, S.; Schwartz, E.; Mulvey, J. T.; Wei, H.; Grosvirt-Dramen, A.; Gibson, W.; Hochbaum, A. I.; Patterson, J. P.; Ragan, R.; Guan, Z. Electrically Fueled Active Supramolecular Materials. *J. Am. Chem. Soc.* **2022**, jacs.2c01884. https://doi.org/10.1021/jacs.2c01884.

(33) Bultema, L. A.; Bücker, R.; Schulz, E. C.; Tellkamp, F.; Gonschior, J.; Miller, R. J. D.; Kassier, G. H. The Effect of Secondary Electrons on Radiolysis as Observed by in Liquid TEM: The Role of Window Material and Electrical Bias. *Ultramicroscopy* **2022**, *240*, 113579. https://doi.org/10.1016/j.ultramic.2022.113579.

(34) Shannon, C. E. Communication in the Presence of Noise. *Proc. IRE* **1949**, *37* (1), 10–21. https://doi.org/10.1109/JRPROC.1949.232969.

(35) Prieto, G.; Guibelalde, E.; Chevalier, M.; Turrero, A. Use of the Cross-Correlation Component of the Multiscale Structural Similarity Metric (R* Metric) for the Evaluation of Medical Images: R* Metric for

the Evaluation of Medical Images. *Med. Phys.* **2011**, *38* (8), 4512–4517. https://doi.org/10.1118/1.3605634.

(36) Ederer, M.; Löffler, S. Image Difference Metrics for High-Resolution Electron Microscopy. *Ultramicroscopy* **2022**, *240*, 113578. https://doi.org/10.1016/j.ultramic.2022.113578.

(37) Nilsson, J.; Akenine-Möller, T. Understanding SSIM. arXiv June 29, 2020. http://arxiv.org/abs/2006.13846 (accessed 2023-04-24).

(38) Zhou Wang; Bovik, A. C. Mean Squared Error: Love It or Leave It? A New Look at Signal Fidelity Measures. *IEEE Signal Process. Mag.* **2009**, *26* (1), 98–117. https://doi.org/10.1109/MSP.2008.930649.

(39) Park, J.; Cheng, N.; Pivak, Y.; Sun, H.; Pérez Garza, H. H.; Ge, B.; Basak, S.; Eichel, R.-A. Metal Plating and Stripping on a Titanium Nitride Microelectrode: An Electrochemical Transmission Electron Microscopy Study.

(40) Rizvi, A.; Mulvey, J. T.; Patterson, J. P. Observation of Liquid–Liquid-Phase Separation and Vesicle Spreading during Supported Bilayer Formation via Liquid-Phase Transmission Electron Microscopy. *Nano Lett.* **2021**, *21* (24), 10325–10332. https://doi.org/10.1021/acs.nanolett.1c03556.

CHAPTER 2: Applying DSSIM analysis to quantify electrically-fueled dissipative self-assembly processes captured with liquid cell electron microscopy and confocal fluorescence microscopy

Portions of this chapter were adapted from a published article (WS Gibson, JT Mulvey, S Das, S Selmani, JG Merham, AM Rakowski, E Schwartz, AI Hochbaum, Z Guan, JR Green, JP Patterson. “Observing the dynamics of an electrochemically driven active material with liquid electron microscopy” ACS Nano. 2024, 18 (18), 11898–11909). © 2024 American Chemical Society

Portions of this chapter were adapted from a published article (S Selmani, E Schwartz, JT Mulvey, H Wei, A Grosvirt-Dramen, W Gibson, AI Hochbaum, JP Patterson, R Ragan, Z Guan. “Electrically Fueled Active Supramolecular Materials” J. Am. Chem. Soc. 2022, 15 (3), 1106–1116). © 2022 American Chemical Society

2.1 Abstract

Living organisms such as actin filaments and microtubules form complex, dynamic structures through fuel-driven dissipative self-assembly processes. This enables novel functions such as motility, homeostasis, self-healing, and camouflage which are difficult to reproduce synthetically. Designing a synthetic dissipative self-assembly system with spatial and temporal control of the self-assembly process may enable the development of materials with these properties. Here, I describe two studies in which an electrode is used to supply local fuel to synthetic dissipative self-assembly systems. In each study, I use DSSIM analysis as a metric to spatially and temporally quantify the local assembly process. I show DSSIM analysis performs better than segmentation analysis for studying these systems as there is often a large gradient of intensity values in the images which constantly fluctuate due to the competing assembly and disassembly processes. In the first example, I use DSSIM analysis to capture and quantify the propagation of a wave-like self-assembly process recorded using liquid cell transmission electron microscopy (LCTEM). In the second example, I spatially resolve a fiber gel formation process on an electrode recorded using confocal laser scanning microscopy (CLSM). These examples demonstrate the advantages of DSSIM analysis as a segmentation-free method of quantifying dissipative self-assembly processes. Furthermore, these examples demonstrate the versatility of DSSIM analysis, as the technique can be applied effectively to both LCTEM and CLSM.

2.2 Introduction

Dissipative self-assembly is defined as a thermodynamically out-of-equilibrium process in which fuel is consumed to sustain higher order structures such as fibers.[1] A key feature of dissipative self-assembly is the presence of two competing reactions: a forward reaction which activates precursors into a product capable of self-assembly, and a backward reaction which reduces the product back into the precursor state.[2] Here, I present research on an electrically fueled synthetic dissipative reaction network that reversibly converts cysteine derivative (CSH) into it cystine derivative (CSSC) which is capable of self-assembling into fibers.[3] Simultaneously, the chemical reductant dithiothreitol (DTT) acts to reduce the system back to the CSH monomer (Figure 2.1). The goal of these studies is to track the dynamic behavior of the self-assembled structures and establish a spatial and temporal control of the system properties.

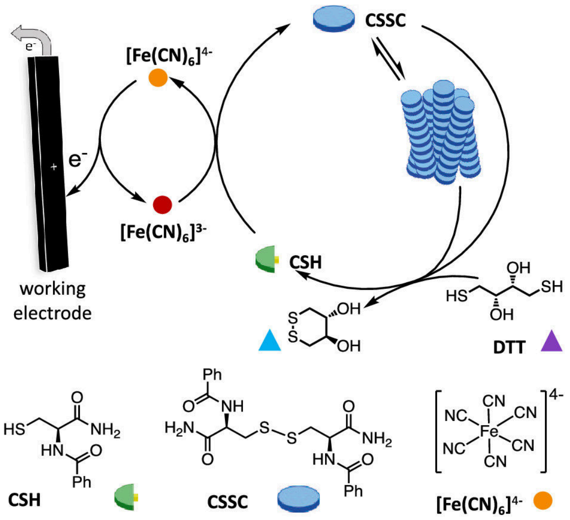

Figure 2.1 Schematic representation of the CSH/CSSC electrically-fueled dissipative self-assembly process.

Due to the competing chemical reactions, the self-assembled structures are highly dynamic and therefore difficult to study. In situ microscopy techniques are ideal for directly imaging the dissipative self-assembly processes in solution, with the goal of capturing and quantifying the material dynamics. In the text below, I will present my analyses of two in situ datasets capturing the electrically fueled self-assembly of the CSH/CSSC system. The first dataset I will present is a LCTEM video collected by Wyeth Gibson. As described in Chapter 1, LCTEM is a technique used to image samples directly in solution using a closed-system silicon nitride cell.[4,5] Specialized in situ LCTEM holders can capture a sample's response to a variety of external stimuli such as changes in solvent composition, temperature, or electrical bias.[6,7] In this dataset, the electrically fueled self-assembly of the CSH/CSSC system is captured with nanoscale spatial resolution and millisecond-scale temporal resolution (Figure 2.6). The second dataset I will present is a confocal laser scanning microscopy (CLSM) video collected by Serxho Selmani. CLSM is an optical microscopy technique in which contrast is generated by the fluorescence response of a material as a laser scans point-by-point across the imaging area. In this dataset, Nile red is added into the CSH mixture to track the formation of the structures. The micron-scale video shows a CSSC gel forming on an electrode (Figure 2.13). For a complete description of the material system and microscopy methodology for the LCTEM[8] and CLSM[9] datasets, the reader is directed to the respective manuscripts. The information presented here will focus primarily on the image analysis methods applied to the datasets.

In both cases, the raw microscopy data is difficult to interpret. In the case of LCTEM, the data had to be collected at a very low electron dose rate in order to minimize the effect of the electron beam on the dissipative process. This resulted in a dataset with a large amount of noise. The structures are clearly visible in the raw data, but the dataset required extensive processing to maximize insight into the self-assembly process. The second dataset was collected using CLSM. While the individual nano-fibers structures are too small to be captured with optical microscopy, the micron-scale fiber macrostructures are visible with CSLM due to intercalation of Nile red. This dataset is challenging to analyze for several reasons: (1) the slow scan rate of CSLM resulted in 1 frame every ~4 seconds so frame averaging to reduce noise was not possible (2) fibers were constantly forming resulting in strong contrast gradients which made individual fiber segmentation highly subjective or impossible (3) fibers were constantly moving in and out of the focal plan which further contributed to the contrast gradient found in this dataset. In the sections that follow, I describe methodology for applying DSSIM analysis[10] to the LCTEM and CLSM datasets and discuss the key outcomes from the analyses.

2.3 Liquid Cell Transmission Electron Microscopy (LCTEM)

2.3.1 LCTEM: Methods and Results

Image processing and analysis was applied to the LCTEM video to quantify the dissipative behavior of the material. This section will first describe the preprocessing pipeline and segmentation algorithm applied to both movies. Subsequent sections will describe the details and parameters of how the preprocessing pipeline and segmentation algorithm were applied to each movie. A final section will describe more details on DSSIM analysis.

2.3.1.1 Preprocessing algorithm

Both movies were preprocessed using a previously reported methodology (Figure 2.2)[11–13]. The raw LCTEM frames were loaded into Matlab from Digital Micrograph 4 files, which preserves pixel intensity values at double-precision floating point values. Due to the low dose rates and short exposure times, the raw frames contained extremely low signal-to-noise ratios, so extensive preprocessing was required prior to analysis. First, frames were spatially reduced to 1024 x 1024 using pixel averaging (Figure 2.2a). Next, frames were temporally averaged using a sliding window average. Different temporal averaging was applied to each dataset, so the exact details will be described in the relevant sections. Next, the images were flattened using sequential Gaussian filters to isolate the fiber foci by removing the high-frequency noise and low-frequency background (Figure 2.2b). First, the low-frequency background image was estimated by applying a Gaussian blur with a relatively large standard deviation to the averaged image. Additionally, the high-frequency noise was removed by applying a Gaussian blur with a relatively small standard deviation to the averaged image. The output image was then divided by the previously calculated background image, which results in a flattened image. The filtering was done sequentially to optimize the removal of low-frequency and high-frequency noise (details below). Ultimately, the goal was to use filtering to isolate objects with diameters in the size range of ~60 nm to ~400 nm (Gaussian blur first standard deviations of ~20 nm to

~130 nm to account for 3 standard deviations of the Gaussian blur). All subsequent analysis, including segmentation analysis and DSSIM analysis, was applied to the flattened images. The electrode was masked off using the same mask for every frame, which was determined by an intensity threshold.

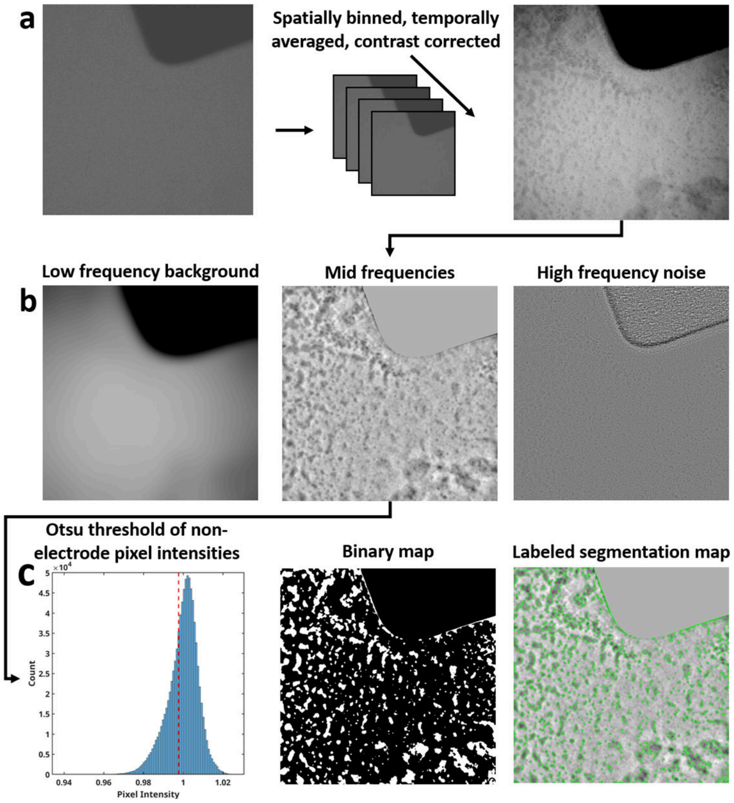

Figure 2.2 Image pre-processing and segmentation pipeline. a) Images were spatially binned with pixel averaging, temporally binned with frame averaging, and contrast corrected by removing outlier pixels when displaying the image. Outliers were only removed when displaying the image and remain in the image in subsequent steps. b) A Gaussian FFT band-pass filter was applied to isolate the mid frequencies of the FFT which correspond to the sample. C) The average Otsu threshold of non-electrode pixels was calculated and applied to every image to produce a segmentation map.

2.3.1.2 Segmentation algorithm

Next, an intensity threshold was calculated to segment the sample from the background (Figure 2.2c). Because of the image flattening, it was possible to use a single threshold to accurately segment the entire image. For each flattened image, the non-electrode pixels were isolated, and the segmentation threshold was calculated using the Otsu threshold algorithm.[14] Then, the average Otsu threshold for all images was calculated. This average threshold was applied to segment every image, which ensures a consistent definition of which intensities correspond to sample and which correspond to background. Finally, the flattened image was labeled by converting the outline of each object in the segmentation map into a green outline, which was overlaid onto the flattened image.

Image preprocessing and segmentation analysis were applied to the LCTEM video. First, the 6114 raw Digital Micrograph 4 images were imported into Matlab as double-precision floating point values. Pixel averaging was applied to convert the images from 4096 x 4096 resolution to 1024 x 1024 resolution. Next a sliding window average of 270 frames (27 seconds) was applied, which resulted in 5,845 frames. This set was then subsampled every 30 frames to improve computational efficiency, resulting in 194 images where each image contains 27 seconds of information (Figure 2.3a). Next, a Gaussian blur with a standard deviation of 10 pixels (30.5 nm) was applied to remove high frequency noise. The background image was calculated by applying a Gaussian blur with a standard deviation of 50 pixels (152.5 nm). The flattened image was then calculated by dividing the denoised image by the background image (Figure 2.3b). Finally, the Otsu threshold segmentation routine described in "Segmentation algorithm" was applied (Figure 2.3c,d).

Next, regional segmentation analysis was performed. The region maps were generated by taking the distance transform of the binary electrode mask, and then thresholding that image at each of the 4 distance bands. The same methodology was applied for generating the vertical masks, except the distance map was generated from a column of white pixels at the left edge of the image rather than the electrode. For each binary segmentation map, each band mask image was individually multiplied by the segmentation map to isolate the band of interest (Figure 2.4a , Figure 2.5a). Statistics were recorded on the isolated particles. These statistics were then plotted for each band (Figure 2.4b,c , Figure 2.5b,c).

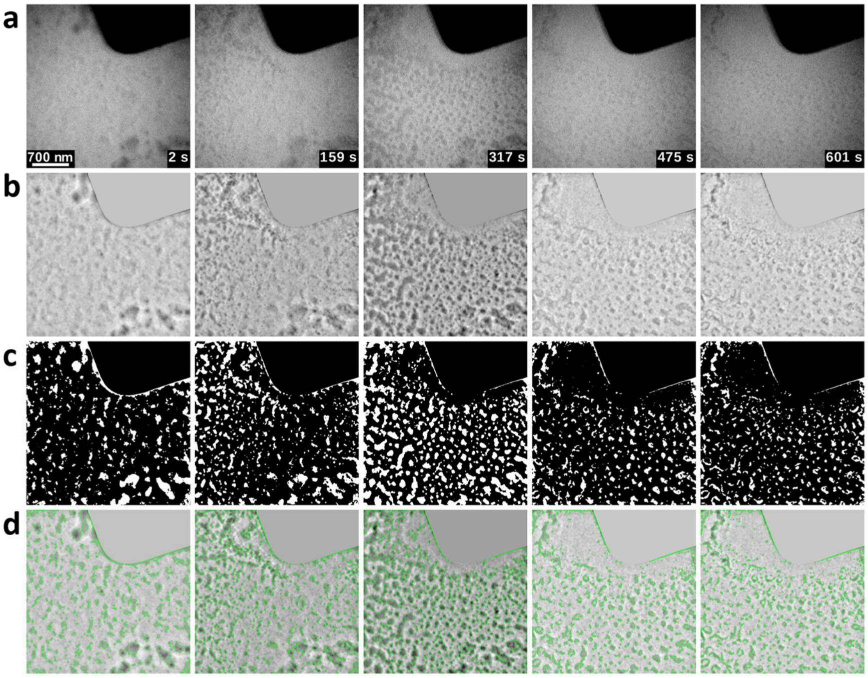

Figure 2.3 Segmentation analysis of the LCTEM video. a) Spatially and temporally binned LCTEM images. b) Flattened LCTEM images. c) Binary images showing locations of segmented particles from b). d) Flattened LCTEM images with segmented structures outlined in green.

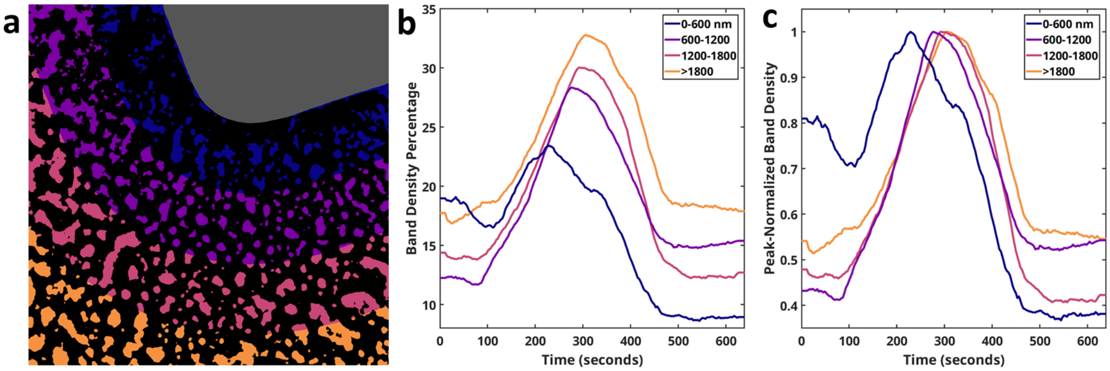

Figure 2.4 Regional segmentation analysis of the LCTEM video. a) Segmentation map divided into 4 colored regions based on distance from the electrode. Each region is 600 nm thick. B) Structure density within each region plotted over time. Density is calculated by the number of segmented pixels divided by the total pixels of the distance band. C) Band density plot normalized to the peak value. The bands reach their peak density sequentially, starting at the closest band and then moving outward.

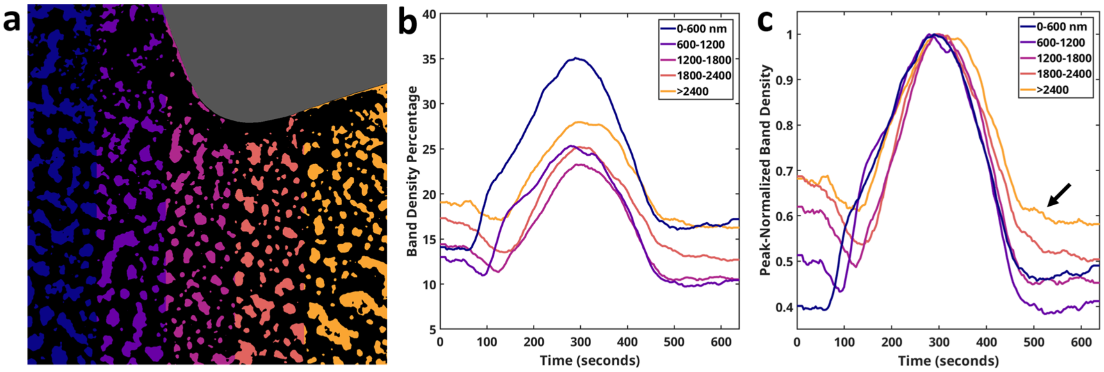

Figure 2.5 Regional segmentation analysis of the LCTEM video. a) Segmentation map divided into 5 vertical regions based on distance from the left side of the image, denoted by color. Each region is 600 nm thick. B) Structure density within each region plotted over time. Density is calculated by the number of segmented pixels divided by the total pixels of the vertical band. C) Band density plot normalized to the peak value. Arrow highlights time points where there is a subtle increase in segmented area in the first right region of the viewing area where all other regions are decreasing.

2.3.1.3 DSSIM analysis

DSSIM analysis was applied to the flattened (described above) images of the LCTEM video. The details of the analysis are described discussion section. Figure 2.6 shows a comparison of the binned data (Figure 2.6a), flattened data (Figure 2.6b), and dissimilarity images (Figure 2.6c). Note the time reported in Figure 2.6a is approximately the average time of the two frames used to generate the dissimilarity image. Qualitative examination shows the structural change reported in the DSSIM images is well matched to the structural changes occurring in the binned images and flattened images.

Figure 2.7 shows the results of analyzing the output of DSSIM analysis using vertical bands in order to resolve front 1. The distance bands were generated using the same methodology described in the previous section, but 400 nm bands were used for the distances bands and the bands overlap (band 1: 0-400 nm, band 2: 80-480 nm, band 3: 160-560 nm, ect). Figure 2.10 is the summation of all dissimilarity frames, which represents a single history map of where structural change has occurred in the viewing area.

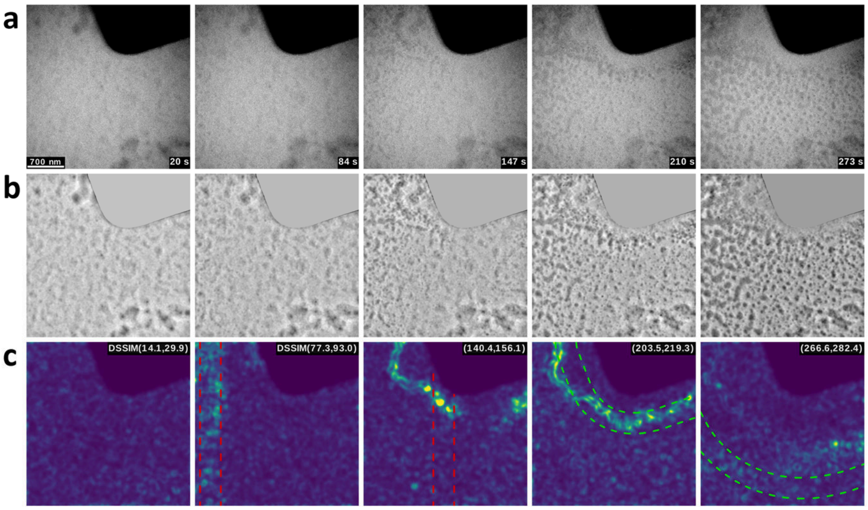

Figure 2.6 Comparison of processed, flattened, and DSSIM LCTEM images. a) Spatially and temporally binned LCTEM images. b) Flattened LCTEM images. c) Dissimilarity images from DSSIM analysis. Bright pixel values correspond to regions of high dissimilarity between frames. Top time labels correspond to the times (seconds) of the two LCTEM images used to calculate the DSSIM image.

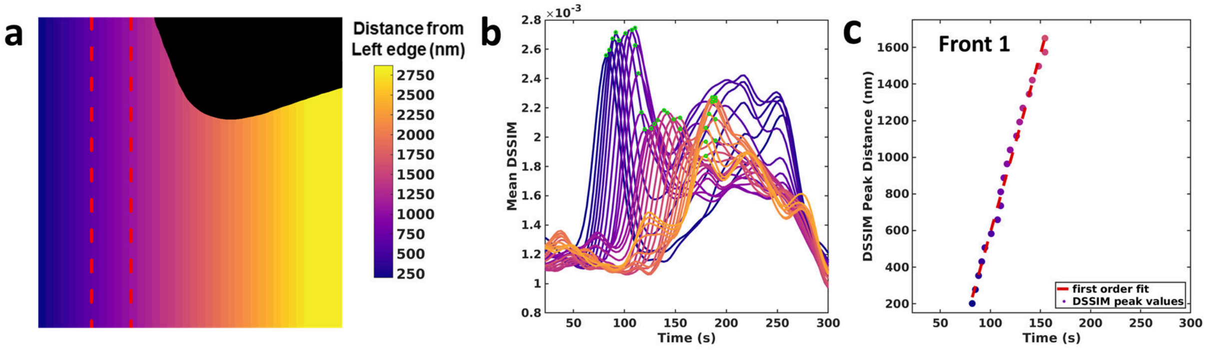

Figure 2.7 Visualization and quantification of fiber foci dynamics. a) The image was divided into 36 overlapping vertical regions, each 400 nm thick, based on distance from left edge of the image. The dashed line shows the size of 1 region. The color gradient shows distance from the left side of the image for each of the 36 regions, with purple being closest and yellow the furthest. Some of the far-right regions were omitted for visual clarity. b) Shows the mean DSSIM signal of each region versus time. The green dots mark the maximum for each region. c) Shows the progression of the global regional DSSIM maximums for front 1. Front 1 shows a linear velocity.

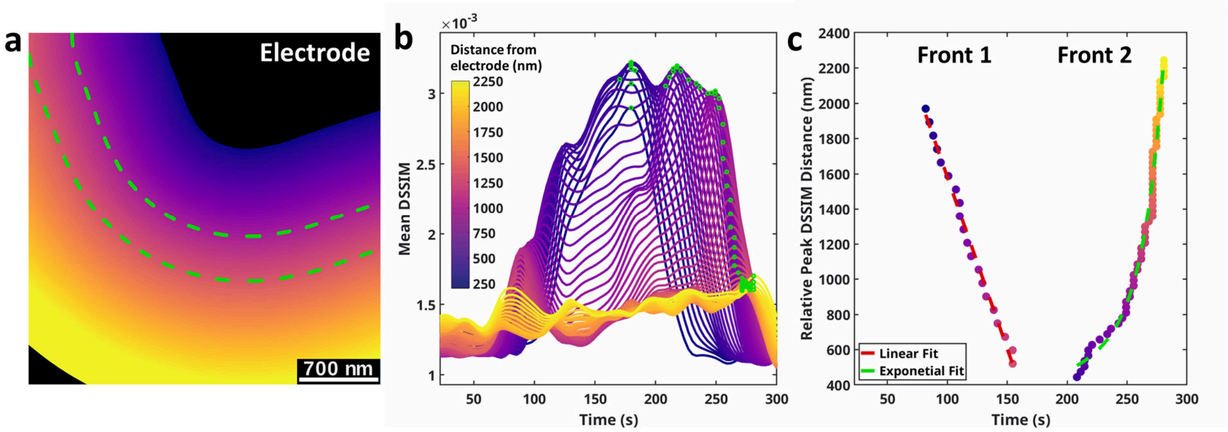

Figure 2.8 Visualization and quantification of fiber foci dynamics. (a) Image was divided into 70 overlapping regions, each 400 nm thick, based on distance from the electrode. The dashed line shows the size of 1 region. The color gradient shows the distance from the electrode for each of the 70 regions, with purple being closest to the electrode and yellow the furthest. (b) Mean DSSIM signal of each region versus time. The green dots mark the maximum dissimilarity for each region. (c) Progression of the regional DSSIM maximums for both front 1 (Figure 2.7) and front 2. Front 1 shows a linear velocity while front 2 is accelerating.

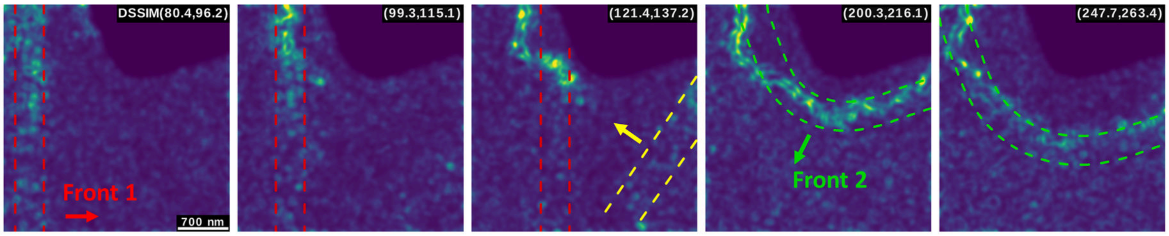

Figure 2.9 Dissimilarity images from DSSIM analysis with all assembly front labeled. Bright pixel values correspond to regions of high dissimilarity between frames. Top time labels correspond to the times (seconds) of the two Liquid EM images used to calculate the DSSIM image.

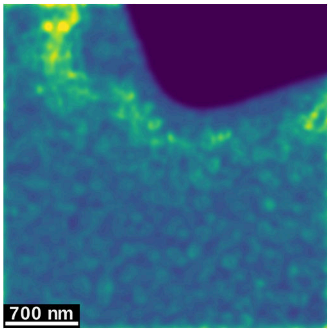

Figure 2.10 Summation of all DSSIM images. This shows the entire history of change within the viewing area and shows that the greatest amount of change occurs within ~1000 nm of the electrode.

2.3.2 LCTEM: Discussion

To quantify the observed wave-like propagation of these self-assembly fronts, regional segmentation analysis was performed (Figure 2.4, Figure 2.5). Figure 2.4a and Figure 2.5a show the flattened TEM images, and Figure 2.4b and Figure 2.5b show the corresponding structure segmentation maps. To resolve the spatiotemporal behavior of the fronts, regional density analysis was performed on the segmentation maps. To resolve front 2, the segmentation maps were split into four different 600 nm thick regions based on distance from the electrode. For each frame, the object density in each region was calculated and then normalized to the respective maximum density. This enabled a direct comparison of the times at which the structures reached the maximum size in each region. Figure 2.4c shows that maximum structural density occurs sequentially based on the distance from the electrode, which confirms the qualitative observation of the outward-moving front 2. Interestingly, there appears to be a large time delay between the 0–600 region and subsequent regions, implying that front 2 may be accelerating and moving more quickly through regions that are further from the electrode. Regional analysis was also applied to resolve front 1 in which the regions were defined vertically based on distance from the left edge of the image (Figure 2.5). Again, the analysis clearly resolves the self-assembly growth front as it moves across each region.

To quantify the characteristics of fronts 1 and 2, regional analysis was performed on the DSSIM data (Figure 2.7, Figure 2.8). The image was divided into several 400 nm thick regions based on distance from the electrode. In this case, 36 overlapping vertical regions (Figure 2.7a) and 70 overlapping distance regions (Figure 7b) were defined, which provided a higher spatial resolution while maintaining an adequate sample size within each region. To resolve the magnitude of the structural change spatially and temporally, the mean DSSIM value was calculated for each region in every frame (Figure 2.8b). Figures 2.8b and Figure 2.10 show structural dynamics are greatest in the regions <1000 nm from the electrode and then substantially decrease in the regions >1000 nm from the electrode, consistent with previous confocal laser scanning microscopy data on this chemical system. (14) This observation suggests that there is a spatial dependence with respect to the electrode on the interaction between the electrochemically generated oxidant and the CSH reductant. Next, the velocities of front 1 and front 2 were quantified by finding the time at which the maximum DSSIM value occurs for each region (Figure 2.7b, Figure 2.8b, green dots). This represents the time at which the structural change is at a maximum within each region. Plotting the maximum time against the average region distance results in a distance–time graph. Fitting front 1 with a line shows the front is moving at constant velocity. Fitting front 2 with an exponential fit shows the front is positively accelerating and confirms the observation made from the segmentation analysis. This behavior implies the material formed during front 1 is acting as an autocatalyst, and increasing the speed of the assembly seen in front 2.

2.4 Confocal Laser Scanning Microscopy (CLSM)

2.4.1 CLSM: Methods and Results

Data analysis on the CLSM video was completed using in-house MATLAB scripts. The analysis can be divided into the following steps: 1) image filtering and normalization, 2) structural dissimilarity (DSSIM) analysis, and 3) DSSIM region analysis.

2.4.1.1 Preprocessing algorithm

Images for the CLSM video were collected, as described above, as 12-bit images. Each image was 1024 x 248 pixels, with a pixel size of 0.13 µm and a dwell time of 3.15 µs, resulting in a frame time of 3.759 s per image. For simplicity, 962 x 248 pixels of the original image are used in the analysis, resulting in an image which is 125.0 µm x 32.2 µm. Time = 0 for the movie is defined as the end of the collection of the first image.

Several standard image processing techniques were applied to the images before analysis. First, a gamma correction with an exponent of 0.45 was applied (Eq 1). This was done to better represent the small fibers which have poor brightness when viewed on a linear scale. Next, a Gaussian blur was applied with first standard deviation of 3 pixels which resulted in a kernel size of 13 x 13 pixels (1.69 µm x 1.69 µm) (Eq 2). Gaussian kernels were normalized such that the sum of all values is equal to 1. This standard deviation was chosen to remove Gaussian noise without substantially altering the fiber features in the image. Next, outliers were removed from the movie to improve contrast in the images for qualitative assessment. The images were combined into a single volume, with frame time as the third dimension, then the top 1 percentile ($i_{.01}$) and the 99. percentile ($i_{.99}$) values were calculated. Every value below $i_{.01}$ was replaced with $i_{.01}$, and every value above $i_{.99}$ was replaced with $i_{.99}$ (Eq 3). These outlier percentiles were chosen to provide adequate contrast for viewing the data. The resulting contrast corrected volume was converted to a grayscale volume with normalized intensities between 0 and 1 (Eq 4) and then displayed as a cyan shaded image. Note contrast was assigned for the entire volume, not per individual image. A visual summary of the processing pipeline can be seen in Figure 2.11. The resulting normalized CLSM images are used in Figure 2.11-2.14 and for clear visualization and qualitative assessment. The same pipeline was used to prepare the CLSM images for qualitative analysis. However, outlier percentile values 0.1 and 99.9 were chosen in Eq 3 to minimize unnecessary processing of the data. Normalized CLSM images from this pipeline were used to calculate all DSSIM images (discussed below) and quantitative analysis in Figure 2.12-2.14.

$$I_g = {I_r}^{\gamma} \qquad \text{Eq 1}$$

$$I_g\text{: } Gamma\ corrected\ image$$

$$I_r\text{: } Raw\ image$$

$$\gamma\text{: } Gamma\ correction\ exponent$$

$$I_s = matrix\ convolution(I_g, k_{gauss})$$ Eq 2

$$I_s\text{: } Guassian\ smoothed\ image$$

$$k_{gauss}\text{: } 2D\ normalized\ Gaussian\ kernel$$

$$I_c(x,y) = \begin{cases} i_{.99}, & I_s(x,y) > i_{.99} \\ I_s(x,y), & i_{.99} \geq I_s(x,y) \geq i_{.01} \\ i_{.01}, & I_s(x,y) < i_{.01} \end{cases}$$ Eq 3

$$I_c\text{: } Contrast\ corrected\ image$$

$$i_{.99}\text{: } 99\ percentile\ intensity\ value\ of\ I_b\ movie\ volume$$

$$i_{.01}\text{: } 1\ percentile\ intensity\ value\ of\ I_b\ movie\ volume$$

$$x, y\text{: } pixel\ position\ in\ image$$

$$I_n(x,y) = \frac{I_c(x,y) - min\ (V_c)}{max\ (V_c - min(V_c))}$$ Eq 4

$$I_n\text{: } Normalized\ image$$

$$V_c\text{: } volume\ of\ all\ contrast\ corrected\ images$$

$$x, y\text{: } pixel\ position\ in\ image$$

$$min(\,)\text{: } minimum\ value$$

$$max(\,)\text{: } maximum\ value$$

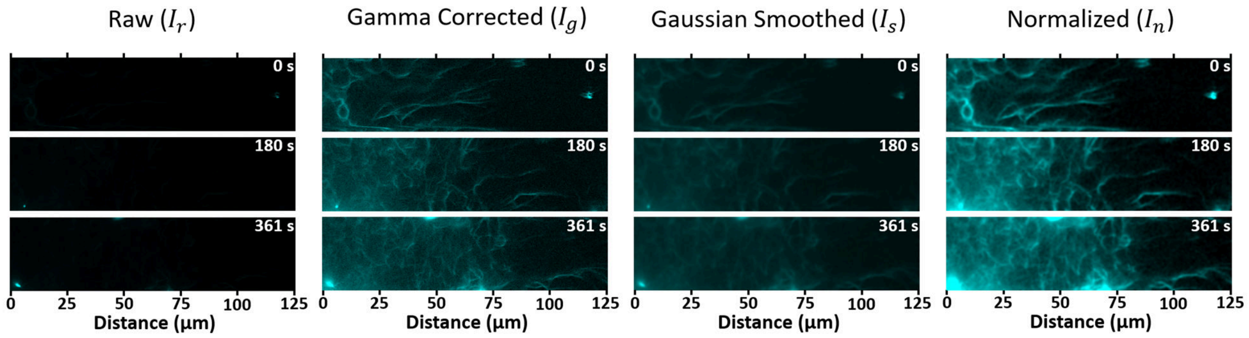

Figure 2.11 Image filtering and normalization steps of select images, calculated from Eq 1-4.

2.4.1.2 DSSIM analysis

The goal of the analysis was to quantify fiber dynamics during dissipative self-assembly. Specifically, to quantify the fast dynamics occurring at the fiber-solution interfaces, and the slow dynamics occurring in the bulk of the fiber gel which can be seen visually in the CLSM video. Here, [a,b,c] = [0,1,1] was applied. This was done to avoid artifacts in the dark regions of the image which were unstable and susceptible to noise. $[c_1, c_2, c_3] = [.0001, .0009, .00045]$ which are MATLAB default values for grayscale images. The Gaussian-weighted neighborhood was formed with a standard deviation of 3 pixels, which resulted in a 19 x 19 pixel (2.47 x 2.47 µm) neighborhood.

As discussed previously, the DSSIM image contains values between 1 and 0, where 1 represents a perfect dissimilarity and 0 represents a perfect similarity; the higher the DSSIM value, the more dissimilar the local neighborhoods of the images are, which represents regions of high dynamics. Comparison of the two images used to create the DSSIM image with the DSSIM image (Figure 2.12) show that regions of high fiber intensity in the CLSM image do not necessarily correspond to regions of high dynamics and that the fibers are most dynamic at the fiber-water interface.

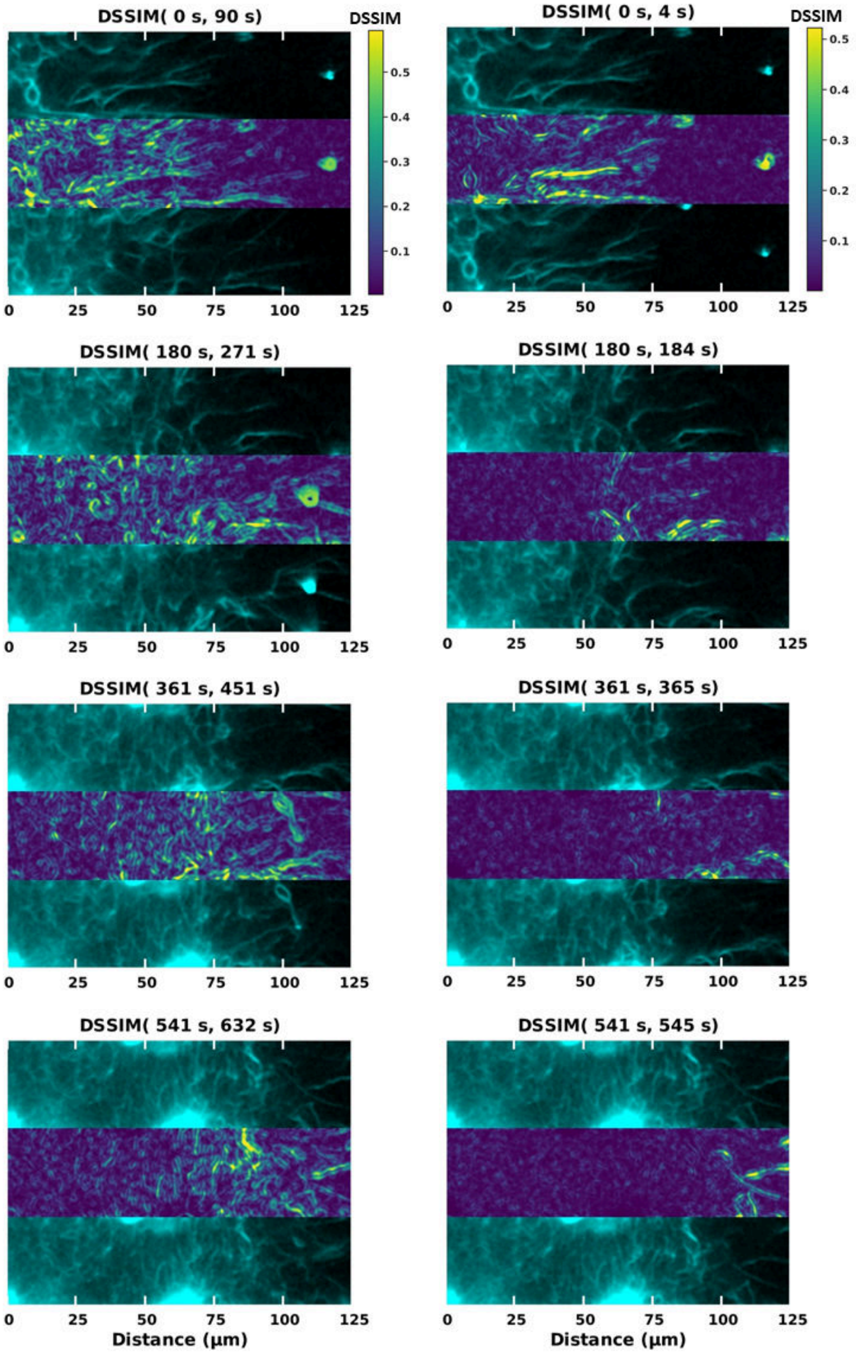

Figure 2.12 Each panel shows CLSM image (t) on the top and (t + Δt) on the bottom, with resulting DSSIM(t ,t + Δt) image between. Left column, 90 s temporal offset. Right column, 3.75 s offset.

Each DSSIM image was divided into 5 equal sections at 25 µm intervals from the left edge of the image. The mean DSSIM of each region was calculated for each set of images (t ,t + Δt). This makes it possible to track the dynamic motion as a function of distance from the electrode surface over the course of the movie. Note from Eq 5 that each image and therefore each feature is present in two calculations: first as (t + Δt), and then again Δt later as (t). This can result in periodic oscillation in the DSSIM average plot, as a bright, fast moving object passes through a region at (t + Δt), and then again at (t) as seen in Figure 2.13f region 75 - 100 µm. This is most significant at high temporal offsets and fast-moving objects. Additionally, if there is a bright, fast moving object it will be counted “twice”, clearly seen in the CLSM video. Here, the same CLSM feature produces two bright feature DSSIM image. However, this still signifies high dynamics in the region which is the intended outcome of this analysis.

The normalized CLSM images processed with Eqs 1-4 were also divided into 5 sections, and the mean normalized intensity of each section was plotted for the entire movie (Figure 2.14a,c). This analysis shows a temporal offset in the intensity increase of each region as the gel forms, which is the expected result. However, intensity analysis alone is highly susceptible to bright objects, seen in region 50 – 75 µm of S10b, and is unable accurately quantify the dynamics occurring in the dim region 100 – 125 µm relative to other regions. Figure 2.14 also shows that fiber dynamics do not necessarily correspond with an increase in intensity. In Figure 2.14c, region 50 – 75 µm is increasing in average intensity between 360 s and 540 s, while the DSSIM analysis in both Figure 2.13f and S10d show a decrease in dynamics in this region during the same timeframe. DSSIM analysis can also be tuned to analyze both fast and slow dynamics by tuning the temporal offset, demonstrated here by the different features captures in the plots produces in Figure 2.13f with a 90 s offset and Figure 2.14d with a 3.75 s offset. These examples highlight the strength of the multicomponent DSSIM analysis for quantifying complex dynamics.

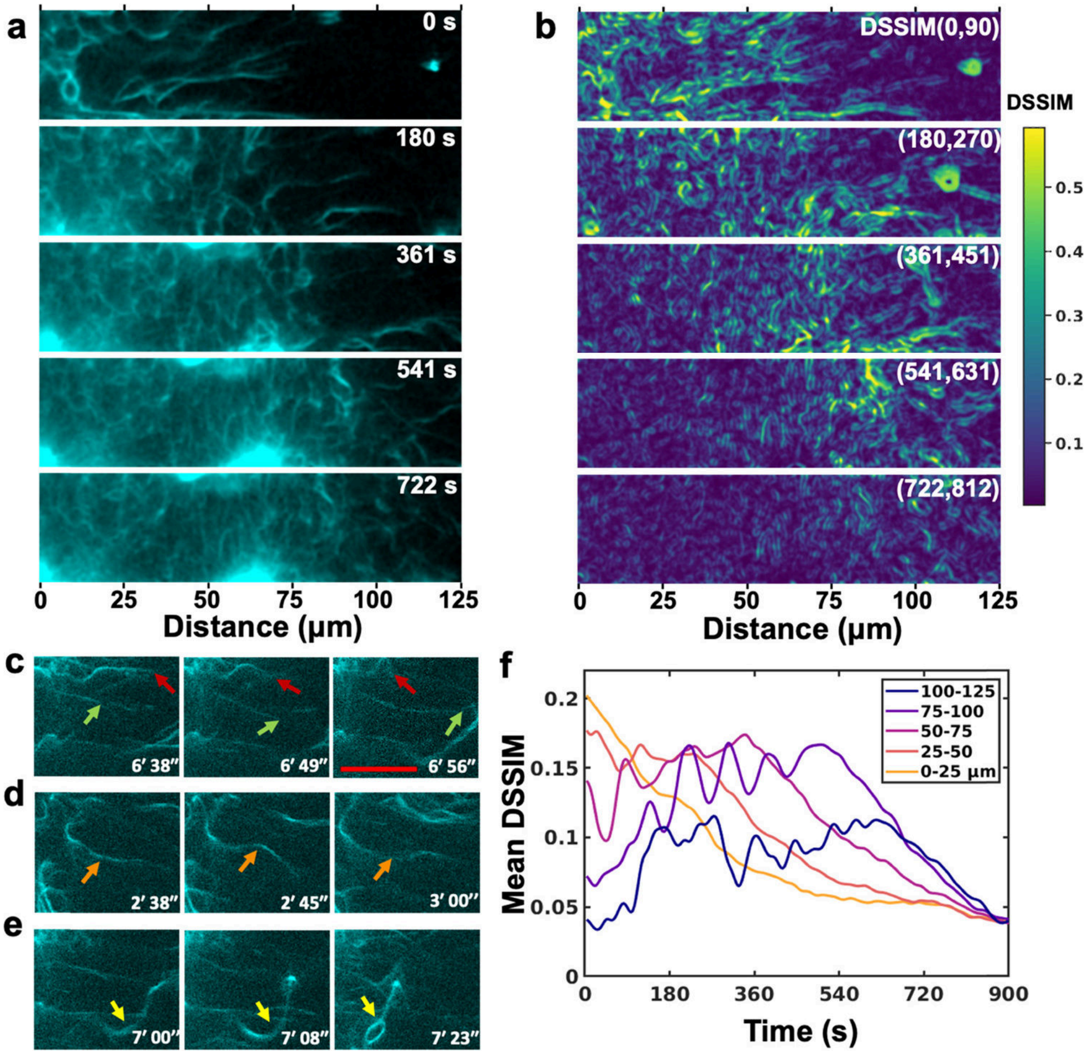

Figure 2.13 Active dynamic self-assembly fueled by electricity. (a) Processed CLSM snapshots highlighting the high dynamics for self-assembly at the gel front (details in Supporting Information). (b) Structural dissimilarity frame series generated by calculating the DSSIM of CLSM frames taken 90 s apart. Bright pixels represent regions of high structural dissimilarity between local areas in frames of comparison, which corresponds to fiber dynamics. (c–e) Snapshots showing different active fiber movements: simultaneous fiber growth and shrinkage ((c) green arrow for growing fiber and red for shrinking), waving (d), and curling/looping (e) (CLSM images rendered with γ = 0.45 and 150% hue saturation for fiber visualization). (f) Mean DSSIM in each region seen in (b). (The working electrode for (a–e) is out of frame on the left. Scale bar = 20 μm for (c–e).

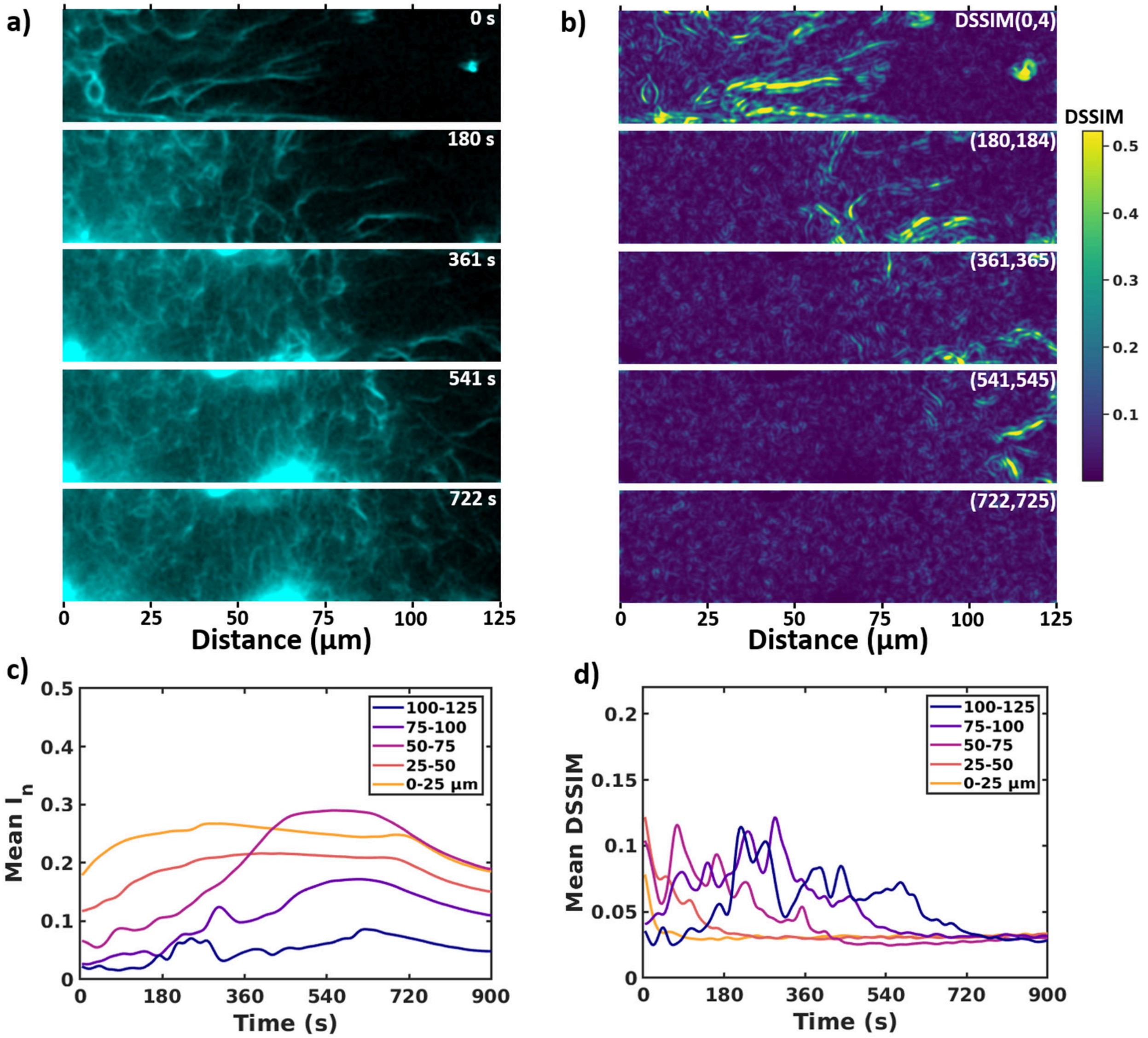

Figure 2.14 Intensity analysis of normalized CLSM images and high temporal resolution DSSIM images. a, CLSM snapshots highlighting the high dynamics for self-assembly at the gel front, processed with Eqs 1-4. b, DSSIM frame series of images takes 3.75 s apart, which captures fast dynamics. c, mean normalized intensity in each region show in a. d, mean DSSIM in each region seen in b.

A sliding-window Gaussian weighted mean was applied to the each DSSIM region-mean signal to smooth the data. A standard deviation of 3 data points was used to smooth each signal. Instantaneous peaks or valleys can be caused by one feature moving very rapidly. Ultimately, the same trends can be seen in both the raw and smoothed data, shown in Figure 2.15.

$$S_s = signal\ convolution(S_r, k_{gauss}) \quad \text{Eq 7}$$

S_s: Gaussian smoothed mean signal

S_r: Raw mean signal

k_{gauss}: 1D normalized Gaussian kernel

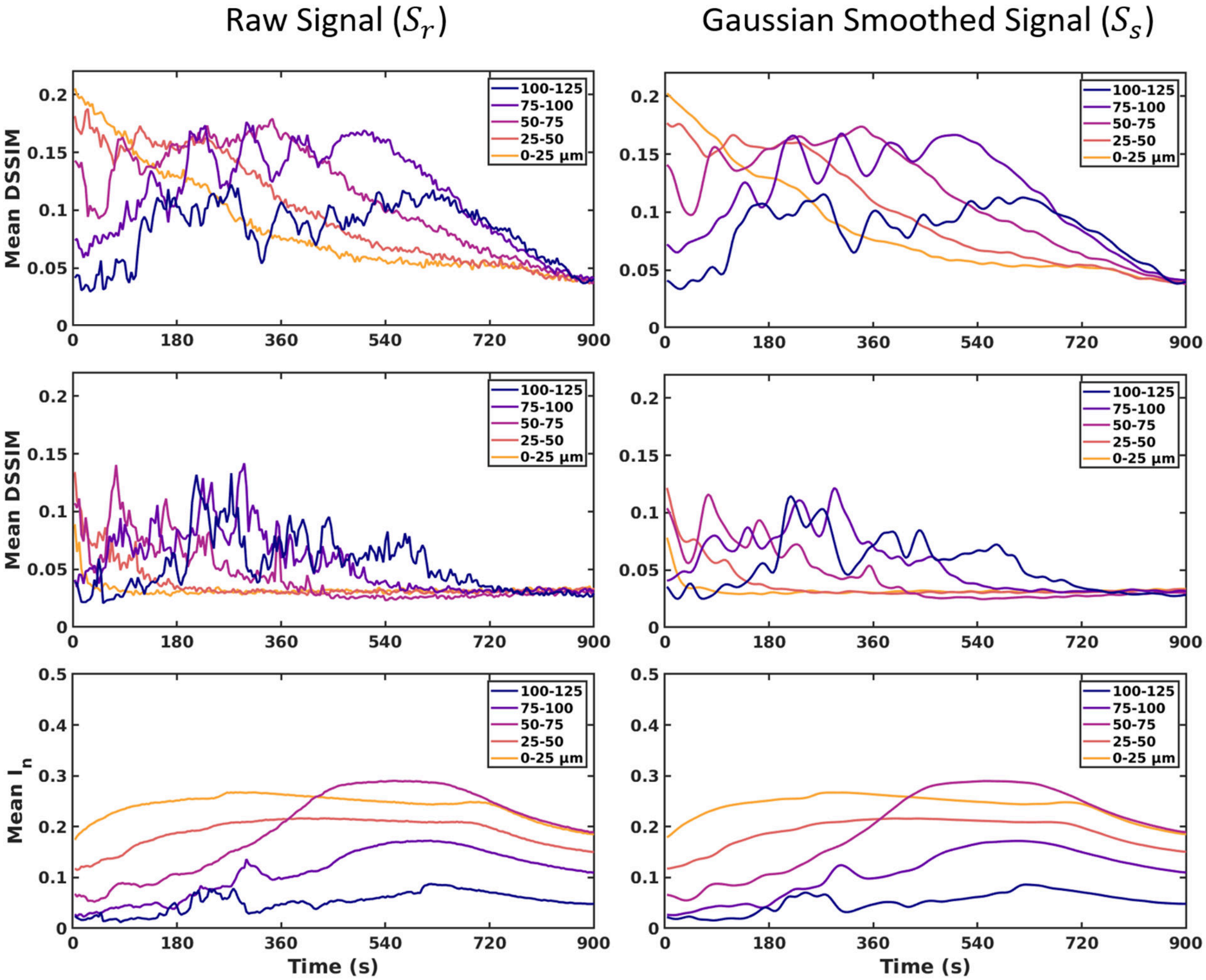

Figure 2.15 Comparison of raw signal to filtered signal used in Figure 2.13 and Figure 2.14f. Filtering was applied to smooth the signal via convolution of a normalized Gaussian Eq 7.

2.4.2 CLSM: Discussion

The self-assembly dynamics observed in the CLSM video were quantified using DSSIM analysis (Figure 2.13b,f). DSSIM is a standard measure of the difference between two images, which compares variation in the mean, variance, and cross-correlation between local regions of two images (Chapter 1). DSSIM images were obtained by comparing two frames taken 90 s (Figures 2.13) or 4 s (Figure 2.14) apart in a sliding-window calculation. The 90 s sliding-window calculation quantifies dynamics occurring over a large time window, while the 4 s sliding-window calculation captures the high temporal resolution dynamics. Each of the 240 DSSIM images was divided into five equally spaced regions with increasing distance from the working electrode, and the average DSSIM in each region is plotted for every frame (Figure 2.13, Figure 2.14).

The results show that the dissipative self-assembly system is highly dynamic, with the most dynamic changes at the fiber–water interface, which is seen for both the 90 and 4 s intervals. The dynamics decrease with distance from the fiber front, as can be seen with the time-delayed decline in DSSIM values starting with the 0–25 µm region, which is then echoed in the 25–50 and 50–75 µm regions. The 75–100 and 100–125 µm regions start with low DSSIM values, which steadily increase as the fiber–water interface progresses further from the electrode until a peak is reached and then gradually decline. The data also shows that the dynamics at the fiber–water interface are highest in the early stages and gradually decrease over time.

2.5 Conclusion

In this chapter, I have demonstrated how DSSIM analysis can be applied to LCTEM and CLSM datasets to derive materials insight on electrically fueled dissipative self-assembly processes. In the LCTEM dataset, I used DSSIM analysis as a segmentation-free method to capture a wave-like progression of materials assembly. The wave first propagates towards the electrode at a linear rate, then reflects away from the electrode at an accelerating rate. This feature suggests autocatalytic behavior from the system. My analysis also showed the material was most active within ~1 µm of the electrode. In the CLSM dataset, I used DSSIM analysis to quantify the electrically fueled formation of a fibrous gel. Because of the diffraction limitations of CLSM and the constantly changing material structures, segmentation of this dataset was not possible. However, DSSIM analysis was able to quantify the spatial and temporal features of the gel formation and showed a consistent rate of gel formation within ~100 µm of the electrode before decreasing. Together, the studies demonstrate how DSSIM analysis can be used to spatially and temporally quantify dissipative self-assembly processes in both LCTEM and CLSM datasets. From a wider perspective, these studies contribute towards understanding how the properties of dissipative systems can dynamically be controlled via electrical inputs. As electronic signals are found in many modern technologies, electrically-fueled dissipative materials may find potential applications in bioelectronics.[15,16]

2.6 References

(1) Van Rossum, S. A. P.; Tena-Solsona, M.; Van Esch, J. H.; Eelkema, R.; Boekhoven, J. Dissipative Out-of-Equilibrium Assembly of Man-Made Supramolecular Materials. *Chemical Society Reviews* **2017**, *46* (18), 5519–5535. https://doi.org/10.1039/c7cs00246g.

(2) Rieß, B.; Grötsch, R. K.; Boekhoven, J. The Design of Dissipative Molecular Assemblies Driven by Chemical Reaction Cycles. *Chem* **2020**, *6* (3), 552–578. https://doi.org/10.1016/j.chempr.2019.11.008.

(3) Ogden, W. A.; Guan, Z. Redox Chemical-Fueled Dissipative Self-Assembly of Active Materials. *ChemSystemsChem* **2020**, *2* (4). https://doi.org/10.1002/syst.201900030.

(4) Rizvi, A.; Mulvey, J. T.; Carpenter, B. P.; Talosig, R.; Patterson, J. P. A Close Look at Molecular Self-Assembly with the Transmission Electron Microscope. *Chem. Rev.* **2021**, acs.chemrev.1c00189. https://doi.org/10.1021/acs.chemrev.1c00189.

(5) De Jonge, N.; Ross, F. M. Electron Microscopy of Specimens in Liquid. *Nature Nanotechnology* **2011**, *6* (11), 695–704. https://doi.org/10.1038/nnano.2011.161.

(6) Omme, J. T. van; Wu, H.; Sun, H.; Beker, A. F.; Lemang, M.; Spruit, R. G.; Maddala, S. P.; Rakowski, A.; Friedrich, H.; Patterson, J. P.; Garza, H. H. P. Liquid Phase Transmission Electron Microscopy with Flow and Temperature Control. *J. Mater. Chem. C* **2020**, *8* (31), 10781–10790. https://doi.org/10.1039/D0TC01103G.

(7) Pu, S.; Gong, C.; Robertson, A. W. Liquid Cell Transmission Electron Microscopy and Its Applications. *Royal Society Open Science 7* (1), 191204. https://doi.org/10.1098/rsos.191204.

(8) Gibson, W.; Mulvey, J. T.; Das, S.; Selmani, S.; Merham, J. G.; Rakowski, A. M.; Schwartz, E.; Hochbaum, A. I.; Guan, Z.; Green, J. R.; Patterson, J. P. Observing the Dynamics of an Electrochemically Driven Active Material with Liquid Electron Microscopy. *ACS Nano* **2024**, *18* (18), 11898–11909. https://doi.org/10.1021/acsnano.4c01524.

(9) Selmani, S.; Schwartz, E.; Mulvey, J. T.; Wei, H.; Grosvirt-Dramen, A.; Gibson, W.; Hochbaum, A. I.; Patterson, J. P.; Ragan, R.; Guan, Z. Electrically Fueled Active Supramolecular Materials. *J. Am. Chem. Soc.* **2022**, jacs.2c01884. https://doi.org/10.1021/jacs.2c01884.

(10) Mulvey, J. T.; Iyer, K. P.; Ortega, T.; Merham, J. G.; Pivak, Y.; Sun, H.; Hochbaum, A. I.; Patterson, J. P. Correlating Electrochemical Stimulus to Structural Change in Liquid Electron Microscopy Videos Using the Structural Dissimilarity Metric. *Ultramicroscopy* **2024**, *257*, 113894. https://doi.org/10.1016/j.ultramic.2023.113894.

(11) Yao, L.; Ou, Z.; Luo, B.; Xu, C.; Chen, Q. Machine Learning to Reveal Nanoparticle Dynamics from Liquid-Phase TEM Videos. *ACS Cent. Sci.* **2020**, *6* (8), 1421–1430. https://doi.org/10.1021/acscentsci.0c00430.

(12) Woehl, T. J.; Park, C.; Evans, J. E.; Arslan, I.; Ristenpart, W. D.; Browning, N. D. Direct Observation of Aggregative Nanoparticle Growth: Kinetic Modeling of the Size Distribution and Growth Rate. *Nano Lett.* **2014**, *14* (1), 373–378. https://doi.org/10.1021/nl4043328.

(13) Rizvi, A.; Mulvey, J. T.; Patterson, J. P. Observation of Liquid–Liquid-Phase Separation and Vesicle Spreading during Supported Bilayer Formation via Liquid-Phase Transmission Electron Microscopy. *Nano Lett.* **2021**, *21* (24), 10325–10332. https://doi.org/10.1021/acs.nanolett.1c03556.

(14) Otsu, N. A Threshold Selection Method from Gray-Level Histograms. *IEEE Trans. Syst., Man, Cybern.* **1979**, *9* (1), 62–66. https://doi.org/10.1109/TSMC.1979.4310076.

(15) Song, E.; Li, J.; Won, S. M.; Bai, W.; Rogers, J. A. Materials for Flexible Bioelectronic Systems as Chronic Neural Interfaces. *Nat. Mater.* **2020**, *19* (6), 590–603. https://doi.org/10.1038/s41563-020-0679-7.

(16) Liu, Y.; Li, J.; Song, S.; Kang, J.; Tsao, Y.; Chen, S.; Mottini, V.; McConnell, K.; Xu, W.; Zheng, Y.-Q.; Tok, J. B.-H.; George, P. M.; Bao, Z. Morphing Electronics Enable Neuromodulation in Growing Tissue. *Nat Biotechnol* **2020**, *38* (9), 1031–1036. https://doi.org/10.1038/s41587-020-0495-2.

CHAPTER 3: Tracking transient nanofiber ordered phase in time-resolved cryoEM images via template matching and data science

This Chapter was adapted from a published article (PJ Hurst, JT Mulvey, RA Bone, S Selmani, RF Hudson, Z Guan, JR Green, JP Patterson. "CryoEM reveals the complex self-assembly of a chemically driven disulfide hydrogel" Chem. Sci. 2024, 15 (3), 1106–1116). Reproduce with permission from the Royal Society of Chemistry.

3.1 Abstract

biological organisms are capable of creating dynamic structures through fuel-driven dissipative self-assembly. In order to mimic this behavior, a variety of synthetic self-assembly processes have been developed that result in the transient formation of polymer structures. These structures form through two simultaneous reactions, forward and backward, which generate and break down self-assembled structures. Here, we present research on a chemically driven redox system where it was possible to separately perform the forward and backward reactions, or perform them synchronously. We discovered the existence of a transient stacked nanofiber phase, and designed a systematic time-resolved cryogenic transmission electron microscopy (cryoEM) study to track this phase over the course of the reactions. Consistent image acquisition conditions enabled a two-step quantitative image analysis pipeline, in which the stacked fiber phase was first segmented in each image using a cross-correlation based template matching. Data science was used to modify the segmentation algorithm to account for variations in TEM defocus, which is impossible to perfectly control when imaging the sample. In step two, the number of fibers contained in each of the stacked fiber domains was counted and labeled with the degree of stacking. Our key finding is that a thermodynamically unstable stacked fiber phase, briefly observed in the backward reaction, is sustained for ~6 hours in the synchronous process. The collective data suggests that chemically driven self-assembly can create sustained morphologies not seen in thermodynamically stable assemblies by kinetically stabilizing transient intermediates.

3.2 Introduction

In Chapter 2, I discussed electrically-fueled dissipative self-assembly of the CSH/CSSC system. In those studies, the electrode was supplying the fuel to the forward assembly reaction.[1,2] In this chapter, I will present a study on chemically-fueled dissipative self-assembly.[3] In this case, the fuel being used to drive the forward reaction is the chemical fuel peroxide (H_2O_2), and dithiothreitol (DTT) is still present as the chemical reductant. A key benefit of this system is that it is possible to isolate the individual steps of the reaction sequentially (Figure 3.1). It is possible to only mix H_2O_2 and CSH to initiate the forward reaction (assembly). Then the H_2O_2 can be removed and DTT can be added to evaluate only the backward reaction (disassembly). Alternatively, all components can be mixed from the start to study the synchronous reaction. Because the steps can be isolated, this system is ideal for studying the structural differences in the sequential (forward then reverse) reactions compared to the synchronous reaction.

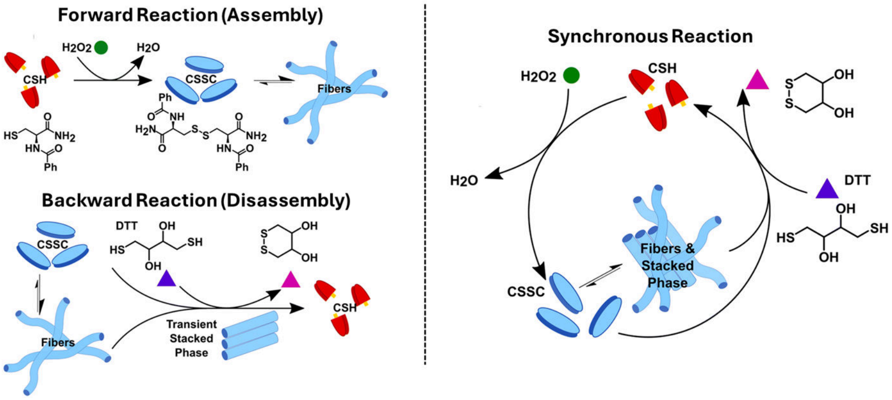

Figure 3.1 Chemically-fueled dissipative self-assembly. Left shows the sequential process separated into the forward assembly reaction and backward disassembly reaction. Right shows the combined synchronous reaction.

This system was studied with a series of time-resolved cryoEM experiments. In cryoEM, the solution sample is rapidly frozen, or vitrified, which makes it possible to image snap-shots of the system during specific time points in the reaction. The advantage of cryoEM over LCTEM is that cryoEM provides higher-resolution structural information on the system, and several images can be taken of the sample at different locations, rather than the single imaging location in LCTEM.[4] Additionally, the electron beam cannot influence the reaction and will not affect the results. The main disadvantage of cryoEM is that each timepoint requires a new TEM sample to be prepared which is very time and labor intensive. This severely limits the temporal resolution of the technique. For a complete description of the material system and microscopy methodology, the reader is directed to the complete manuscript.[5] The information presented here will focus primarily on the image analysis methods applied to the dataset.

In this chapter, I describe the image analysis and data science methods I used to analyze a time-resolved cryoEM dataset of the chemically-fueled CSH/CSSC system. The dataset consists of 770 cryoEM images collected across 24 timepoints of the reactions. The data collection was carried out at a standard set of microscope conditions which were ideal for large-scale data analysis. The goal of the analysis was to track the presence of a highly-ordered stacked fiber phase which appeared during the backward reaction and in the dissipative reaction. The first part of the algorithm uses cross-correlation based template matching to identify the stacked fiber phase in each image.[6] The second part of the algorithm labels the degree of stacking in each domain, which quantifies the organization of the local fibers. The combined analysis reduces the 770-image dataset to a few simple graphs that are simple to interpret. The analysis clearly shows the dissipative system is sustaining this thermodynamically unstable phase, which was an unexpected and exciting result.

3.3 Methods

To quantify and track the fiber stacking, we developed an in-house MATLAB script to segment and analyze the stacked fiber phase. Stacked fiber domains were identified by first producing normalized cross-correlation maps using 108 synthetic templates to select for the stacked phase at different fiber spacings and angles in each image (Figure 3.2). This was possible because all cryoEM images were captured at the ame nominal magnification (30k), so the pixel size of the fiber structures was consistent. It was found that the variation in microscope defocus impacted the normalized cross-correlation, so cross-correlation map thresholding was adjusted depending on the defocus of each image, which was estimated via radial integration of the fast-Fourier transform (Figure 3.4). Finally, fibers within the segmented domains were identified and labeled with the number of adjacent fibers, defined as the degree of stacking (DoS) (Figure 3.6A–D and S18). The image analysis pipeline was used to analyze 770 cryoEM images across 24 experimental conditions generating 398 million data points (Figure 3.6-3.9). The resulting analysis tracks the structural evolution of the system by temporally quantifying the mean DoS (Figure 3.6E), DoS distribution (Figure 3.6F), and percent coverage (Figure 3.9) present at each timepoint.

3.3.1 Selection of cryoEM parameters:

Preliminary studies were carried out to optimize all cryoEM parameters. A TEM magnification of 30k was selected for magnification as it is the highest magnification that does not cause visible beam damage of the sample using low dose imaging. This allows a large area of the sample to be inspected in a single image. On average, each timepoint had approximately 30 images collected. We opted to capture additional timepoints rather than repeating the sample multiple times with a smaller number of time points. We were also sensitive to the image processing time and therefore had to find a balance between the number of images collected and time required for image processing. Our study encompassed 770 images which were processed in parallel using the UCI HP3. Each image was allocated 30 cores, 100GB of RAM, and 1 hour of processing time. It took approximately 23,000 core-hours in total. Because of efficient parallelization, the time to complete the entire analysis was 5 hours for a given set of parameters. This processing collected 398 million data points with an average of over 500,000 per image with a very large standard deviation as images contain little to no stacking.

3.3.2 Cross-Correlation Template Generation

Several symmetric templates of alternating black and white stripes were systematically generated to act as templates of the stacked fiber phase. Fibers of different thicknesses were accounted for by generating template sets with three different pixel spacings: 15, 20, and 25 pixels (Figure 3.3). Furthermore, templates were rotated 175 degrees at 5-degree intervals, resulting in 36 templates for each pixel spacing, and 108 templates in total. Finally, the templates were masked to be circular which makes them symmetric to all fiber directions, such that diagonal fibers do not have higher cross-correlations compared to vertical fibers.

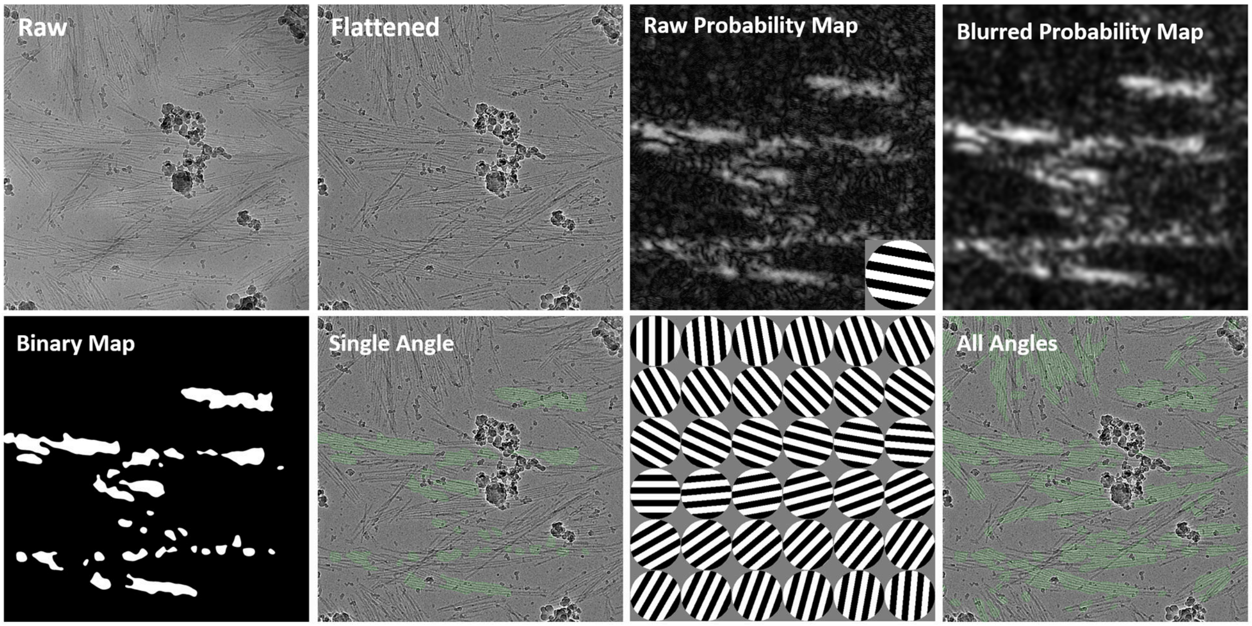

Figure 3.2 Image processing pipeline for stacked fiber phase segmentation. The image processing steps are outlined for a representative image. A more detailed description of each step can be found in the text below. The templates have been increased in size for display purposes.

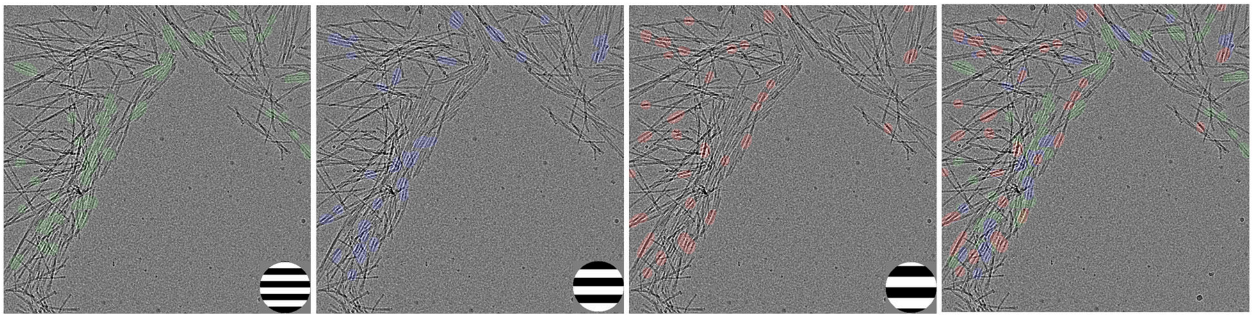

Figure 3.3 Individual segmentation maps for template pixel spacings of 15, 20, and 25 pixels. The templates have been increased in size by 4x for display purposes. The right figure shows an overlay of the 3 individual maps and demonstrates how different template spacings are used to identify different fiber stack spacings in the image. Note some highlighted regions are single fibers and not fiber stacks, these will be removed from the dataset during fiber stack labeling.

3.3.3 Stacked fiber phase segmentation

Figure 3.2 shows the image processing pipeline applied to each cryoEM image. First, a high pass filter was applied to remove background features and create a flat image. Next, the normalized cross-correlation is computed between each template and the flattened image which results in a correlation probability map. The absolute value of this map is taken, which results in equal positive weight to correlation and anticorrelation. This is helpful because a high probability is returned both when the black pixels line up with the fibers and white pixels line up with the fringes (correlation), and also when white pixels line up with the fibers and black pixels line up with the fringes (anticorrelation). Next, the correlation probability map is smoothed with a Gaussian blur to smooth out the high correlation regions. Then, a probability threshold was used to convert the probability map into a binary segmentation map. Different probability thresholds were used for each image and were based on the estimated defocus of the image (Figure 3.4, details in ‘Defocus Threshold Correction‘). Binary maps for the 36 angles are calculated individually for each of the 3 templated spacings, resulting in 108 total binary maps. Finally, angles are combined across the 3 template spacings by adding the binary maps together for each angle, producing 36 binary maps which contain information about both the fiber stack location and fiber stack angle. Note the angular information is used to label the degree of stacking, as discussed in ‘Labeling Degree of Stacking’.

3.3.4 TEM defocus correction

It is well known that the brightness of the Fresnel fringes around an object will depend on the defocus of the microscope; larger microscope defocus values lead to higher intensity of the Fresnel fringes. We found that TEM images taken at higher defocus values were more sensitive to the segmentation algorithm and had higher normalized cross-correlations values. This makes physical sense, because the algorithm relies on the pattern of alternating dark fibers and bright fringes. If the fringes are brighter in some images due to differences in focus, it will increase the values of the normalized cross-correlations. To minimize this effect, all images were taken around 11 μm of defocus using the autofocus feature in SerialEM. However, there was still significant variation in defocus between images. To account for this variation in the segmentation algorithm, we estimated the defocus of every image and adjusted the probability threshold for segmentation on a per-image basis.

We estimated the defocus of every image by first calculating the Fast Fourier transform (FFT) image and then taking a radial integration (Figure 3.4A-B). Then, we used a peak-finding algorithm to find the distance to the second peak in the radial integration, which is characteristic of the defocus value (Figure 3.4C). The second peak was chosen because the first peak appeared distorted in many images, likely from high-frequency components generated by small features in the images such as fibers. We then took CryoEM images of amorphous ice with no sample at known defocus values to use as a calibration curve to convert the second-peak distances to the defocus of the images (Figure 3.4D). Note that our algorithm was unable to detect peaks below 7 µm of defocus, but this was below the range of defocus values found in the experimental datasets. Once all images were labeled with the defocus value, the probability threshold for segmentation was adjusted with an empirically determined function (Figure 3.4E).

Originally, a static threshold of 0.145 was used to segment all images, which appeared to work well for most images. However, we observed that images taken at high defocus had inaccurate segmentation and were over segmented. We quantified this observation by examining the correlation between image defocus and the number of segmented pixels in an image, which should be random and uncorrelated features. To examine these features, we plotted the mean segmented pixels across images in different 1 µm defocus ranges, from 7-8 µm, 8-9 µm, 9-10 µm etc. (Figure 3.4F). Defocus and mean segmented pixels should be uncorrelated features and yet there is clearly a trend when a static threshold of .145 was used; high defocus images had a greater number of segmented pixels. After the defocus threshold correction was applied, the trend was reduced and a more random correlation between defocus and the number of segmented pixels was observed (Figure 3.4F). Figure 3.4G shows an uncorrected image which was over segmented while Figure 3.4H shows more accurate segmentation after the defocus threshold correction.

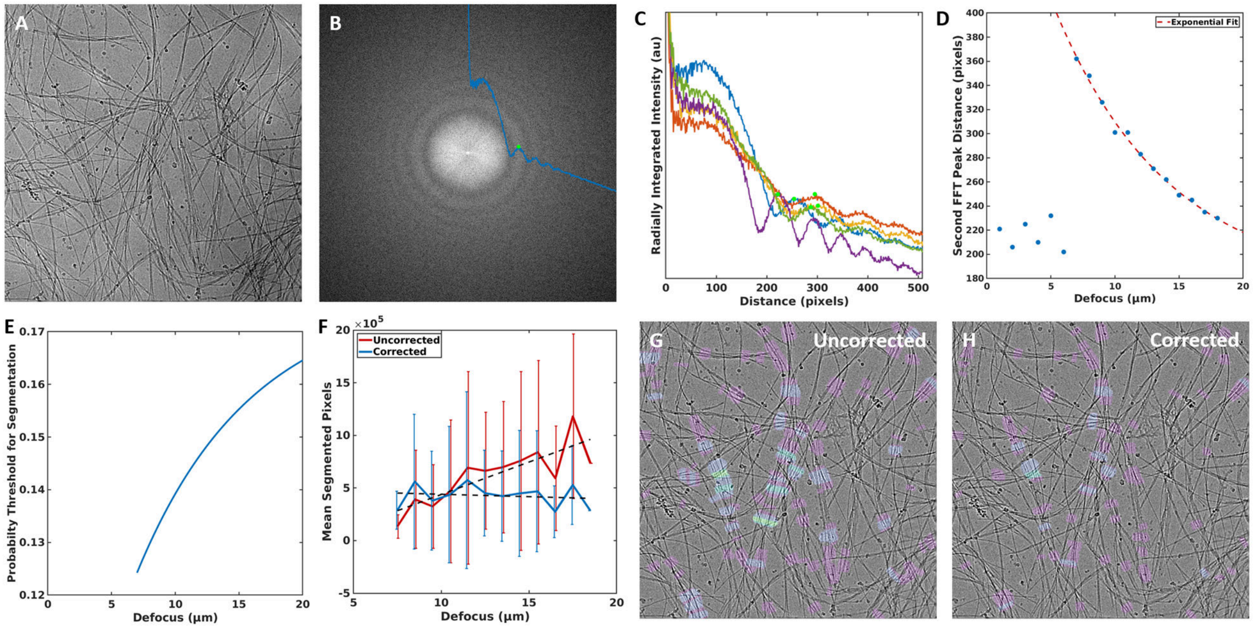

Figure 3.4 Defocus correction for segmentation algorithm. A) Typical TEM image with B) corresponding FFT image. Blue line represents radial integration of the FFT, with the green dot labeling the calculated second-peak distance. C) Examples of several radially integrated FFTs from images at different defocuses with the calculated second-peak distance. D) Calibration curve which relates defocus value to the calculated second-peak distance. Points below 7 µm were omitted from the fit. E) Empirically determined curve which adjusts probability threshold for segmentation as a function of image defocus. F) Mean segmented pixels of images across different defocus ranges. There was a clear correlation in the uncorrected curve which has been removed in the corrected curve. Dashed line represents linear fit. Error bars represent standard deviation. G) Uncorrected image with threshold of .145 showing over segmentation compared to H) segmentation after defocus threshold correction.

3.3.5 Labeling degree of stacking

After the stacked fiber phase was segmented, the goal was to track how well-ordered the stacked phase was by quantifying the degree of stacking (DoS) within each fiber stack structure. The DoS is the number of fibers present in the local region of the stacked fiber phase. Higher degrees of stacking are more ordered and entropically less favorable than lower degrees of stacking. To understand how the structures were evolving during the sequential and synchronous processes, it was important to accurately quantify the amount and distribution of stacking present at each timepoint.

The output of the fiber stack phase segmentation algorithm is 36 binary maps of the stacked phase at each angle. Each angle was analyzed individually. For each binary object in the segmentation map, the stacked phase was cropped, then rotated to be oriented vertically. The rotation angle is equal to the rotation angle of the template. Once oriented vertically, a sliding window vertical integration was performed across 100 pixels (Figure 3.5A) to produce a high signal-to-noise 1D intensity profile (Figure 3.5B). A peak-finding algorithm was applied to find the intensity valleys created by the fibers, which were then labeled (Figure 3.5D). This resulted in a local label for the number of fibers at every location in the stacked phase. Small gaps in the labeling resulting from noise and non-fiber objects were smoothed over.

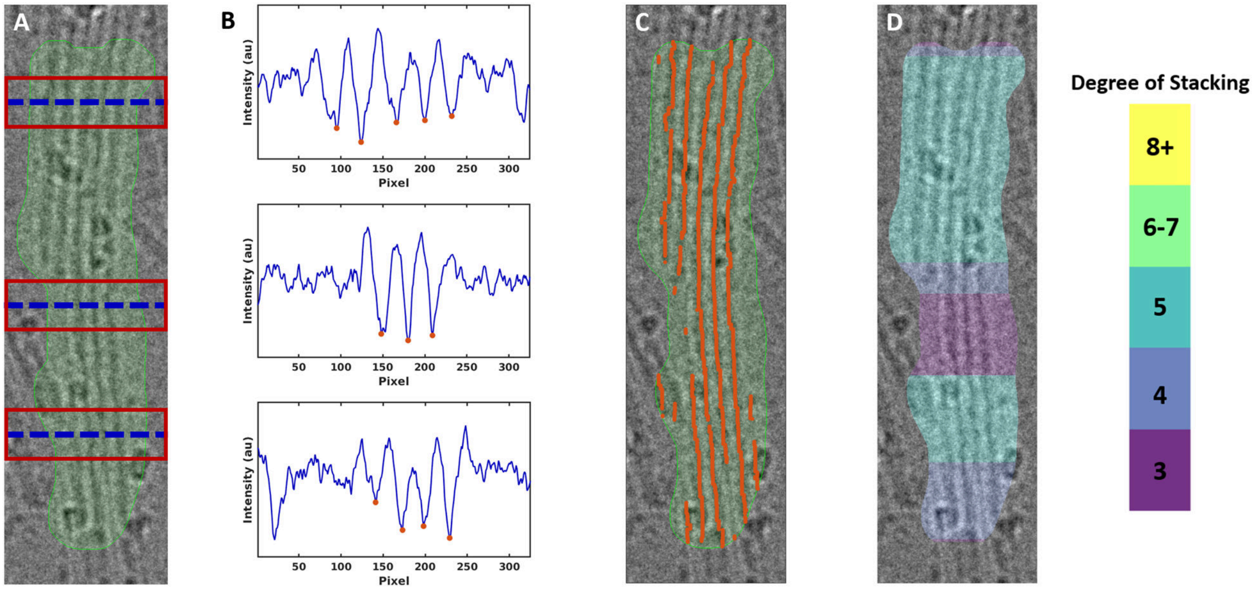

Figure 3.5 Labeling degree of stacking. A,B) snapshots of integrated profiles at different locations in the fiber stack. Fibers are labeled with orange dots. C,D) The number of fibers at each location is then counted and labeled.

Once each of the 36 angles were analyzed, they were combined into a single DoS map. Because of the large number of angles used, the same fiber stack was often segmented and labeled by 2 or more different angles of the templates. To resolve this conflict between angles and prevent multiple counting, the maximum DoS was taken for each labeled pixel. This was done because the most fibers were counted when the angle of the template best matched the angle of the stacked phase, and the highest DoS was recorded.

3.4 Results

The stacked fiber phase segmentation and labeling image analysis pipeline was applied to 770 CryoEM images across 24 experimental timepoints, generating 398 million DoS datapoints. A datapoint is defined as a pixel labeled with the DoS. A subset of labeled images is shown in Figure 3.7. The data generated from segmentation and labeling was used to track the structure of the stacked fiber phase across all timepoints in this study.

We analyzed the mean DoS in each timepoint in order to clearly quantify the stacked phase of each process over time. The mean DoS presented in Figure 3.6E is determined by treating each image as an independent observation of the entire population of stacked fibers present within each timepoint. First, the “observed DoS” was calculated for each image by taking the sum of labeled DoS datapoints divided by the number of datapoints. By the central limit theorem, the set of observed DoS values should have a Gaussian distribution even though the population of fiber stacks does not have a Gaussian distribution.

Next, the “mean observed DoS” was calculated for each timepoint, which is defined as the mean of the observations (Figure 3.6E). Importantly, this calculation gives each image (observation) an equal weighting in the calculation of mean observed DoS. This would assume each image contributes the same number of datapoints. However, due to the stochastic nature of the system, the distribution of datapoints is very heterogenous; some images contain a very small number of datapoints or no datapoints. To account for this and remove outliers, images contributing less than 2% of the total datapoints for a given timepoint were removed from the mean observed DoS calculation Next, we used the standard error and the t-distribution to compute the 95% confidence intervals of the mean, which are represented by the black error bars in Figure 3.6E and Figure 3.8. Accordingly, we are 95% confident the mean DoS of the entire population will fall within the error bars.

In addition to this analysis, the “mean combined DoS” was calculated for each timepoint (Figure 20). In this case, the datapoints from each image within a timepoint were combined into a single large dataset. Then, the mean DoS value of this combined dataset was calculated (mean combined DoS). In this calculation, each observation is not given an equal weighting in the mean; images with a large number of stacked fibers will contribute more heavily to the mean combined DoS. For comparison, the mean combined DoS was plotted with the mean observed DoS (Figure 3.8, green dots). Figure 3.8 shows the mean combined DoS values fall within the 95% confidence interval of the mean observed DoS values for all conditions.

Finally, we examined the distribution of DoS datapoints within each timepoint. Figure 3.6F shows a normalized bar graph of the distribution which clearly shows there is more high-order stacking in Sequential 1579 s, Synchronous 6060 s, and Synchronous 13440 s. Furthermore, we analyzed the amount of stacked phase present in the CryoEM images (Figure 3.9). For each timepoint, the binary labeled pixels in each image were combined and then divided by the total pixels (image resolution multiplied by number of images in the timepoint). In addition, the percent coverage was calculated individually for each image within a timepoint and used to calculate the standard deviation of coverage. Note the standard deviation of labeled pixels treats all DoS values binary values.

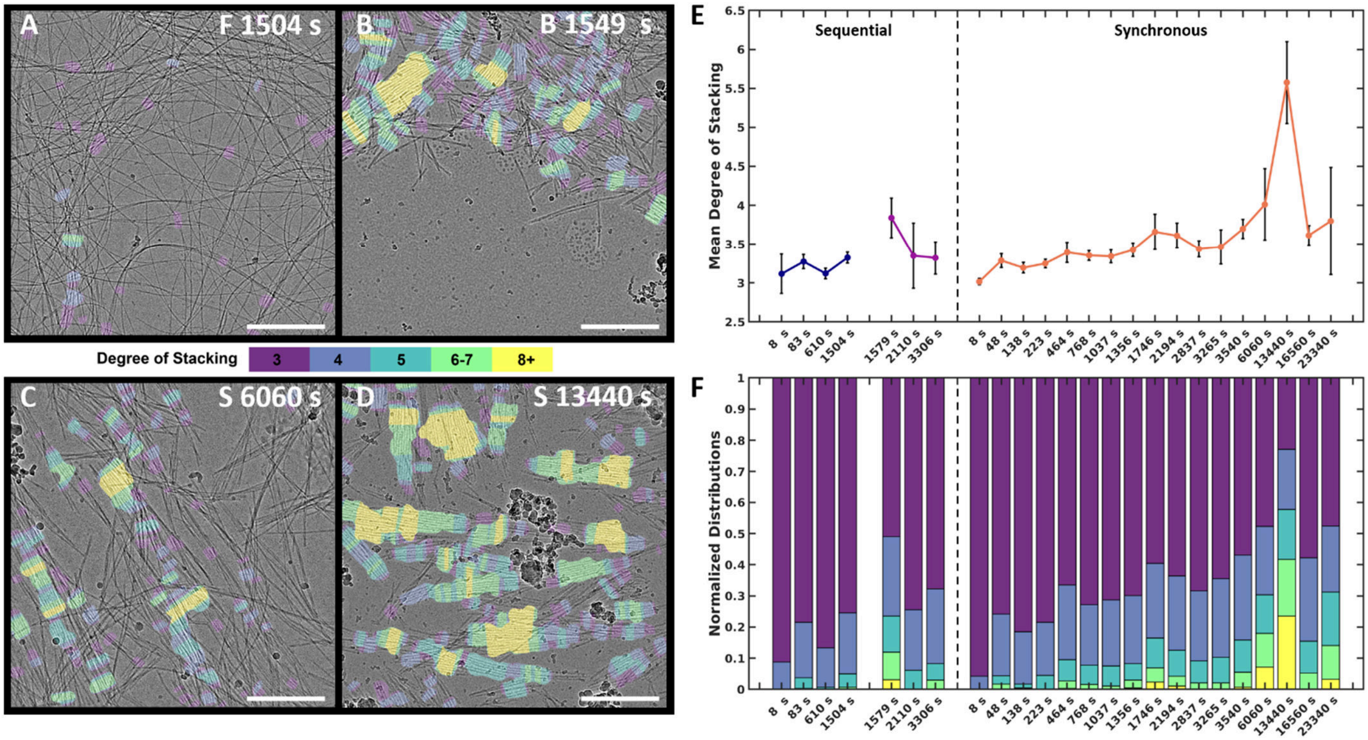

Figure 3.6 Quantitative image analysis of the stacked fiber phase. (A–D) Selection of labeled frames from key timepoints. Colored tinting corresponds to the degree of stacking. F = forward, B = backward, S = synchronous. (E) Mean DoS for each timepoint, high values indicate higher order in the system. Black error bars represent 95% confidence interval of mean. (F) DoS datapoint distribution normalized to 1 for comparison between timepoint. Scale bars 300 nm.

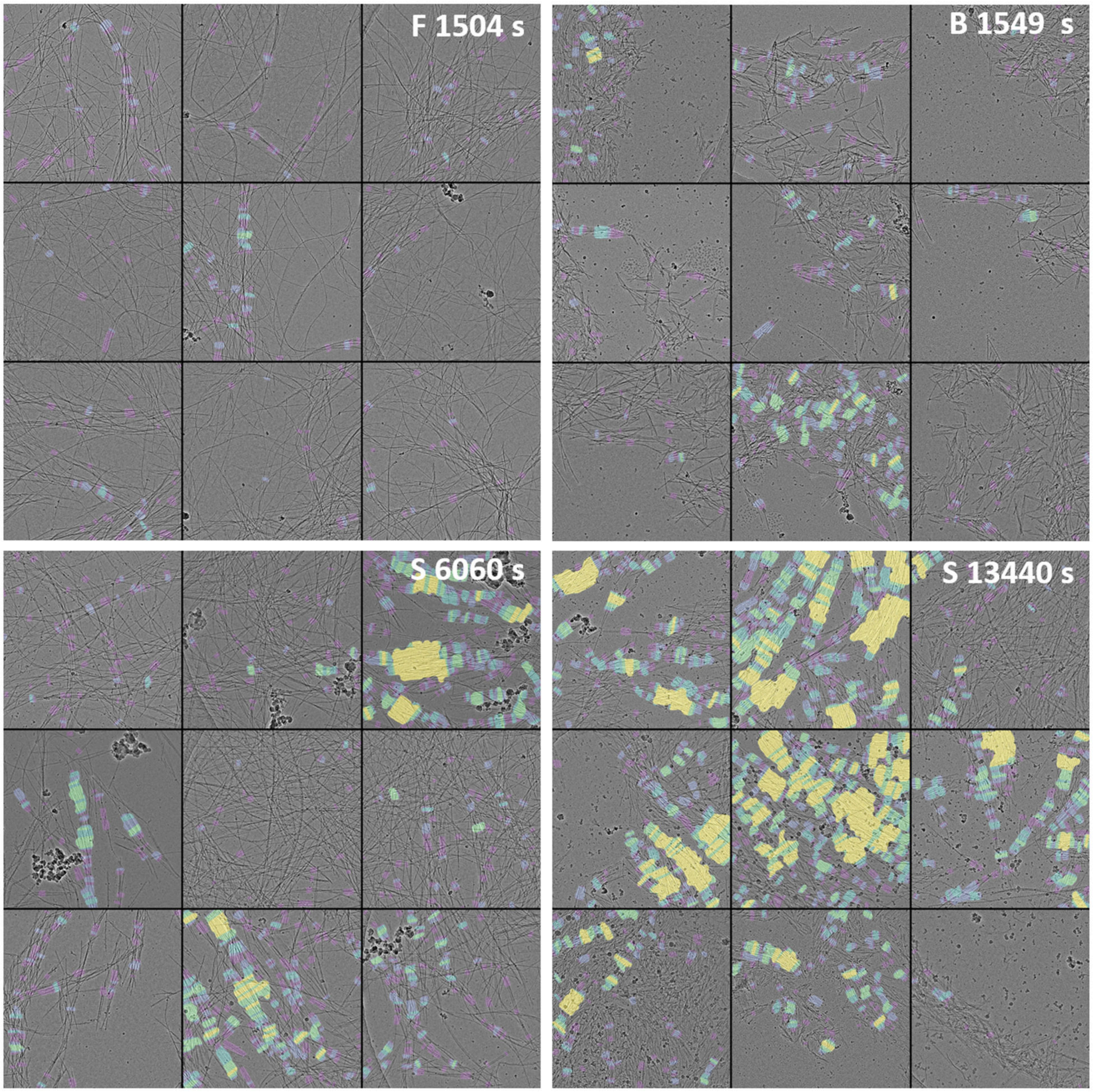

Figure 3.7 Examples of labeled images.

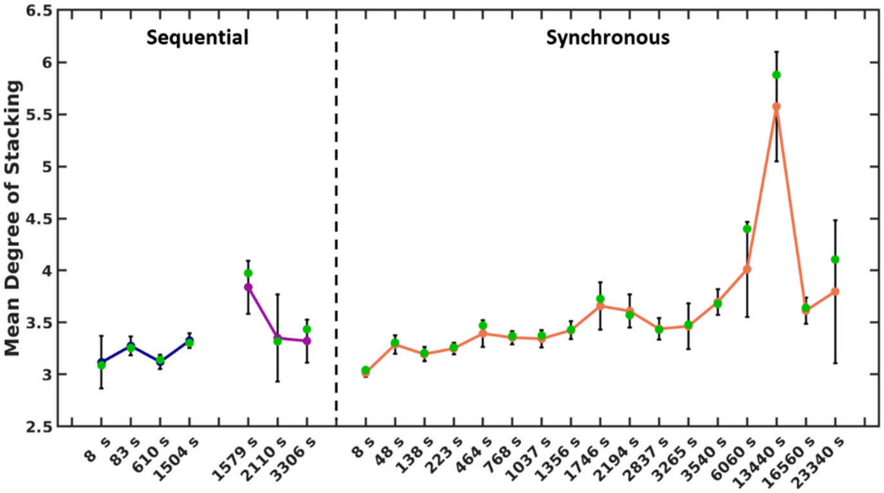

Figure 3.8 Display of Figure 3.6E with the mean combined DoS labeled for each timepoint (green dots).

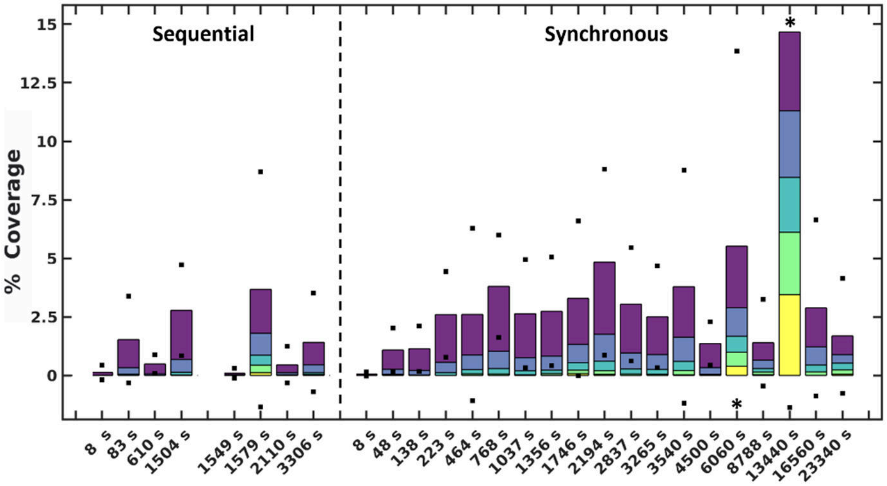

Figure 3.9 Density distribution of each timepoint, defined as the total number of labeled pixels divided by the total number of pixels in each timepoint. Black dots represent standard deviation of image densities within each timepoint. (*) represents standard deviation points omitted for visibility.

3.5 Discussion

The analysis reveals that both the sequential and synchronous processes show the presence of the stacked fiber phase but exhibit different temporal behavior. In the sequential study, the forward process shows a low mean DoS with distributions dominated by low-DoS (≤4), which comes from the random distribution of fiber locations and relatively weak inter-fiber interactions (Figure 3.6A). In contrast, the first timepoint in the backward reaction shows a sharp increase in mean DoS, indicating a substantial increase in inter-fiber interactions (Figure 3.6B and E). The later timepoints show the system returning to a low DoS distribution, supportive of the previous qualitative observations that the high-DoS (≥5) stacked fiber phase is transient (Figure 3.6E and F).

In the synchronous process, the mean DoS plot shows a gradual shift towards higher DoS structures during the first hour. The 6060 s and 13440 s timepoints (Figure 3.6C and D) show a significant increase in 8+ DoS (Figure 3.6F and S21), and the 13440 s timepoint shows the highest mean DoS for all samples analyzed (Figure 3.6E). This observation suggests that certain conditions can be exploited to control the order and amount of stacked fiber phase present in the system. Later timepoints reveal a drop in stacked phase density (Figure 3.9), while some high DoS domains persist (Figure 3.6F). The data shows that the high-DoS structures are present for a period of >6 hours, which is substantially longer than the <600 s lifetime observed in the sequential system. The data also suggests that evolution of the stacked phase is a complex process. Figure 3.6E shows subtle increases and decreases in the synchronous data which may indicate the amount stacked fiber phase present in the system is oscillating.

3.6 Conclusion

In summary, we have compared the self-assembly mechanisms for a conventional sequential assembly–disassembly process and a synchronous process. Image processing was used to track the presences of a thermodynamically unstable phase within the sequential and synchronous process. Importantly, the image analysis presented here was only possible due to careful collection of the data, which involved an initial trial-and-error stage to determine the best microscope conditions for quantitative image analysis. Once these conditions were determined, all images in the 24 experimental timepoints were collected at the same conditions. The results presented above were only possible to obtain because the data collection was designed from the start with the intention to perform quantitative image analysis and data science. These results contributed well to support the overall narrative, and made it possible for the scientific community to easily interpret the trends occurring in the large cryoEM dataset of 770 images. The analysis also made it possible to easily compare the trends seen in cryoEM to the trends found in kinetic Monte Carlo simulations of this system (details in full publication). From a broader point of view, the overall findings presented here provide information on how to tune the reaction kinetics to select for and enhance the yield of a transient, well-ordered phase. We anticipate that these findings will also be useful for understanding how higher-ordered systems are maintained using synchronous chemistry and will aid in establishing tunable structure–property relationships in applied materials.

3.7 References

(1) Selmani, S.; Schwartz, E.; Mulvey, J. T.; Wei, H.; Grosvirt-Dramen, A.; Gibson, W.; Hochbaum, A. I.; Patterson, J. P.; Ragan, R.; Guan, Z. Electrically Fueled Active Supramolecular Materials. *J. Am. Chem. Soc.* **2022**, jacs.2c01884. https://doi.org/10.1021/jacs.2c01884.

(2) Gibson, W.; Mulvey, J. T.; Das, S.; Selmani, S.; Merham, J. G.; Rakowski, A. M.; Schwartz, E.; Hochbaum, A. I.; Guan, Z.; Green, J. R.; Patterson, J. P. Observing the Dynamics of an Electrochemically Driven Active Material with Liquid Electron Microscopy. *ACS Nano* **2024**, *18* (18), 11898–11909. https://doi.org/10.1021/acsnano.4c01524.

(3) Ogden, W. A.; Guan, Z. Redox Chemical-Fueled Dissipative Self-Assembly of Active Materials. *ChemSystemsChem* **2020**, *2* (4). https://doi.org/10.1002/syst.201900030.

(4) Rizvi, A.; Mulvey, J. T.; Carpenter, B. P.; Talosig, R.; Patterson, J. P. A Close Look at Molecular Self-Assembly with the Transmission Electron Microscope. *Chem. Rev.* **2021**, acs.chemrev.1c00189. https://doi.org/10.1021/acs.chemrev.1c00189.

(5) Hurst, P. J.; Mulvey, J. T.; Bone, R. A.; Selmani, S.; Hudson, R. F.; Guan, Z.; Green, J. R.; Patterson, J. P. CryoEM Reveals the Complex Self-Assembly of a Chemically Driven Disulfide Hydrogel. *Chem. Sci.* **2024**, *15* (3), 1106–1116. https://doi.org/10.1039/D3SC05790A.

(6) Briechle, K.; Hanebeck, U. D. Template Matching Using Fast Normalized Cross Correlation; Casasent, D. P., Chao, T.-H., Eds.; Orlando, FL, 2001; pp 95–102. https://doi.org/10.1117/12.421129.

CHAPTER 4: Observation of liquid−liquid-phase separation and vesicle spreading during supported bilayer formation via liquid-phase transmission electron microscopy

This Chapter was adapted from a published article (Aoon Rizvi, Justin T Mulvey, Joseph P Patterson. "Observation of Liquid–Liquid-Phase Separation and Vesicle Spreading during Supported Bilayer Formation via Liquid-Phase Transmission Electron Microscopy." Nano Lett. 2021, 21, 24, 10325–10332).

4.1 Abstract

Liquid cell transmission electron microscopy (LCTEM) enables the real-time visualization of nanoscale dynamics in solution. Here, we study the formation of block-copolymer-supported bilayers using LCTEM. We observe two formation pathways that involve either liquid droplets or vesicles as intermediates toward supported bilayers. In the first dataset, segmentation analysis is used to characterize vesicle spread rates and track the rupture of a vesicle membrane as it transitions into a bilayer. In the second dataset, a cross-sectional time series is used to show the origin of defect formation in a supported bilayer. Our results suggest that bilayer assembly methods that proceed via liquid droplet intermediates should be beneficial for forming pristine supported bilayers. Furthermore, this study demonstrates that supported bilayers inside the liquid cells may be used to image membrane interactions with proteins and nanoparticles in the future.

4.2 Introduction

Amphiphilic block copolymers (BCP) are polymers composed of 2 homopolymer blocks with different polarities that are covalently connected. Similar to lipids, amphiphilic BCPs are capable of self-assembling into a variety of hierarchical structures such as micelles, vesicles, and bilayers. The final structure depends on the thermodynamic conditions during the self-assembly process such as temperatures, block length, and solvent environment. It is also possible to induce a structural transition by changing the thermodynamic conditions, such as heating a solution of worms (cylindrical micelles) to produce micelles.[1] Furthermore, BCP self-assembly processes can be kinetically controlled by slowly or rapidly changing the thermodynamic conditions.

BCP solid-supported bilayers are commonly studied for applications in microchannel transport and protein embedding.[3] A common method of forming a bilayer is through rupturing a vesical onto a solid surface.[4] While this method has been widely adopted by the bilayer community, the exact mechanisms of vesicle rupture are still unknown.[5] Previous studies have observed this process with optical microscopy, but the diffraction-limited resolution hinders mechanistic insight.[6] There have also been many attempts to model solid-supported vesicle rupture with molecular simulations,[7] but the spatial and temporal scale of simulations are difficult to establish and verify without direct nanoscale observation.

LCTEM offers an ideal environment to study vesicle interactions with a solid surface at nanoscale resolution. Aoon Rizvi of the Patterson Lab captured two bilayer formation pathways using LCTEM. These experiments were conducted on the BCP polystyrene-block-polyacrylic (PS200-b-PAA35) in a THF:dioxane solution undergoing a morphological transition during a solvent-exchange process, in which water is flown into the liquid cell to induce the transformation. In the first dataset, a vesicle can be seen rupturing and spreading across the chip surface. In the second dataset, liquid structures can be seen diffusing, coalescing, and then spreading to cover the entire chip surface to form a bilayer. The two bilayer formation mechanisms are illustrated in Figure 4.1. For a complete description of the material system and microscopy methodology, the reader is directed to the complete manuscript.[8] The information presented here will focus primarily on the image analysis methods applied to the dataset. The text below described quantitative image analysis methods which were used to characterize and quantify these two different processes.

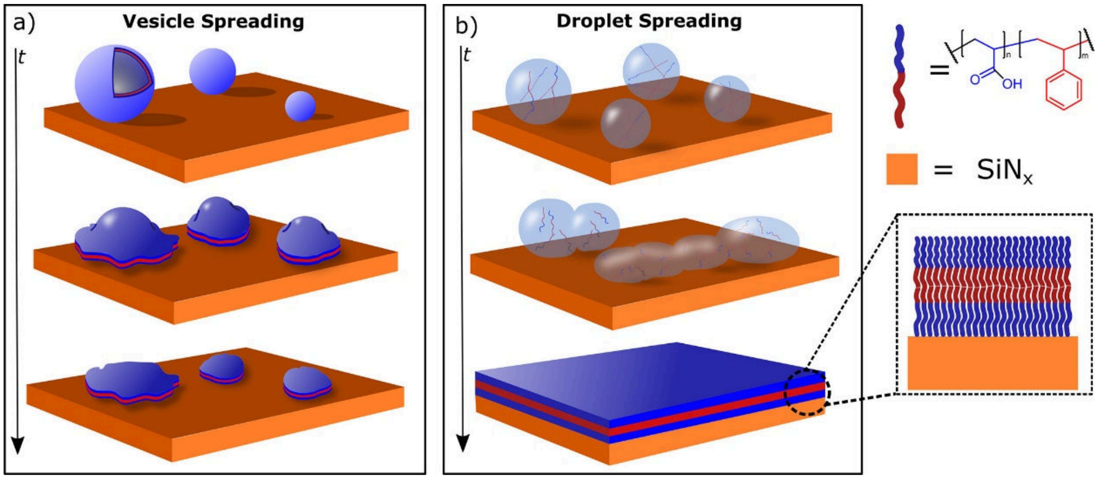

Figure 4.1 Schematic of the two pathways observed during bilayer formation. (a) Vesicle spreading: the block copolymers were observed to form vesicles that grew, ruptured, and spread to form supported bilayers. (b) Droplet spreading: the block copolymers were observed to undergo liquid–liquid-phase separation to form droplets that spread over the surface to form supported bilayers.

4.3 Methods and Results

The goal of this analysis was to study the kinetics of vesicle rupture by measuring changes in area and contrast of the particles (Figure 4.3). This required accurate segmentation maps – binary images which distinguish the particle from the background. A series of standard processing techniques were used to improve signal and correct for artifacts introduced from the liquid cell.[9] Then, the Otsu method was used to segment the images by statistically calculating an intensity threshold to separate the object and background,[10] and the resulting binary map was processed with morphological operations followed by a custom function to define the perimeter of the particle. The resulting segmentation maps were used to quantitatively analyze the changes in size and contrast of 4 individual particles in the experimental system and 2 particles from the control experiments.

4.3.1 Image pre-processing

The raw images were imported into MATLAB directly from the Digital Micrograph 4 image files without compression. They were then processed with standard processing techniques outlined in Figure 4.2. First, the 99.9% and .1% outliers were removed from the frame and replaced with the 99.9% and .1% value.

Next the images were aligned in the dataset. There is often camera drift over the course of the LCTEM, and this is likely the primary source of the global shift. Frame alignment was accomplished by finding the center of mass of the same particle in each frame, and then aligning based on the center of mass (COM). This was done iteratively, by first inverting the image so the dark pixels representing the particles became bright, meaning they had a high mass in the calculation. An initial COM guess was given manually for each particle. Then, a 329 x 329 pixels (729 nm by 729 nm) area around this COM guess was cropped, and the COM of the crop was calculated. The newly calculated COM was then used as the starting guess for the next iteration. This was done iteratively until the COM converged (the same COM was calculated for multiple iterations). Local pixels around the converged COM were calculated to ensure it was not a local minimum. This final COM was then used as the starting guess for the next frame, which continued until all COMs were calculated for each particle in each frame. Then images were aligned based on the COM location.

After image alignment, the dataset was time-averaged using a sliding window calculation of 5 frames (10 seconds). In this calculation new frame 1 is the average of frames 1-5, new frame 2 is the average of frame 2-6, etc. This improved signal-to-noise ratio and segmentation reliability. Next, the intensity of each image was normalized with respect to an empty region of the cell adjacent to each particle. This was done to correct particle intensity values for the variation in thickness in different regions of the liquid cell. Before segmentation, the images were flattened to correct for the non-uniform illumination caused by the liquid cell. This was done in the local crop for each particle due to the large number of artifacts in the dataset. First, a local adaptive thresholding algorithm was used to get a rough segmentation map.[11] Then the background of the rough segmentation map was fit with a first order plane to locally approximate the liquid cell gradient. Then the image was divided by the plane to remove the background and flatten the image. A flat image is needed for accurate threshold segmentation. The flat images were used for segmentation, as well as the angular intensity map, but were not used for the contrast calculation (details on this in data analysis).

4.3.2 Vesicle segmentation-based area and contrast analysis

After processing the normalized images were converted to binary images. This was done using Otsu method thresholding,[10] which finds a statistically significant value which divides the two classes: the object and the background. Next, binary operations were performed to identify a representative binary object map (Figure 4.2). First, all binary objects except for the largest were removed. Then image closing was performed,[12] which was done to connect gaps in the perimeter of the object. Then the binary object was filled in. Finally, image opening was performed, which removed the sharp features from the edges of the image. This "minimum feature size" was applied to prevent random variations in the background to be included in the object mask. In the case where there is a sharp feature on the perimeter, smoothing the boarder will have very little impact on the area, average intensity, or angular intensity map.

Once the binary maps were calculated for each particle in each frame, the particle perimeter was determined with a custom algorithm, highlighted in Figure 4.6. First, the binary mask of particle was transformed into polar space about the center of mass.[13] The next goal was to define a continuous perimeter around the particle, which was challenging due to rupturing of the cell membranes leading to a discontinuous perimeter shown in Figure 4.6. This was corrected by a custom algorithm which moves the disconnected pixels upward one pixel at a time (iteratively from left to right, then right to left) until a continuous perimeter was defined in polar space, shown as the green line in Figure 4.6. Equivalent, this defines a maximum curvature which allows the perimeter to dynamically change as the structure evolves, but also prevents instability at gaps caused by ruptures in the membranes. This line was then transformed into cartesian space to define the perimeter of the particle. This was repeated for every particle in every frame.

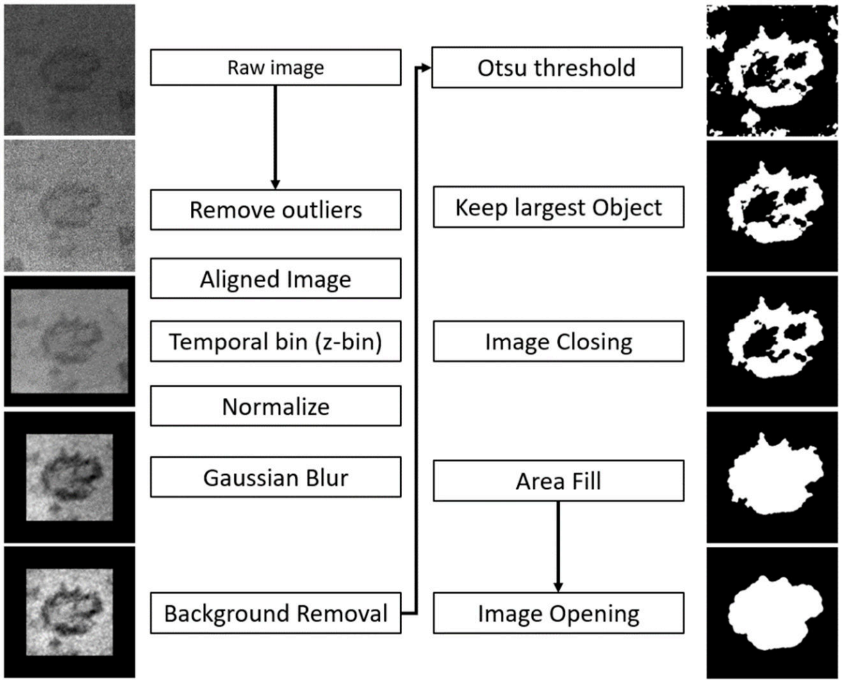

Figure 4.2 Image processing pipeline for particle segmentation. The image processing steps are outlined for a representative image, which are described in more detail in the text above. This pipeline was applied to each particle of the study individually.

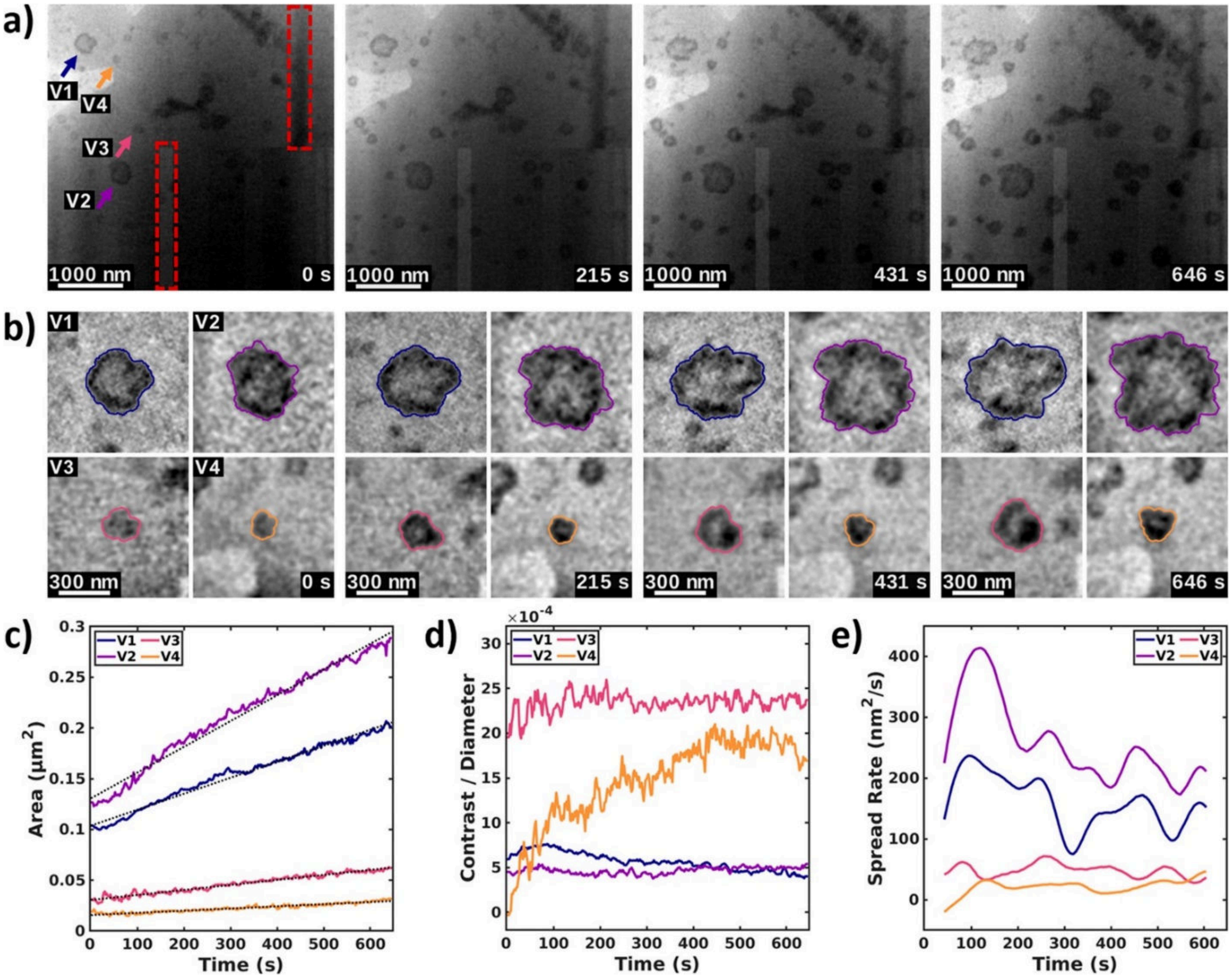

Figure 4.3 Vesicle spreading during bilayer formation. (a) Time series of Video 1: the colored arrows indicate each vesicle that was analyzed further, and the red dashed box highlights detector artifacts. (b) Time series of individual vesicles in Video 1 (15 e–/nm2·s). Colored outlines correspond to the arrows. (c) The area evolution of each vesicle shown above. The dashed line indicates a linear fit. (d) Ratio of average membrane contrast to membrane diameter. (e) The evolution of the spread rate for each vesicle shown above.

The perimeters defined above were used for quantitative analysis. The pixel area of each mask was converted to area and used to generate the area plot (Figure 4.3c). Contrast was calculated with the temporally binned frames before flattening, described in the Image Processing section. Contrast is defined as 1 – I_particle / I_background,[13] where I_particle is the average intensity in the binary mask, and I_background is the average intensity of the background adjacent to the particle. This definition of contrast is used to correct for the global fluctuations in intensity seen in Figure 4.3a and Video 1. For each frame, the contrast was divided by the equivalent diameter, calculated as 2 * sqrt(area/pi). This was repeated for each particle. The plot of Spread Rate vs Time was generated from the derivative of the Area vs Time plot, but required additional signal processing for meaningful interpretation. A 1D Gaussian-weighted sliding average was applied to the Area vs Time plot to smooth out frame-to-frame variations which would otherwise cause instability in the derivate. A normalized 1D Gaussian with a standard deviation of 21 frame (42 seconds) was convoluted with the signal before the derivative calculation. The raw vs filtered signal is shown in Figure 4.4. The data was extended at the boundary conditions for the calculation, and the first and last 21 points are removed in Figure 4.3 because of this boundary condition.

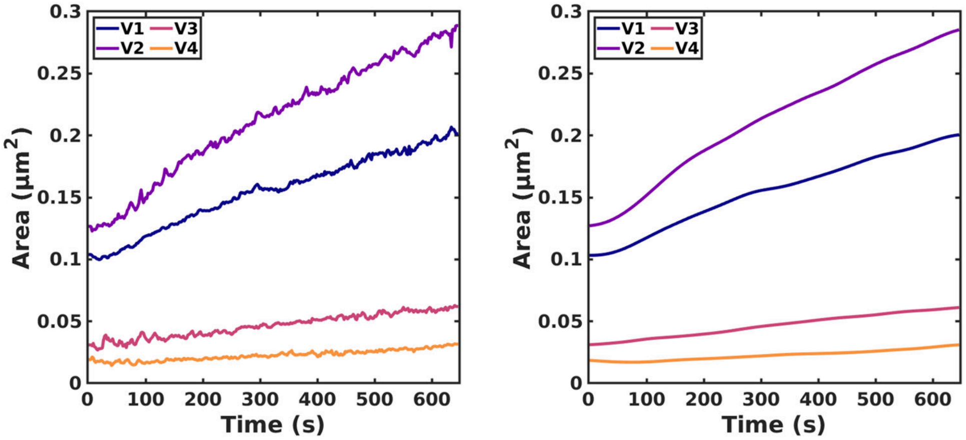

Figure 4.4 Gaussian-Weighted sliding average for signal filtering prior to derivative calculation. Left shows unfiltered area calculation, while right shows the filtered signal which was used for the derivative calculation shown in Figure 4.3.

The same segmentation and analysis methodology was applied to a particle in each of the control experiments (Figure 4.5). The only notable difference in segmentation methodology was the use of a watershed transform to disconnect touching particles. Analysis of the graphs show there is very little change in properties within the relevant experimental timeframe.

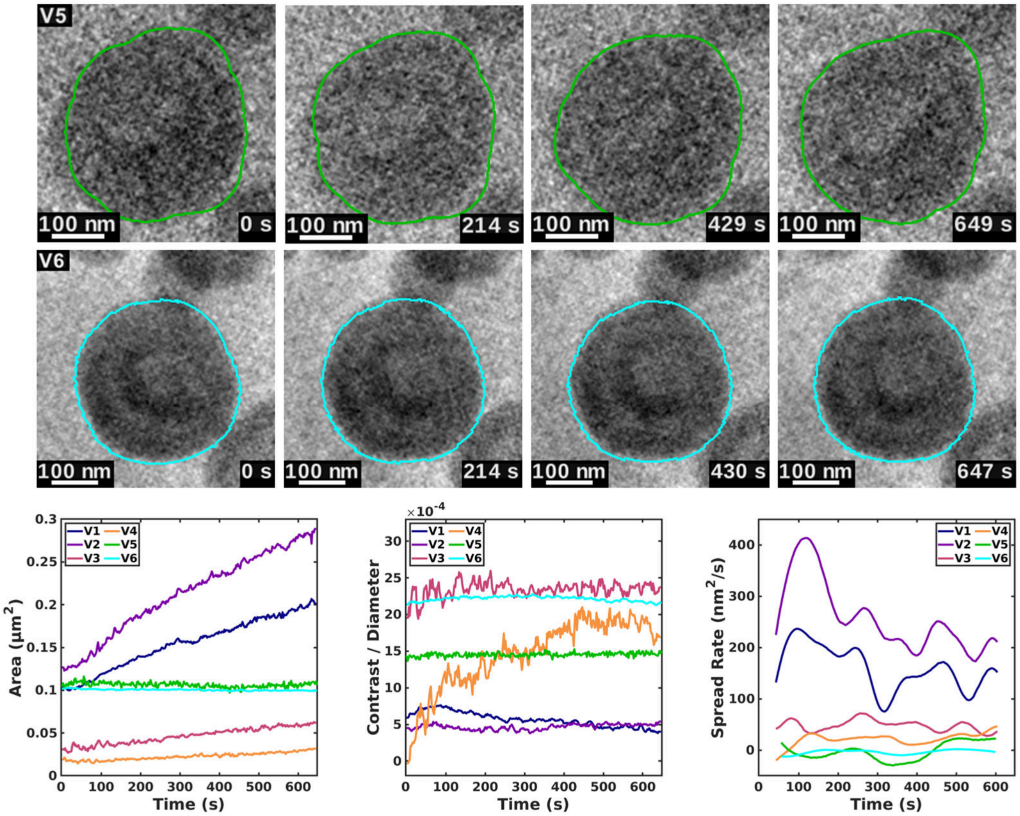

Figure 4.5 Quantitative analysis of a particle in each control experiment.

4.3.3 Vesicles membrane rupture analysis

Qualitatively, it is clear the vesicles in Figure 4.3 are changing in morphology as the solvent environment changes. The goal of this analysis was to visualize the change in structure by measuring the change in intensity at the wall of the vesicle (Figure 4.7).

Particle 1 was further analyzed after the drift stabilization and processing described above. Once the continuous perimeter of the vesicle was defined, the perimeter was lower by 11 pixels (70 nm) in the polar transform to define the inner perimeter of the membrane (green lines in Figure 4.6). Next, polar transforms of the flat, normalized images were calculated (defined in the Image Processing section). Here, the origin of the polar transform is the origin of the image, which is located at the calculated center of mass of the vesicle in each frame (See Image Processing section). For each column of the polar transform, the normalized values between the top and bottom perimeter were averaged to determine the average angular intensity of the membrane. The color of this average angular intensity was then mapped to the cartesian perimeter as a function of angle. Additionally, the average angular intensity profile from each frame was concatenated to produce an angular intensity map, which shows the change in membrane intensity as a function of time and angle for the entire dataset (Figure 4.7b). Figure 4.7c was produced by simply plotting the colored cartesian perimeters on a white background.

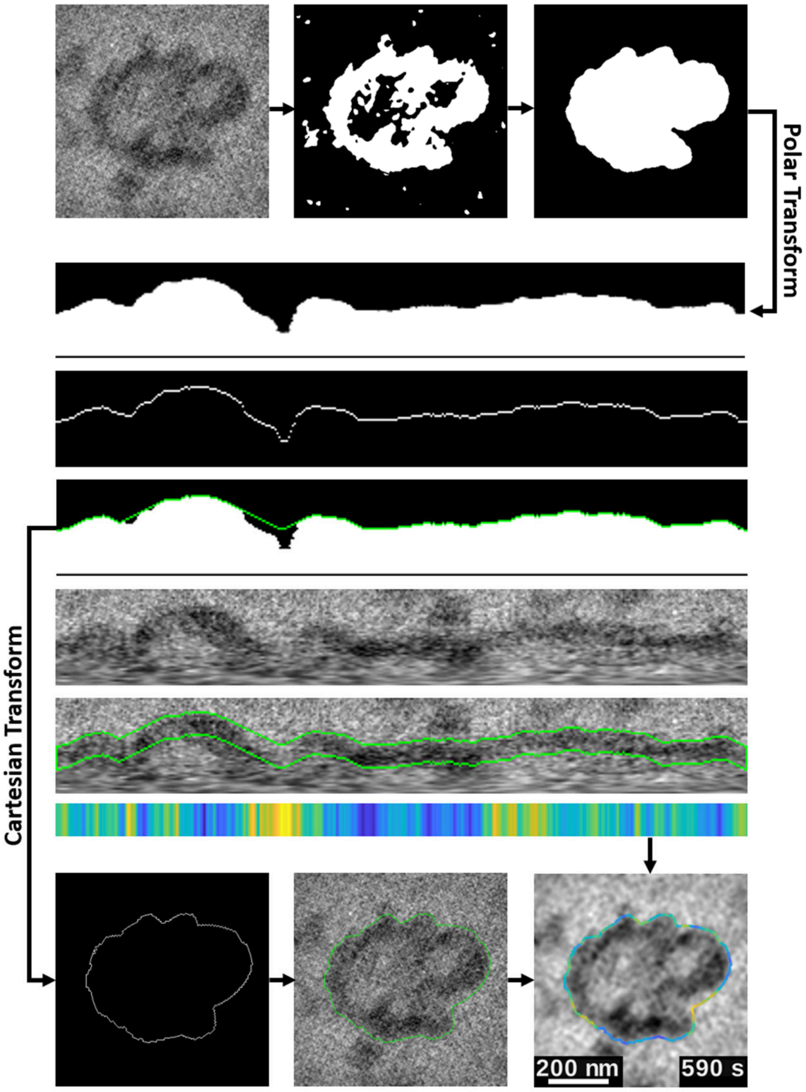

Figure 4.6 Image processing pipeline for defining particle perimeter from binary map. A combination of polar and cartesian transforms were used to define a continuous perimeter of each particle. The images above demonstrate how this works when there is a significant gap in the vesicle. The colormap produced from the column averaging in polar space was mapped to the perimeter based on angular position in cartesian space.

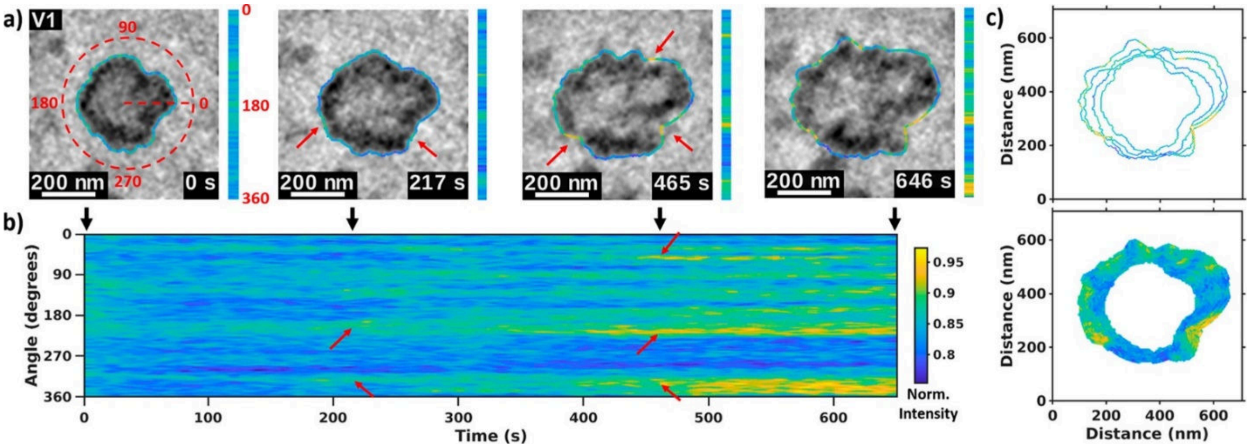

Figure 4.7 Membrane analysis of vesicle (V1). (a) Snapshots of the LCTEM Video 1 during the solvent exchange process. The outline intensity shows the integrity of the membrane; a high intensity of detected electrons means the membrane has been ruptured in that area. (b) Angular intensity map of the vesicle pictured above (more details in the SI). The red arrows correspond to the individual areas in the vesicle membrane where the rupture was observed. (c) Overlayed particle outlines for the selected frame (top) and all frames (bottom).

We recognize there is some subjectivity in defining the membrane as 11 pixels (70 nm) from the polar transform of the segmentation map outline. This was chosen empirically to maximize signal at the membrane edge where the thinning and rupture is occurring. Below, we will also provide the angular intensity map for the entire pixel range, from the outermost pixel of the perimeter to the center of mass pixel (Figure 4.8, center). Here, we see contrast between thick and thin regions is reduced due to the large number of pixels, and because most pixels in the center of the vesicle are generally bright. This leads to reduced contrast between dense and thin sections. Also, structural changes taking place inside the vesicle are now considered in the calculation. For example, there is a reduction in rupture intensity at the 500 second mark between 300 and 360 degrees, due to the vesicle wall caving inward and creating a region of high density here (See Figure 4.7a). While the signal strength changes, the same features can be seen in both angular intensity maps. This shows the features are not a result of membrane boundary selection. We also show the angular intensity map for the center of the vesicle, excluding the 11 pixels at the membrane edge (Figure 4.8, bottom). Here, the intensities are much brighter on average, and become brighter as the vesicle expands. While the intensity does change at some angles as the membrane collapses inward, there are not as many features in this angular intensity map.

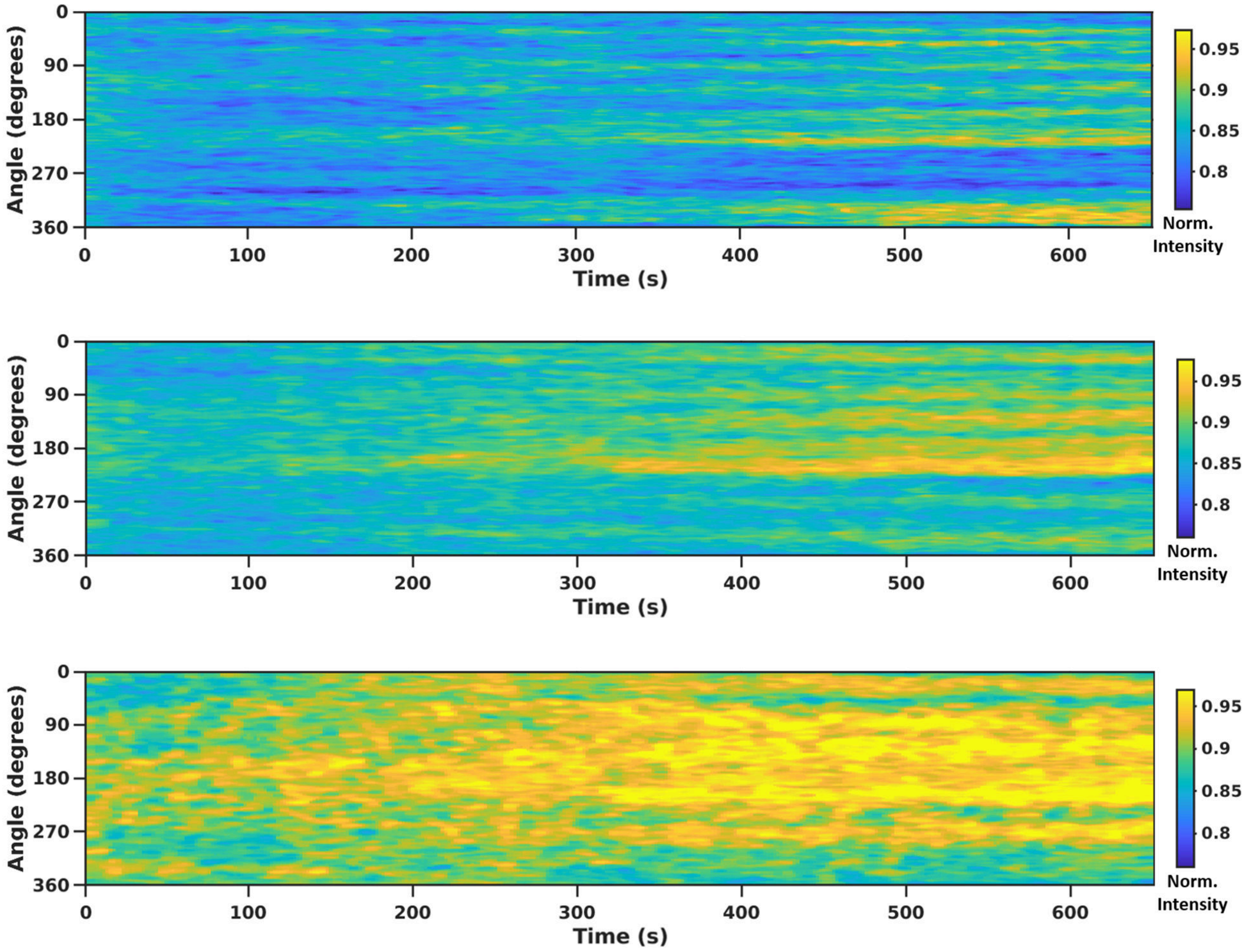

Figure 4.8 Comparison of angular intensity map for different radial distances. Top shows the angular intensity map for the mean intensity values within 11 pixels (70 nm) of the perimeter in the polar transform. Center shows the angular intensity map for the mean intensity values from the perimeter to the center of mass pixel, average of 35 pixels (222 nm). Bottom shows the angular intensity map for the mean intensity values from the center of mass pixel to 11 pixels before the perimeter (the center of the vesicle excluding the membrane). All images are displayed on the same contrast boundaries.

Although forcing the perimeter to be continuous (see Figure 4.6) will impact the resulting angular intensity map, as the intensity at each angle is calculated based on the location of the perimeter, Figure 4.9 shows the angular intensity map from the discontinuous perimeter, which was taken from the top pixels of the polar transform of each segmentation map. Note that because the perimeter may be discontinuous, the radial distances of adjacent angles are not necessarily at similar radial distances. Here, most of the features are the same since many regions did not require any correction. The largest differences are between 300 and 360 degrees, where a significant correction was needed to make the perimeter continuous. Overall, the majority of the features are not affected by the continuous perimeter algorithm and are not dependent on this processing technique.

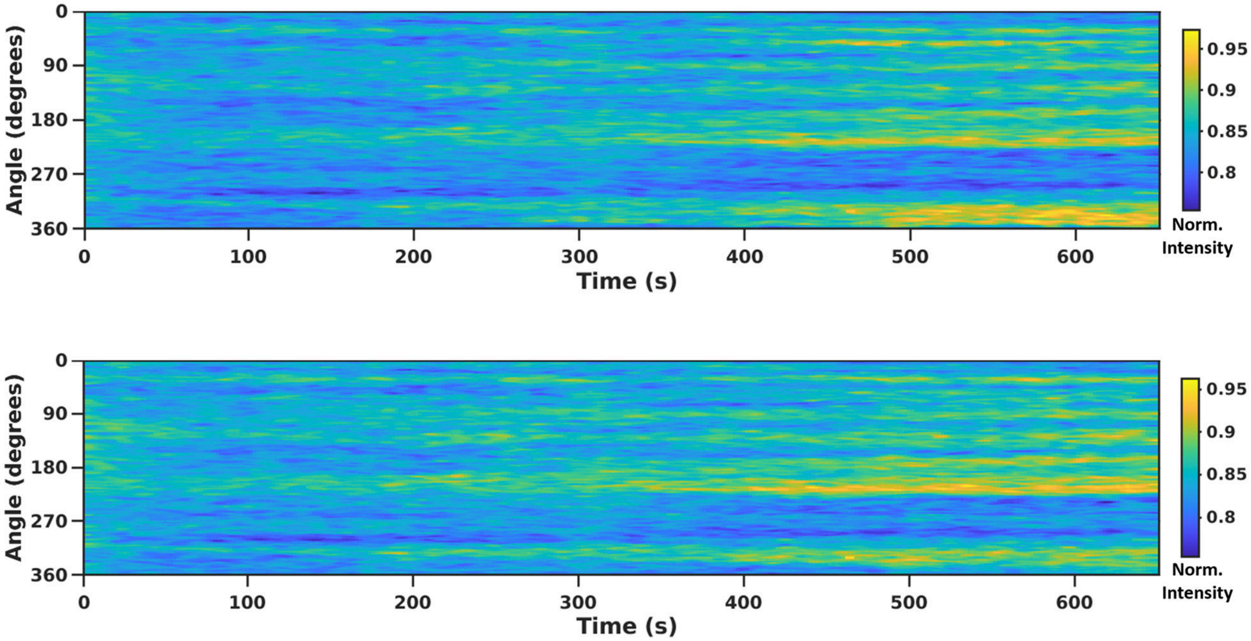

Figure 4.9 Comparison of angular intensity map for different perimeter definitions. Top shows the angular intensity map for the mean intensity values within 11 pixels (70 nm) of the continuous perimeter in the polar transform (Figure 4.7b). Bottom shows the angular intensity map for the mean intensity values within 11 pixels (70 nm) of the discontinuous perimeter (details in Vesicle Segmentation section) in the polar transform.

4.3.4 Video cross sectional time series analysis of bilayer formation

The formation of the bilayer was characterized with image analysis techniques. We were interested in studying two events in the dataset – a boundary dissipation and a boundary formation. The goal of this analysis was to visualize the structural transformation occurring in each event by studying the changes in contrast (Figure 4.10). We applied a cross-sectional time series to Video 2 to generate a single image which captured the temporal progression of both events to compare the structural rearrangement in the material.

First, the frames were temporally binned by 3 frame (15.5 s) to improve the signal-to-noise ratio. Next, a Gaussian kernel with a first standard deviation of 5 pixels (5.4 nm) was convoluted with each frame (Gaussian blur) to reduce Gaussian noise. A cross sectional time series implemented using an in-house MATLAB script to examine two key events which occur during bilayer formation.[13] In each case, the region was manually specified by 2 points forming a line, and a thickness in the region of analysis, shown by the green outline in Figure 4.10b,c. This region was converted to a vertical crop. For each frame, the vertical crop was averaged across each row, producing a 1D column of pixels. Each 1D vertical column was concatenated to produce a 2D image, where each column represents a unique frame (time point), and each row is the mean intensity of that location in the image. The intensity values in each final image were normalized between 0 and 1. This transforms the 3D video into a 2D video that can be easily interpreted.

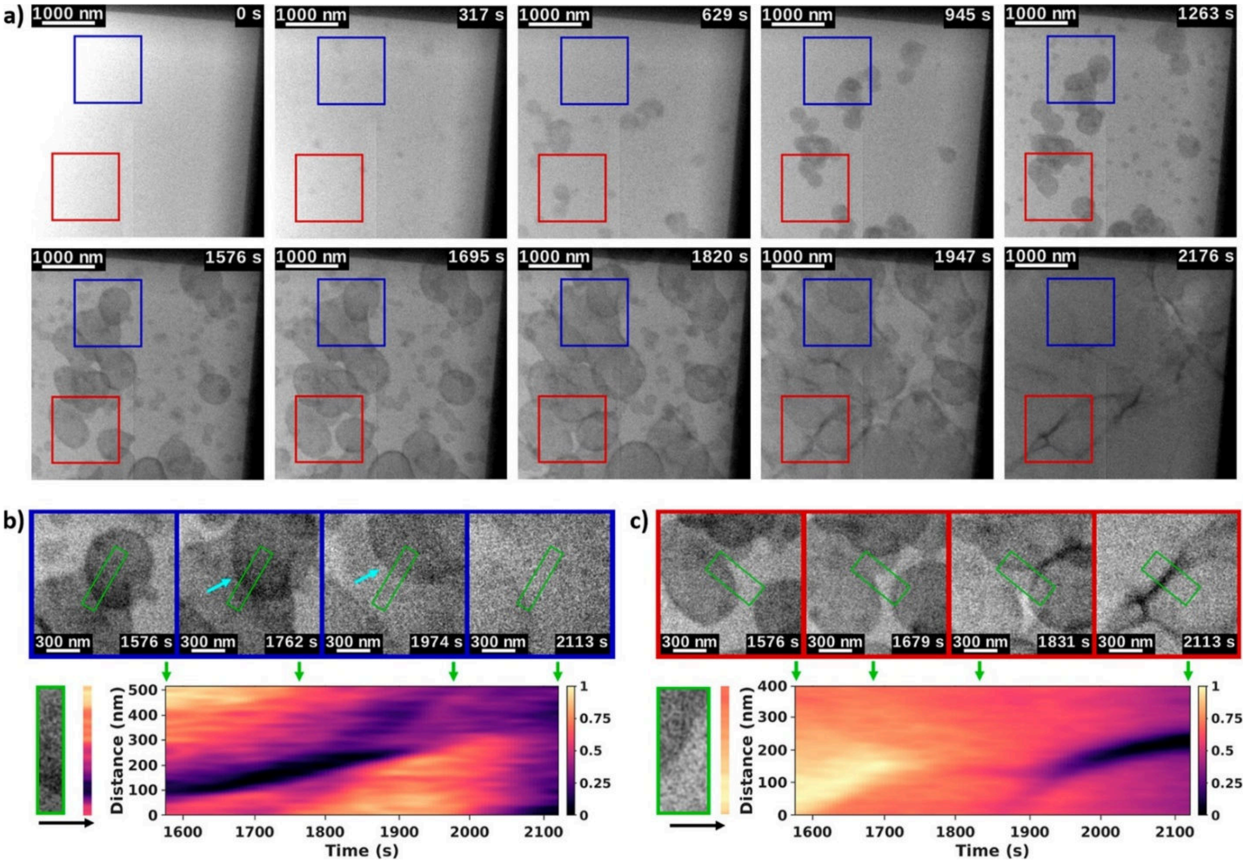

Figure 4.10 LCTEM analysis of droplet spreading during bilayer formation. (a) Snapshots of the LCTEM Video 2 (11 e–/nm2·s) during the solvent exchange process. The blue and red boxes highlight examples of pristine bilayer formation and defect formation, respectively. (b) Close view of two droplets completely fusing together to form a homogeneous bilayer along with the cross-sectional time series of the highlighted green box to show a homogeneous bilayer area. (c) Close view of two droplets merging to form a bilayer boundary along with the cross-sectional time series of the highlighted green box to visualize boundary formation.

4.3.5 Bilayer coverage calculation

The percent coverage of the bilayer in the liquid cell viewing area was calculated based on the last frame of Video 2 (Figure 4.10). The dark edges of the cell were omitted from the percent coverage calculation. The number of pixels representing the covered area (green tint) was divided by the number of pixels in the viewing area (the rest of the image, not including the edge of the cell). The result was 99.8% coverage of the bilayer (Figure 4.11).

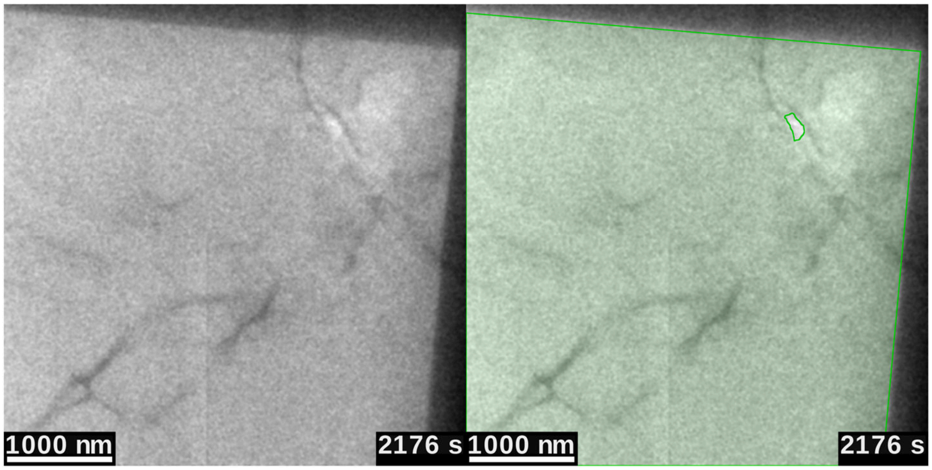

Figure 4.11 Percent coverage of the bilayer in the viewing area for the last frame of Video 2. The covered area was segmented manually and given a green tint in the right image.

4.4 Discussion

Vesicle rupture is the most accepted mechanism for SB formation.[14] The driving force for vesicle rupture is proposed to be the high curvature of the vesicles at the substrate-vesicle interface.[15] Additionally, it has been reported that rupture and spreading occurs through the widening of a pore and attachment of the outer membrane surface to the substrate.[15] The exposed edge is known to catalyze other vesicles to rupture due to the high energy conformation of lipids at the edge of a bilayer. This thermodynamically favors larger supported bilayers and makes smaller bilayers (diameter ≈ 300 nm) unstable.[15] Our LCTEM data (Figure 4.3a), shows individual vesicles undergoing spreading and rupture. In this experiment we obtained a partially dry cell, which can be seen from the contrast gradient in the top left of the image series (Figure 4.3a).[16,17] The area and membrane contrast of 4 individual vesicles within the wet areas of the cell were quantified using image analysis (Figure 4.3b-d). An in-house MATLAB script was developed to segment the vesicles across each frame in the dataset for quantitative analysis as described above. The data shows that the larger vesicles (V1 and V2) grow much faster than the smaller vesicles (V3 and V4) (Figure 4.3c). We have previously shown that for a vesicle growth mechanism, the ratio between the membrane contrast and the equivalent membrane diameter (C/D) in the TEM images should increase as the membrane diameter increases.[13] This is mainly due to the increase in polymer volume fraction within the membrane as the solvent exchange proceeds. However, despite the large area increase for V1 and V2, V1 shows a decrease in C/D, and V2 shows virtually no change in C/D. This indicates that the vesicles are undergoing spreading rather than growth. Consequently, we can quantify the vesicle spread rate as the change in area vs. time (Figure 4.3e). The data shows there is a decrease in the spread rate of V1 and V2 over the course of the experiment indicating the polymers are becoming kinetically trapped. V3 and V4 are much smaller and show an increase in C/D with increasing diameters indicating they are likely undergoing growth and spreading during data collection. All block copolymer bilayers (Figure 4.3a) were < 500 nm in equivalent diameter which is interesting because it has previously been shown that lipid bilayers and not stable in this size range.[18]

To interpret the membrane dynamics during rupture and spreading, a MATLAB script was developed to produce a time-resolved angular intensity map of the segmented membrane for V1 (Figure 4.6, Figure 4.7). The data shows the vesicle spreading anisotropically, and that multiple localized regions in the membrane begin to thin before eventually rupturing between 400 and 500 seconds (Figure 4.7b, c). Other regions appear to be more fixed to the substrate, and do not significantly change over time (Figure 4.7c). It has previously been shown that the surface chemistry and binding affinity dictates whether vesicles undergo intact adsorption or SB formation.[19,20] We believe our LCTEM data is a direct visualization of why substrate attachment is required for vesicle spreading. When the solvent exchange process is performed in a vial (i.e. when the vesicles are not adhered to a surface), the size of the vesicles increases with increasing amount of water addition, as determined by dynamic light scattering (Figure 4.8).[21] However when the solvent exchange is performed and a vesicle is adhered to a surface at multiple locations, the size increase in these regions is hindered. This results in the formation of a supported bilayer through anisotropic swelling, rupture, and spreading. This mechanism has been previously discussed but not directly obsvered.[22,23]

In pathway 2 (Figure 4.10a) we observe the liquid-liquid phase separation (also known as coacervation) and the formation of droplets that diffuse across the surface, coalesce, and then spread to cover the surface. The resulting SB shows 99.8% surface coverage (Figure 4.11) and minimal nanoscale defects. We interpret the early-stage structures as liquid droplets based upon their dynamic motion during fusion. Coacervate droplets are typically thought to be membraneless and their spreading and fusion dynamics have been less studied compared to vesicles.[24] In this dataset, droplets fuse together within a few seconds, which is much quicker than what is expected for block copolymer nanoparticles.[25,26] Based on control experiments we believe that liquid-liquid phase separation occurs at ~10% water content (Figure 4.9). We have shown previously that nonionic BCP can form coacervates (stable droplets) in organic water mixtures where slight variations in the water composition may shift the favored phase into the self-assembled phase.[27] The droplet formation in the LCTEM experiment suggests that the solvent exchange rate was slow enough that the polymers are not kinetically arrested in the early stages of SB formation. Due to the fact that the liquid-liquid phase separation does not favor stable nanodroplets we were unable to perform the same electron dose control experiment. However, as the organic solvent content is higher for droplets than for vesicles, we believe that the vesicle control is valid as a guide for the droplet experiments (Figure 4.5).

These data show that droplet fusion and spreading can either lead to homogenous bilayers (Figure 4.10a,b, blue region) or regions with defects (Figure 4.10a,c, red region). To better visualize the droplet fusion dynamics and defect formation, cross-sectional time series plots were created for both the red and blue regions (Figure 4.10b,c). The analysis of the blue region shows that fusion between the two droplets had already started before the droplets appeared in the viewing area of the cell (t < 1576 seconds). The higher contrast at the droplet interface indicates a higher polymer concentration and different polymer organization at the interface. In our previous studies we have performed self-consistent mean field calculations on similar di-block copolymer systems which show a direct relationship between polymer concentration and contrast.[13] Over time, the polymer density at the interface decreases, and the resulting supported bilayer region becomes homogeneous (t > 2000 seconds). The analysis of the red region shows droplet fusion occurs later in the dataset (t > 1800 seconds) and produces a dense region at the interface, which we interpret as a defect in the bilayer. This is likely due to the kinetically limited reorganization of polymers at droplet interface, which we have previously observed during the formation of block copolymer vesicles.[13] However, the observations here indicate that premature organization at the droplet interface leads to defect formation in the final SB structure (Figure 4.10c).

4.5 Conclusions

We have demonstrated that LCTEM can be used to observe and quantify the formation of supported polymer bilayers with nanoscale resolution in real time. We observed two pathways of bilayer formation derived from vesicle spreading and droplet spreading. Image segmentation and contrast analysis was used to quantify individual vesicle spread rates and track the formation of membrane rupture points. This method could be extended to image lipid bilayer spreading, although lipids can be much more difficult to image.[28,29] In addition, image analysis was used to visualize the formation of bilayers via the droplet spreading mechanism. The data and accompanying analysis suggest that defects form due to kinetically limited reorganization of polymers at droplet interfaces. Our observations make it clear that liquid-precursors are important to form defect free supported bilayers when using the solvent assisted method. The examples presented here demonstrate how image processing algorithms can be used to quantify processes captured in LCTEM datasets and directly address materials science questions.

4.6 References

(1) Fielding, L. A.; Lane, J. A.; Derry, M. J.; Mykhaylyk, O. O.; Armes, S. P. Thermo-Responsive Diblock Copolymer Worm Gels in Non-Polar Solvents. *J. Am. Chem. Soc.* **2014**, *136* (15), 5790–5798. https://doi.org/10.1021/ja501756h.

(2) Nicolai, T.; Colombani, O.; Chassenieux, C. Dynamic Polymeric Micelles versus Frozen Nanoparticles Formed by Block Copolymers. *Soft Matter* **2010**, *6* (14), 3111. https://doi.org/10.1039/b925666k.

(3) Andrews, D.; Nann, T.; Lipson, R. H. *Comprehensive Nanoscience and Nanotechnology*; Elsevier Science, 2019.

(4) Lind, T. K.; Cárdenas, M. Understanding the Formation of Supported Lipid Bilayers via Vesicle Fusion—A Case That Exemplifies the Need for the Complementary Method Approach (Review). *Biointerphases* **2016**, *11* (2), 020801. https://doi.org/10.1116/1.4944830.

(5) Reimhult, E.; Kasemo, B.; Höök, F. Rupture Pathway of Phosphatidylcholine Liposomes on Silicon Dioxide. *IJMS* **2009**, *10* (4), 1683–1696. https://doi.org/10.3390/ijms10041683.

(6) Andrecka, J.; Spillane, K. M.; Ortega-Arroyo, J.; Kukura, P. Direct Observation and Control of Supported Lipid Bilayer Formation with Interferometric Scattering Microscopy. *ACS Nano* **2013**, *7* (12), 10662–10670. https://doi.org/10.1021/nn403367c.

(7) Wu, H.-L.; Chen, P.-Y.; Chi, C.-L.; Tsao, H.-K.; Sheng, Y.-J. Vesicle Deposition on Hydrophilic Solid Surfaces. *Soft Matter* **2013**, *9* (6), 1908–1919. https://doi.org/10.1039/c2sm27450g.

(8) Rizvi, A.; Mulvey, J. T.; Patterson, J. P. Observation of Liquid–Liquid-Phase Separation and Vesicle Spreading during Supported Bilayer Formation via Liquid-Phase Transmission Electron Microscopy. *Nano Lett.* **2021**, *21* (24), 10325–10332. https://doi.org/10.1021/acs.nanolett.1c03556.

(9) Yao, L.; Ou, Z.; Luo, B.; Xu, C.; Chen, Q. Machine Learning to Reveal Nanoparticle Dynamics from Liquid-Phase TEM Videos. *ACS Cent. Sci.* **2020**, *6* (8), 1421–1430. https://doi.org/10.1021/acscentsci.0c00430.

(10) Otsu, N. A Threshold Selection Method from Gray-Level Histograms. *IEEE Transactions on Systems, Man, and Cybernetics* **1979**, *9* (1), 62–66. https://doi.org/10.1109/TSMC.1979.4310076.

(11) Xiong, G. *Local Adaptive Thresholding - File Exchange - MATLAB Central*. https://www.mathworks.com/matlabcentral/fileexchange/8647-local-adaptive-thresholding (accessed 2021-08-31).

(12) Mat Said, K. A.; Jambek, A.; Sulaiman, N. A Study of Image Processing Using Morphological Opening and Closing Processes. *International Journal of Control Theory and Applications* **2016**, *9*, 15–21.

(13) Ianiro, A.; Wu, H.; Rijt, M. M. J. van; Vena, M. P.; Keizer, A. D. A.; Esteves, A. C. C.; Tuinier, R.; Friedrich, H.; Sommerdijk, N. A. J. M.; Patterson, J. P. Liquid–Liquid Phase Separation during Amphiphilic Self-Assembly. *Nat. Chem.* **2019**, *11* (4), 320–328. https://doi.org/10.1038/s41557-019-0210-4.

(14) Keller, C. A.; Glasmästar, K.; Zhdanov, V. P.; Kasemo, B. Formation of Supported Membranes from Vesicles. *Phys. Rev. Lett.* **2000**, *84* (23), 5443–5446. https://doi.org/10.1103/PhysRevLett.84.5443.

(15) Hamai, C.; Cremer, P. S.; Musser, S. M. Single Giant Vesicle Rupture Events Reveal Multiple Mechanisms of Glass-Supported Bilayer Formation. *Biophysical Journal* **2007**, *92* (6), 1988–1999. https://doi.org/10.1529/biophysj.106.093831.

(16) Zheng, H.; Claridge, S. A.; Minor, A. M.; Alivisatos, A. P.; Dahmen, U. Nanocrystal Diffusion in a Liquid Thin Film Observed by in Situ Transmission Electron Microscopy. *Nano Lett.* **2009**, *9* (6), 2460–2465. https://doi.org/10.1021/nl9012369.

(17) Patterson, J. P.; Abellan, P.; Denny, M. S.; Park, C.; Browning, N. D.; Cohen, S. M.; Evans, J. E.; Gianneschi, N. C. Observing the Growth of Metal–Organic Frameworks by in Situ Liquid Cell Transmission Electron Microscopy. *J. Am. Chem. Soc.* **2015**, *137* (23), 7322–7328. https://doi.org/10.1021/jacs.5b00817.

(18) Banerjee, S.; Lyubchenko, Y. L. Topographically Smooth and Stable Supported Lipid Bilayer for High-Resolution AFM Studies. *Methods* **2021**. https://doi.org/10.1016/j.ymeth.2021.02.010.

(19) Reimhult, E.; Höök, F.; Kasemo, B. Intact Vesicle Adsorption and Supported Biomembrane Formation from Vesicles in Solution: Influence of Surface Chemistry, Vesicle Size, Temperature, and Osmotic Pressure. *Langmuir* **2003**, *19* (5), 1681–1691. https://doi.org/10.1021/la0263920.

(20) Keller, C. A.; Kasemo, B. Surface Specific Kinetics of Lipid Vesicle Adsorption Measured with a Quartz Crystal Microbalance. *Biophys J* **1998**, *75* (3), 1397–1402.

(21) Luo, L.; Eisenberg, A. Thermodynamic Size Control of Block Copolymer Vesicles in Solution. *Langmuir* **2001**, *17* (22), 6804–6811. https://doi.org/10.1021/la0104370.

(22) Andrecka, J.; Spillane, K. M.; Ortega-Arroyo, J.; Kukura, P. Direct Observation and Control of Supported Lipid Bilayer Formation with Interferometric Scattering Microscopy. *ACS Nano* **2013**, *7* (12), 10662–10670. https://doi.org/10.1021/nn403367c.

(23) Dorn, J.; Belegrinou, S.; Kreiter, M.; Sinner, E.-K.; Meier, W. Planar Block Copolymer Membranes by Vesicle Spreading. *Macromolecular Bioscience* **2011**, *11* (4), 514–525. https://doi.org/10.1002/mabi.201000396.

(24) Yewdall, N. A.; André, A. A. M.; Lu, T.; Spruijt, E. Coacervates as Models of Membraneless Organelles. *Current Opinion in Colloid & Interface Science* **2021**, *52*, 101416. https://doi.org/10.1016/j.cocis.2020.101416.

(25) Parent, L. R.; Bakalis, E.; Ramírez-Hernández, A.; Kammeyer, J. K.; Park, C.; de Pablo, J.; Zerbetto, F.; Patterson, J. P.; Gianneschi, N. C. Directly Observing Micelle Fusion and Growth in Solution by Liquid-Cell Transmission Electron Microscopy. *J. Am. Chem. Soc.* **2017**, *139* (47), 17140–17151. https://doi.org/10.1021/jacs.7b09060.

(26) Li, C.; Chen Tho, C.; Galaktionova, D.; Chen, X.; Král, P.; Mirsaidov, U. Dynamics of Amphiphilic Block Copolymers in an Aqueous Solution: Direct Imaging of Micelle Formation and Nanoparticle Encapsulation. *Nanoscale* **2019**, *11* (5), 2299–2305. https://doi.org/10.1039/C8NR08922A.

(27) Rizvi, A.; Patel, U.; Ianiro, A.; Hurst, P. J.; Merham, J. G.; Patterson, J. P. Nonionic Block Copolymer Coacervates. *Macromolecules* **2020**, *53* (14), 6078–6086. https://doi.org/10.1021/acs.macromol.0c00979.

(28) Gnanasekaran, K.; Chang, H.; Smeets, P. J. M.; Korpanty, J.; Geiger, F. M.; Gianneschi, N. C. In Situ Ni2+ Stain for Liposome Imaging by Liquid-Cell Transmission Electron Microscopy. *Nano Lett.* **2020**, *20* (6), 4292–4297. https://doi.org/10.1021/acs.nanolett.0c00898.

(29) Piffoux, M.; Ahmad, N.; Nelayah, J.; Wilhelm, C.; Silva, A.; Gazeau, F.; Alloyeau, D. Monitoring the Dynamics of Cell-Derived Extracellular Vesicles at the Nanoscale by Liquid-Cell Transmission Electron Microscopy. *Nanoscale* **2018**, *10* (3), 1234–1244. https://doi.org/10.1039/C7NR07576F.

CHAPTER 5: Liquid electron microscopy with non-aqueous solvents: evaluating the beam-sample interactions of complex liquid structures

This Chapter was adapted from a published article (Justin T Mulvey, Aoon Rizvi, Joseph P Patterson. "Liquid Electron Microscopy with Non-Aqueous Solvents: Evaluating the Beam-Sample Interactions of Complex Liquid Structures." Microscopy and Microanalysis. 2023, 29 (Supplement_1), 1758–1760).

5.1 Introduction

Advances in liquid cell transmission electron microscopy (LCTEM) have made it possible to study solution-state processes in real-time with nanometer scale resolution.[1] Recent LCTEM studies have shown that dissolved polymers can form liquid structures during self-assembly,[2] which can be controlled to engineer the structure and properties of solid-state self-assembled structures.[3] However, liquid structures can be difficult to study with LCTEM because solvent-electron interactions can introduce undesired beam effects such as local radiolysis, pH changes, and heating.[4] A recent simulation study of aqueous and non-aqueous solvent radiolysis showed that during continuous irradiation, equilibrium radical concentration could vary by orders of magnitude between solvents, causing different degrees of damage to materials in solution.[5] Here, we experimentally evaluate beam interactions with liquid structures in non-aqueous media. We use LCTEM and quantitative image analysis to show the beam can control the nucleation of polymer-rich liquid-liquid phase-separated droplets, which is the first observation in non-aqueous LCTEM. Furthermore, we show the beam can be used to stimulate and study internal and external structural dynamics in complex phase-separated nanoscale droplets, which have been predicted in literature but never observed.[6]

5.2 Methods and Results

A DENSsolutions Ocean Holder with solvent flow capabilities was used to perform solvent exchange LCTEM experiments. First, 10 mg/ml of poly(lauryl methacrylate)-block-poly(benzyl methacrylate) (PLMA-b-PBzMA) dissolved in dioxane was sealed between two SiN chips. The sample was inserted into the TEM and pure dodecane was flown into the tip of the holder to initiate solvent exchange with dioxane. After 8 minutes of imaging at 13 e-/(nm^2 s), a polymer-rich droplet spread across the viewing area. Moving to an unimaged area of the cell resulted in the nucleation of more polymer-rich droplets, which then coalesced and spread (Figure 5.1a). Polymer-rich liquid structures with similar characteristics have been reported in aqueous systems,[7] but this is the first observation in non-aqueous media.

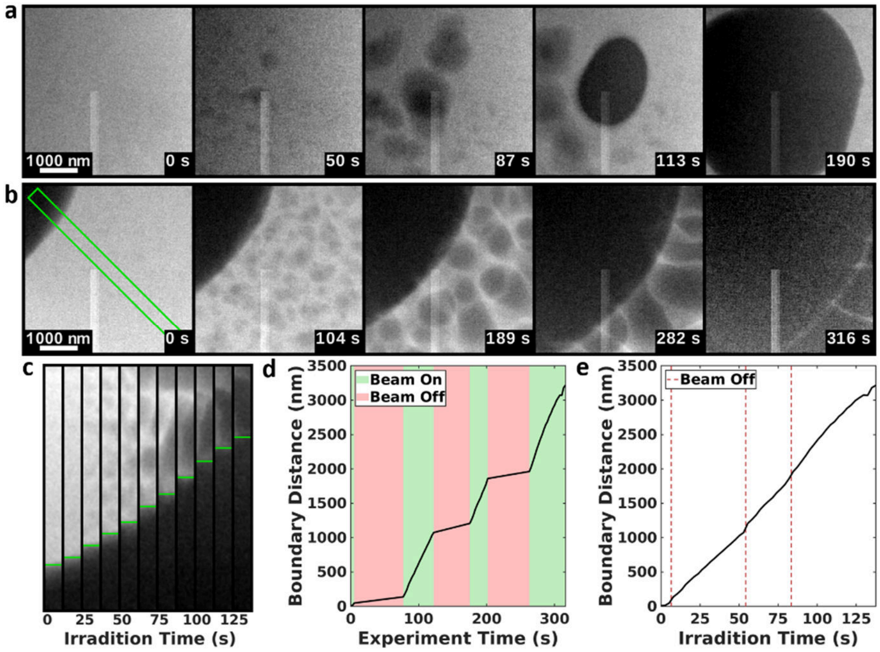

Figure 5.1 A) LCTEM frame-series of dark polymer-rich liquid droplets nucleating, coalescing, and spreading under continuous irradiation from the beam. B) Polymer-rich droplet spreading while the beam is periodically blanked and unblanked. Time labels are experiment time. C) Frame-series of cropped images from droplet spreading shown in B). The green line labels the interface between the polymer-rich droplets and polymer-poor continuous phase. D,E) Boundary distance relative to the location in the first frame plotted as a function of experiment time (D) and beam irradiation time (E).

Next, a dose study was performed to determine if the observed formation was a result of beam irradiation. The beam was moved to the edge of an already-formed polymer-rich droplet, then blanked and unblanked several times to evaluate if the droplet would continue to spread while the beam was blanked (Figure 5.1b). Quantitative image analysis was used to track the position of the droplet edge during spreading (Figure 1c). Figure 5.1d shows there is only significant droplet growth when the beam is turned on. It also shows the growth is linear and the polymer-rich droplet is spreading at an average of 24.7 nm/s along the image diagonal (Figure 5.1e). The study demonstrates that growth is promoted while the beam is on, and continuous perturbation is required to study the growth of these structures. This indicates the beam is instantaneously shifting the local equilibrium to favor polymer-rich droplet formation. Note that formation did not occur until 8 minutes into solvent exchange, suggesting both beam irradiation and a binary solvent system are necessary for polymer-rich droplet formation.

The solvent system was changed to determine if different solvent-electron interactions would alter the beam effects. The same solvent exchange experiment was performed, but dodecane was replaced with hexane. In this system, the viewing area was covered by a polymer-rich continuous phase which contained light, phase-separated, polymer-poor droplet structures (Figure 5.2a,b). Upon irradiation, these structures dissolved back into a homogeneous, polymer-rich phase which is consistent with the previously observed behavior. Unlike the previous study, the polymer-poor liquid droplets were complex and contained internally phase-separated polymer-rich nanocompartments which are clearly seen in the first frame of each series. To our knowledge, this is the first observation of spontaneous phase-separated droplets forming with internal nanocompartments in block copolymer systems.

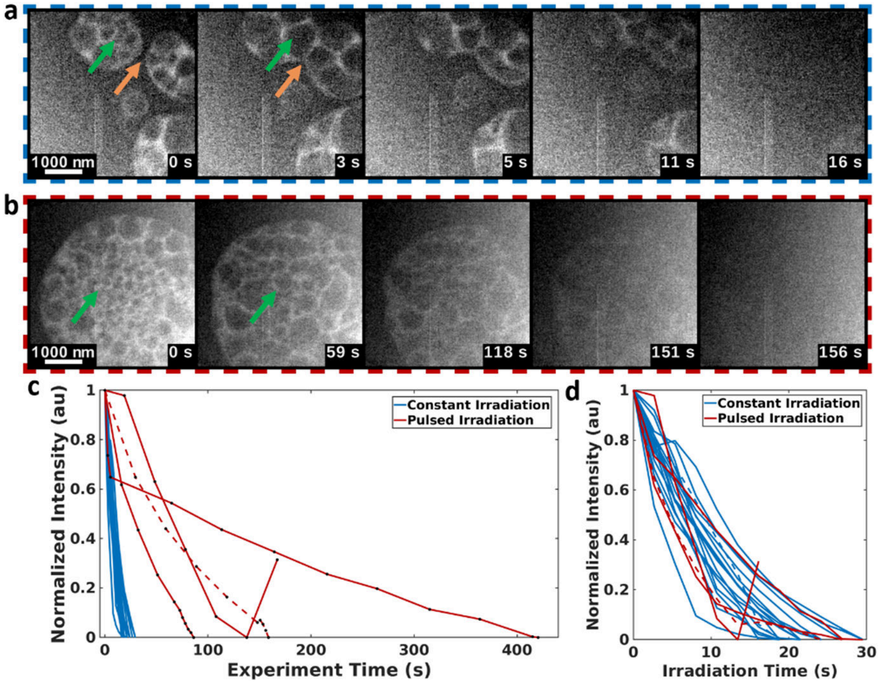

Figure 5.2 A,B) Selected images from dose study of complex liquid structures with continuous irradiation (A) and pulsed irradiation (B). Green arrows indicate internal droplet coalescence and orange arrows indicate external droplet coalescence. Time labels are experiment time. C,D) Normalized image intensity

of frame-series for each dose study plotted against experiment time (C) and exposure time (D). Frame-series shown in A,B) are distinguished with dashed lines.

Several beam dose studies were conducted on the polymer-poor droplets as they dissolved back into the polymer-rich continuous phase (Figure 5.2a,b). In 17 dose studies the droplets were irradiated continuously, and in 4 dose studies the droplets were irradiated in intervals of 2.2 seconds followed by periodic lengths of no irradiation. Quantitative image analysis was used to compare the structural dissolution rate between different frame-series and evaluate if dissolution was taking place in the absence of the beam (Figure 5.2c,d). For each frame-series, the sum of intensities in each frame was divided by the sum of the initial frame, and the output was normalized between 0 and 1. The graphs show the structures dissolve at the same rate with respect to dose whether constant irradiation (Figure 5.2c) or pulsed irradiation (Figure 5.2d) was applied, confirming the dissolutions were a result of irradiation.

5.3 Discussion

Similar to the dioxane/dodecane experiment, we see local beam interactions shifting the thermodynamic state of the system to favor a homogenous polymer-rich phase. A closer examination of the frames-series reveals unique structural dynamics occurred during the beam-induced droplet dissolution, such as internal droplet coalescence and external droplet coalescence (Figure 5.2a,b). This is the first experimental observation of dynamics in multicompartment nanodroplets. From this study, the unperturbed stability of these complex nanostructures is unknown; it is unclear if the observed dynamics and dissolution would occur without irradiation or if the structures are stable indefinitely. In either case, it is clear the beam can shift the local equilibrium to stimulate and control structural dynamics. In future studies, controlled irradiation may be useful for analyzing and controlling solution-state dynamics to engineer complex liquid nanostructures.

5.4 References

(1) Wu, H.; Friedrich, H.; Patterson, J. P.; Sommerdijk, N. A. J. M.; Jonge, N. de. Liquid-Phase Electron Microscopy for Soft Matter Science and Biology. *Advanced Materials* **2020**, *32* (25), 2001582. https://doi.org/10.1002/adma.202001582.

(2) Ianiro, A.; Wu, H.; van Rijt, M. M. J.; Vena, M. P.; Keizer, A. D. A.; Esteves, A. C. C.; Tuinier, R.; Friedrich, H.; Sommerdijk, N. A. J. M.; Patterson, J. P. Liquid–Liquid Phase Separation during Amphiphilic Self-Assembly. *Nat. Chem.* **2019**, *11* (4), 320–328. https://doi.org/10.1038/s41557-019-0210-4.

(3) Rizvi, A.; Patel, U.; Ianiro, A.; Hurst, P. J.; Merham, J. G.; Patterson, J. P. Nonionic Block Copolymer Coacervates. *Macromolecules* **2020**. https://doi.org/10.1021/acs.macromol.0c00979.

(4) Schneider, N. M.; Norton, M. M.; Mendel, B. J.; Grogan, J. M.; Ross, F. M.; Bau, H. H. Electron–Water Interactions and Implications for Liquid Cell Electron Microscopy. *J. Phys. Chem. C* **2014**, *118* (38), 22373–22382. https://doi.org/10.1021/jp507400n.

(5) Korpanty, J.; Gnanasekaran, K.; Venkatramani, C.; Zang, N.; Gianneschi, N. C. Organic Solution-Phase Transmission Electron Microscopy of Copolymer Nanoassembly Morphology and Dynamics. *Cell Reports Physical Science* **2022**, *3* (3), 100772. https://doi.org/10.1016/j.xcrp.2022.100772.

(6) Sheth, T.; Seshadri, S.; Prileszky, T.; Helgeson, M. E. Multiple Nanoemulsions. *Nat Rev Mater* **2020**, *5* (3), 214–228. https://doi.org/10.1038/s41578-019-0161-9.

(7) Rizvi, A.; Mulvey, J. T.; Patterson, J. P. Observation of Liquid–Liquid-Phase Separation and Vesicle Spreading during Supported Bilayer Formation via Liquid-Phase Transmission Electron Microscopy. *Nano Lett.* **2021**, *21* (24), 10325–10332. https://doi.org/10.1021/acs.nanolett.1c03556.